ABSTRACT

Title of Dissertation: NEW METROLOGICAL TECHNIQUES FOR MECHANICAL CHARACTERIZATION AT THE MICROSCALE AND NANOSCALE

Huiqing Jin, Doctor of Philosophy, 2004

Dissertation Directed By: Associate Professor Hugh Alan Bruck
Mechanical Engineering Department

New metrological techniques have been developed for mechanical characterization at the microscale and nanoscale as follows: (1) Development of a control system and integrated imaging capability at the microscale and nanoscale for a new biaxial microtensile tester, (2) a new method for characterizing nonlinearity in AFM imaging using Digital Image Correlation (DIC), and (3) development of pointwise DIC technique. In the biaxial microtensile tester, loading of specimen is induced through the opposing motion of dual picomotor linear actuators in orthogonal directions with a displacement resolution of less than 30 nm. Using an optical microscope, *in situ* digital images are obtained and analyzed with DIC to determine the full field displacements at the microscale over an Area of Interest (AOI) in order to characterize the biaxial performance of the microtensile tester. An objective AFM has been integrated into the biaxial microtensile tester to obtain *in situ* digital images

of topographic microstructural features at the nanoscale. These topographic images can then be converted to gray scale images with textures that are suitable for DIC to calculate full field displacements at the nanoscale. This measurement capability is demonstrated on a sputtered nanocrystalline copper film subjected to uniaxial loading in the microtensile tester. Since image quality is critical to the accuracy of the nanoscale DIC measurements, a new method was developed to calibrate the errors induced by the nonlinearity of AFM scanning. In this new method, the DIC technique was applied to AFM images of sputtered nanocrystalline NiTi films to calculate the displacement errors caused by the probe offset that must be eliminated from the apparent displacement field. The conventional DIC technique assumes a zero-order or first order approximation of the variation in displacement fields (i.e., displacement gradients) relative to the center of a subset of the image. In the case of displacement fields associated with the microstructure of a material, the displacement gradients can vary discontinuously, which violates the assumed nature of the displacement gradients in the conventional DIC. Therefore, a pointwise DIC technique has been developed to calculate displacements independently at each pixel location, eliminating the constraints imposed by the subset on the calculated displacements. Because of the potentially large number of unknown displacement variables that need to be determined using this approach, an efficient Genetic Algorithm (GA) optimization algorithm with a Differential Evolution (DE) method was investigated for optimizing the correlation function. To guarantee uniqueness of the optimized displacement field, the correlation function was modified using intensity gradients that had to be transformed from an Eulerian to Lagrangian reference frame using

displacement gradients. The theoretical development of pointwise DIC is discussed in detail using ideal sinusoidal images, and its validation using real images is also presented.

NEW METROLOGICAL TECHNIQUES FOR MECHANICAL CHARACTERIZATION AT THE MICROSCALE AND NANOSCALE

By

HUIQING JIN

Dissertation submitted to the Faculty of the Graduate School of the
University of Maryland, College Park, in partial fulfillment
of the requirements for the degree of
Doctor of Philosophy
2004

Advisory Committee:
Associate Professor Hugh A. Bruck, Chair/Advisor, Mechanical Engineering Department
Professor Amr Baz, Mechanical Engineering Department
Professor Abhijit Dasgupta, Mechanical Engineering Department
Associate Professor Bongtae Han, Mechanical Engineering Department
Research Professor Jaime F. Cárdenas-García, Mechanical Engineering Department
Professor Amde M. Amde, Civil and Environmental Engineering Department

ACKNOWLEDGEMENTS

There are many people who have been encouraging, supportive, and inspiring to me in the completion of my Ph.D study. I would like to formally thank these people and express my gratitude for the contributions they have made.

I am very grateful to my advisor, Dr. Hugh Alan Bruck, whose encouragement, support, and guidance have helped me to mature during my PhD studies at Maryland. I really appreciate that he provided me with many opportunities for research experiences beyond the work for my Ph.D dissertation. I want to thank the committee members, Professors Amr Baz, Abhijit Dasgupta, Bongtae Han and Amde Amde for their time and assistance in my Ph.D study.

Special thanks are owed to Dr. Jaime F. Cárdenas-García for providing me with the opportunity to work with the biaxial microtensile tester. Your systematic approach in conducting experiments has been a great help to me.

I would also like to thank Dr. Roytburd from the Materials Science and Engineering department and Tom and Nolen from the EE clean rom for their assistance in the early stage of my Ph.D study.

A big hug goes to my family and my boyfriend for their understanding, love and support. I would like to also thank all of my friends and colleagues, particularly Alan Gershon, Arun Kota, Dan Cole, Dr. Mitch Gallant, and Prof. Yasser Shabana, for their kindness and encouragement.

List of Tables

List of Figures

1 Background and Literature Review

1.1 Nanostructured Materials

This thesis focuses on developing new metrological techniques in characterizing the mechanical behavior of materials, such as nanostructured materials, at the microscale and nanoscale. In this chapter, a description of nanostructured materials, their mechanical and microstructural characterization, along with more advanced full-field deformation measurement techniques developed at the macroscale are discussed. This discussion provides the basis for the motivation behind the metrological advances that were the focus of this thesis.

1.1.1 Description of Nanostructured Materials

Nanostructured materials are materials with microstructural features at length scales normally below 100 nanometers [Gleiter 2000]. The processing, structure and properties of nanostructured materials are research areas with a considerable increase in interest over the past few years. The application of grain refinement has been a powerful tool for designing microstructures with superior properties and performance in metallurgical research. Several drivers have contributed to the rapid increase in the research of nanostructured materials: advances in processing techniques, sophisticated metrology tools with spatial resolution at the nanoscale, and advances in computer hardware and software which have facilitated the development of *new*

multiscale models for simulating structural effects on the deformation of these materials.

According to Gleiter [Gleiter 1995], there are three types of nanostructured materials:

- Materials and devices with nanoscale dimensions
- Surfaces engineered on the nanoscale
- Bulk materials with nanoscale microstructural features

The first category comprises materials and devices with reduced dimensions in the form of nanometer-sized particles, thin wires or thin films. Well-known examples of this category are catalysts and semiconductor devices utilizing single or multilayer quantum structures. The second category comprises materials and devices in which the nanometer-sized microstructure is limited to a thin surface region of a bulk material. Engineered surfaces with enhanced corrosion resistance, hardness, wear resistance or protective coatings are examples for this category. The third category is of more attention in current application and research. The bulk solids have nanometer-scale microstructures. Two classes of such solids can be distinguished: In the first class, the atomic structure and chemical composition vary continuously in space throughout the solids at an atomic scale. It is microstructurally homogeneous as shown in *Figure 1.1*. Glasses, gels, supersaturated solid solutions are examples of this type. In the second class, nanocrystalline materials are assembled with nanometer-sized "building blocks" consisting of the crystalline component and large volume fraction of intercrystalline components as shown in *Figure 1.2* [Gleiter 1989]. These "building blocks" may differ in their atomic structure, crystallographic orientation

and chemical composition. These microstructural building blocks are inherently heterogeneous. It is this inherently heterogeneous structure at a nanometer scale that is crucial for many of their properties, and what distinguishes them from glasses and gels. *This type of nanostructured material is called a "nanocrystalline material", which is the specific material that will be used to characterize AFM nonlinearity in this thesis.*

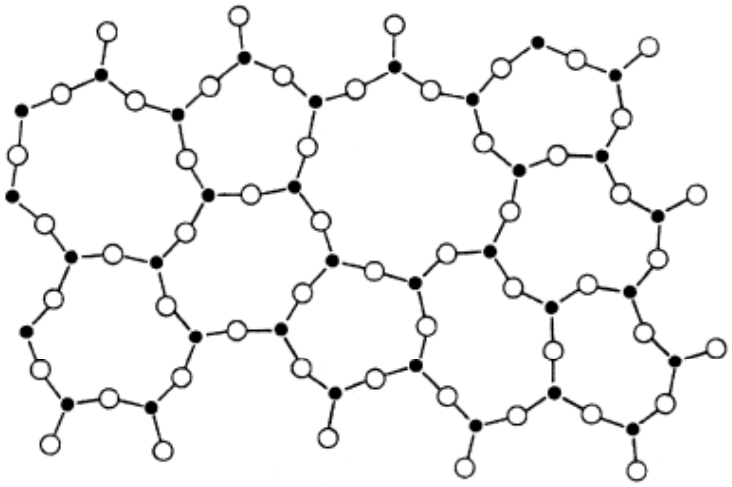

Figure 1.1: Two-dimensional model for an Al_2O_3 glass

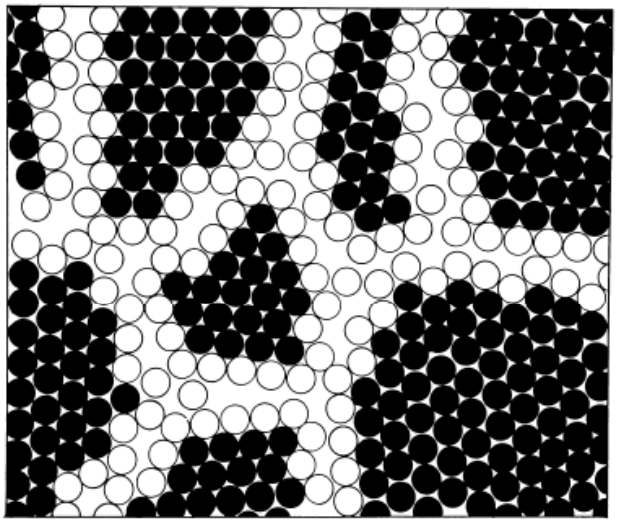

Figure 1.2: Atomic structure of a two-dimensional model of nanocrystalline material. The atoms in the centers of "crystals" are displayed in black. The ones in the boundary core regions are represented by open circles

1.1.2 Proposed Deformation Mechanisms for Nanostructured Materials in Need of Verification

The variation of flow stress as a function of grain size from the microcrystalline to the nanocrystalline regime is schematically shown in *Figure 1.3* [Kumar and Suresh 2003]. In many microcrystalline and ultra fine crystalline metals and alloys with average grain size of 100 nm or larger, strengthening with grain refinement has traditionally been rationalized on the basis of the Hall-Petch mechanism [Hall 1951, Petch 1953]. In metals and alloy with grain size of 100nm or larger, pile-ups of dislocations at grain boundaries were envisioned as a key mechanism underlying an enhanced resistance to plastic flow from grain refinement. As the microstructure is refined from the microcrystalline and ultra fine crystalline regime into the nanocrystalline regime, this process invariably breaks down and the

flow stress versus grain size relationship departs markedly from the “Hall-Petch effect”, and has been recognized as “reverse Hall-Petch effect”.

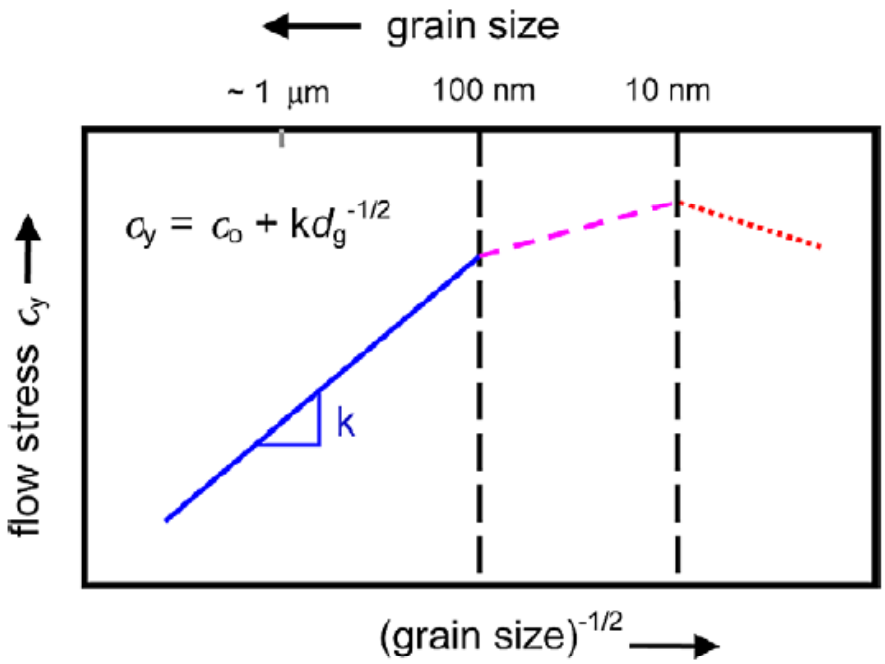

Figure 1.3: Schematic representation of the variation of yield stress as a function of grain size

Many theories have been proposed for the deformation mechanism of nanocrystalline materials [Schiotz 1999]. They can be summarized as follows:

Enhanced Coble Creep. Chokshi *et al* [Chokshi 1989] proposed that inverse Hall-Petch effect is caused by Coble creep, which is the creep due to the diffusion at the grain boundaries. However, direct measurements of the creep rate have ruled out this explanation [Nieman, Weertman and Siegel 1990; Nieh and Wadsworth 1991].

Suppression of dislocation pileups. Once the grain size drops below the equilibrium distance between dislocations in a pileup, pileups are no longer possible, and the Hall-Petch relation should cease to be valid. The critical grain size is estimated to be 20nm for copper [Nieh and Wadsworth 1991]. It is, however, not clear how the yield stress should depend on the grain size below that point.

Different grain boundary structures. It has been proposed that grain boundaries in nanocrystalline metals may be more "transparent" to dislocations, and thus allow dislocations to run through several grains [Valiev 1992; Lian, Baudelet and Nazarov 1993]. This was proposed in connection with measurements of a breakdown of the Hall-Petch relation in metals with sub-micrometer grain sizes, produced by severe plastic deformation [Valiev 1992]. Recent high-resolution electron microscopy studies show, that the grain boundaries in metals produced in this way have a complex structure, with a large number of dislocations very close to the grain boundary [Horita 1996]. This should make the grain boundaries less transparent to dislocations. Further study is needed on the dislocation behavior at the grain boundaries.

Porosity and flaws. If the compaction of nanometer-sized clusters is not complete during inert gas condensation, small voids will be present between the grains. If the nanocrystalline metal contains a significant volume fraction of porosity from the fabrication, this will obviously reduce the hardness significantly.

Deformation in the grain boundaries. Li *et al* proposed a deformation mechanism based on motion of grain boundary dislocations [Li, Sun and Wang 1994].

As summarized above, there are many explanations proposed for the inverse Hall-Petch effect for nanocrystalline materials. Different explanations may apply depending on the different ways that materials are fabricated. For example, inert gas condensation will produce essentially dislocation-free grains in the materials. While severe plastic deformation will produce small grains by breaking up larger grains through intense dislocation activities. It is not unlikely that these different samples have different deformation mechanisms. The use of large-scale molecular dynamics (MD) simulations has provided insight into the atomic scale processes that may occur during plastic deformation [Schiøtz 1998, Van Swygenhoven 2002, 2003]. However, simulations should therefore be regarded only as a source of inspiration and quantitative guidance and not as a means to validate or disprove the existence of a mechanism. *The mechanisms still need to be experimentally explored and the comparison between simulation and experimental results need to be conducted.*

In considering the structure of nanocrystalline metals and alloys and its impact on deformation behavior, the role of grain boundaries is clearly paramount. Computations have shown the effects of atomic structure of the boundaries (boundary type and boundary stresses) on the behavior of grain boundary (GB) such as grain boundary sliding and the capacity of a GB to emit dislocations into a grain and absorb dislocations. *While these theories seem plausible, there is currently little direct or indirect experimental evidence to support the computational finding even for simple tensile deformation.* Clearly, there is a need for experimental efforts dedicated to characterizing grain boundary structures in nanocrystalline metals and their response to applied stress. Furthermore, experimental validation of computations is required at

a more fundamental level rather than at the level of macroscopic mechanical properties such as hardness and strength.

Microstructural characterization has also not been systematic and as a direct consequence, the connection between structure and mechanical properties has not been well established in many nanocrystalline metals and alloys. Even the relatively simple characteristics, such as *texture, grain size distribution, grain morphology* through the cross section, and population of *growth twins*, are often not well defined. *However, in order to create maximum synergy between simulation and experiment, there is a need to advance metrological techniques to provide detailed information on the microstructure, such as a distribution of the lattice misorientation and the GB plane misorientation.* Information of such type would facilitate a more direct simulation of the sample in the computational model.

1.1.3 Mechanical Characterization of Thin Films

Nanostructured materials are commonly found in the form of nanoscrystalline thin films. Nanocrystalline thin films are used in many technical applications, such as semiconductor devices, information storage media, microelectromechanical systems (MEMS), and biomedical devices. The knowledge of materials properties is essential for the design and fabrication of these devices [Kraft 2001]. The mechanical properties of thin films differ significantly from those of bulk materials due to the effects of fabrication processes, interfaces, microstructure, and the presence of thick underlying substrates. There has been a substantial increase in thin films on silicon substrates used in MEMS devices. The mechanical properties of these thin films need to be well characterized in order to exploit the applications of these materials.

Specialized experimental techniques have been developed to determine mechanical properties of both free standing films and films bonded to substrates. These techniques include: *small-scale tension testing*, *small-scale bend testing* (including axisymmetric plate bending, beam bending, wafer curvature test), *bulge testing*, *resonant frequency testing*, and *nanoindentation testing* [Srikar 2003]. The introduction of the substrate may complicate the experimental measurement of thin films because: 1) the microscale material properties of the substrate material itself may not be well understood, and 2) the interface between the substrate and the thin film may affect the mechanical behavior of the thin film. [Nix 1989]. Therefore, it is most desirable to test freestanding thin films.

Tensile testing is generally considered the most reliable method to measure the mechanical properties of free standing thin films. There have been great efforts on applying this technique to the testing of thin films and MEMS materials. Koskinen *et al* [Koskinen and Johnson 1993] first developed a procedure to directly measure mechanical properties of free standing fiber fabricated from thin films. These thin film fibers had cross-section of 1 micron by 3 micron. A grid of parallel specimens was mounted between two large grips. One of the grip ends was fixed, and the other end was rotated and pulled. The specimens were straightened and individually broken to measure the tensile strength and elastic modulus. Mearini and Hoffman [Mearini and Hoffman 1993] reported the first *microtensile tester*, which was capable of generating 0.1N of uniaxial force and was used to test a single specimen with a geometry of 0.5-1.5 mm x 150 um x100nm fabricated from an aluminum film. Ruud *et al* [Ruud 1993] used motor-driven micrometers to produce elongation in thin films,

a load cell to measure the force, and laser spots diffracted from the gratings on the specimen surface to determine the strain. After that, Read [Read 1998] developed a piezoactuated tensile testing apparatus with a force resolution of 200μN and displacement resolution of 20nm. The testing apparatus was used to characterize 700 x 200 x 1.2 μm multilayered aluminum thin film specimens. Tsuchiya *et al* [Tsuchiya and Tabata 1997] used electrostatic gripping to enable easy testing of a large number of specimens, but concentrated mainly on the tensile strength of polysilicon thin films. Sharpe *et al* built tensile tester to measure the Young's modulus and strength for polysilicon specimen [Sharpe, 1997, 1999]. Both axial and lateral strains were measured directly by laser interferometric strain/displacement gage (IDSG) from the relative displacement between the two gauge markers on the specimen. These markers are gold lines that were deposited on the specimen during fabrication of the specimen for the reflection of the laser.

Haque and Saif [Haque 2001] presented a methodology for uniaxial tensile testing and cantilever bending testing of free standing specimens using MEMS actuators. The tensile forces were applied by lateral comb drive actuators capable of generating a total load of 383 μN at 40V with resolutions on the order of 3nN. The tensile testing methodology was demonstrated with the testing of 110nm thick free standing aluminum specimen. The experimental setup can be mounted in an SEM for *in situ* observation of mechanical deformations.

Finally, Chasiotis and Knauss [2002] developed a method for uniaxial microtensile testing of polysilicon using an electrostatic gripping and measuring strain at the micro-nanoscale using images of the microstructure obtained with an

Atomic Force Microscope (AFM). This approach has demonstrated a great deal of potential, however it is currently limited to MEMS structures because of the method for gripping the specimen and the use of the AFM to image microstructural features that are tracked to determine uniaxial elastic deformations. *There is a need to improve this technique to handle biaxial testing of thin films and to understand how AFMs can be used not only to characterize the microstructure of materials, but to also measure the inhomogeneous deformations associated with the grain structure of the films.*

1.2 Microstructural Characterization at the Microscale and Nanoscale: Atomic Force Microcopy (AFM)

1.2.1 Concepts and Applications of AFM in Surface Imaging

Atomic Force Microscope (AFM) was invented for surface imaging at the microscale and nanoscale by Binnig *et al* [Binnig 1986] to overcome the limitation of STM, which is unable to image insulating materials. Paredes *et al* presented a comprehensive review on the applications of AFM to inorganic materials such as metals, silica, alumina, oxides and nitrides, carbon materials, organic and biological materials [Paredes 2003]. The working principle of the AFM is to use the interaction force between a tip and sample to image a surface, unlike the case with scanning tunneling microscope (STM) which uses a current. The main components of an AFM include [Rugar and Hansma, 1990]:

(a) A sharp tip mounted on a cantilever spring

(b) A way of sensing the deflection of cantilever

(c) A feedback system to monitor and control the deflection of the cantilever

(d) A mechanical scanning system to control the tip relative to sample

(e) A display system that converts the measured data into an image

The details of the implementation of these components may vary for different AFMs. Most AFM cantilevers today are microfabricated from silicon, silicon oxide and silicon nitride using photolithography. The optical detection was used to detect the cantilever's deflection. Optical detection schemes are divided into two basic types: *Interferometry* and *beam deflection*. In the typical beam deflection AFM, laser light is reflected from the mirror-like surface of the cantilever and the intensity of the light is sensed with a photo detector. Rugar *et al* developed a cantilever deflection based on a fiber-optical interferometer [Rugar 1988]. The advantage of fiber-optic interferometry is that it can be used with cantilevers that do not have a reflection coating. The introduction of commercial AFM instruments based on micromachined cantilevers and optical deflection techniques that operated under ambient conditions found wide appeal in the scientific community and stimulated many applications.

The AFM works much the same way as a profilometer works only on a much, much smaller scale: a very sharp tip is dragged across a sample surface and the change in the vertical position (denoted the "z" axis) reflects the topography of the surface. The concept of AFM tip is shown in *Figure 1.4.* By collecting the scanning motion of the tip for a succession of lines, three-dimensional map of the surface features can be formed. AFM typically operates in the micrometer to nanometer range. An upper limit of the current scan range can be up to $150\mu m \times 150\mu\text{m} \times 20\mu\text{m}$ for the axes x, y and z. The resolution of image can be up to 1024 pixels by 1024 pixels.

There are three different interaction modes between tip and sample. The AFM working principle is based on these interaction modes. As the tip approaches the sample surface, they first weakly attract each other due to van der Waals forces. This attraction force increases until the atoms are so close that their electron clouds begin to repel each other electrostatically. This repulsion force progressively weakens the attractive force as the tip continues to approach the sample. The attractive force becomes zero when the distance between the atoms reaches about the length of a chemical bond. When the total force becomes repulsive, the atoms are in contact.

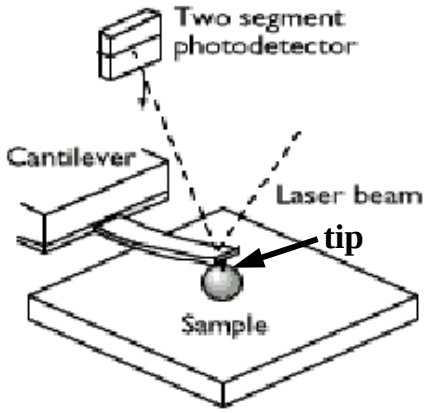

Figure 1.4: Concept of AFM and the optical lever

The most common mode of the operation of AFM is “contact mode”, the scanning tip touches the sample surface during scanning. The interaction force during the contact mode is typically 10^{-7} N, which is nondestructive for most materials. The AFM operates by measuring attractive or repulsive forces between the tip and the sample. The tip is kept in contact with the sample by a feedback circuit. When the tip is deflected by the sample, the cantilever is forced upwards. Thus the feedback

controller will detect this reflection and sends a signal to the piezo driver in order to keep the contact force constant. The feedback signal is recorded during the scanning process and then used to map the sample's height distribution. One of the drawbacks of remaining in contact with the sample is that there exist large lateral forces on the sample as the tip is "dragged" over the specimen.

Tapping mode, or intermittent mode, is the next common mode used in AFM. The cantilever is oscillated at its resonant frequency (often hundreds of KHz) and positioned above the surface so that it only taps the surface for a very small fraction of its oscillation period. The lateral forces are dramatically reduced as the tip scans over the surface. When imaging soft samples, tapping mode may be a far better choice than contact mode. With the tapping mode, both topographic and phase images can be obtained. The phase image monitors the phase lag between the signal that drives the cantilever and the output signal of the cantilever. Thus both the topographic information and other additional physical properties can be obtained simultaneously during scanning.

Another work mode of AFM is called "noncontact mode". The tip and sample are not contacting with each other during the scanning process. The tip is excited to oscillate close to its resonance frequency. By keeping the amplitude of the oscillation constant as feedback signal, the topographic information can be achieved. With the noncontact mode, the phase image can also be obtained which maps the variations in surface properties. The topographic images record the microscale and nanoscale structure of the sample surface, such as defects and grain boundaries. The phase image records the phase difference between input and output signal, which can reflect

the material property changes on the sample surface. When a feature is shown in the phase image but not in the topographic image, it is due to the variation of material properties in that area even there is no variation in the structure feature. But in the noncontact mode, the cantilever must be oscillated above the surface of the sample at such a distance that the tip is no longer in the repulsive regime of the inter-molecular force curve. This is a very difficult mode to operate in ambient conditions with the AFM since the associate forces are in the range of 10^{-10} N.

The presence of a feedback loop is one of the subtler differences between AFMs and older stylus-based instruments such as stylus profilometer. The AFM not only measures the force on the sample but also regulates it, allowing acquisition of images at very low forces. A schematic diagram of AFM feedback loop is shown in *Figure 1.5.* The feedback loop consists of the tube scanner that controls the height between the sample, the cantilever and optical detector which measures the local height of the sample, and a feedback circuit that attempts to keep the cantilever deflection constant by adjusting the voltage applied to the scanner.

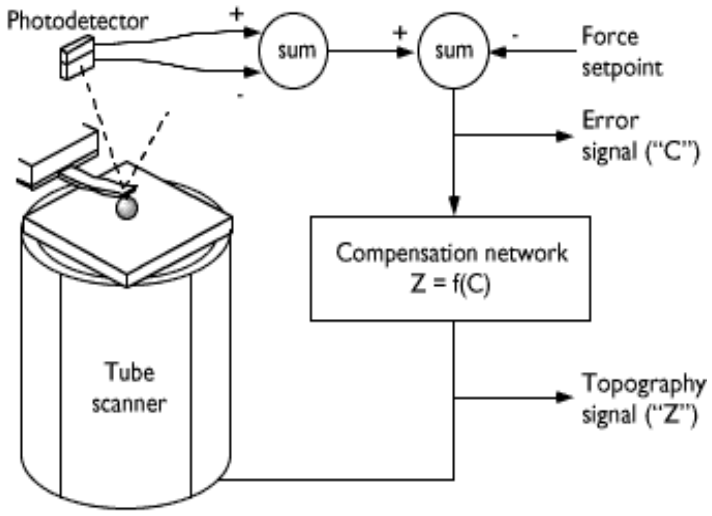

Figure 1.5: The AFM feedback loop

1.2.2 Application of AFM Imaging in Mechanical Characterization

AFM imaging has proven to be an extremely effective tool for microstructural and mechanical characterization at the microscale and nanoscale. Harvey *et al* [Harvey and Marsh 1994] first used atomic force microscope (AFM) to obtain images of cell-like boundaries and slip band emergence of fatigued titanium and high strength alloy steel surfaces. The samples were first fully underwent fatigue cycling and then were scanned to obtain AFM images. These AFM images were used to obtain quantitative information about slip spacing and slip height displacements. These measurements can then be used to determine the fraction of cumulative plastic strain.

Tong *et al* [Tong and Weiland 1997] presented a technique that combines AFM and Orientation Imaging Microscopy (OIM) to measure grain surface topography of binary aluminum alloy during *in situ* tensile testing. Sets of AFM images of aluminum grains were obtained during the increment of the strain. Nanometric-scale roughness features such as slip bands and grain boundaries can then be measured corresponding to the different strain level. Cretegny *et al* [Cretegny 2001] used AFM to study the development of slip bands and protrusions in strain controlled fatigue tests on polycrystalline copper. Chandrasekaran and Nygards [Chandrasekaran and Nygards, 2003, 2004] have studied the surface deformation of ultra-low-carbon ferritic steel with two different grain sizes using AFM after different plastic strains. Different parameters, such as surface roughness and change in misorientation with strain were evaluated. Bhushan *et al* [Bhushan 2001a, 2001b,

2003] used an AFM to study the cracks developed on thin film coatings on a polymer substrate subjected to external tension. A stage was built to control the motion of the film so that the AFM can scan over the same area during deformation. This technique was also used to study the crack propagation in the magnetic tapes. Also, a technique was developed by this group to measure the Poisson's ratio of ultra thin polymeric films used as substrates in magnetic tapes. Using features and surface height profiles obtained from AFM images, both longitudinal and lateral displacements can be measured and the Poisson's ratio can be calculated from these displacements. Dasari *et al* [Dasari and Rohrmann, 2003, 2004] used the AFM to determine the extent of surface damage induced by the scratch test in different grades of polypropylenes and ethylene propylene di-block copolymers. The extent of surface damage was evaluated in terms of average surface height of the plastically deformed region, depth of the scratch tracks, thickness and density of the scratch tracks. Therefore, the ability of the polymeric materials to resist scratch deformation can be determined. AFM has also been used to investigate the nanodynamics of human brain tumor cells on collagen substrates [Chasiotis and Fillmore 2003]. The behavior of tumor cells and their response to the presence of neighboring tumor cells have been explored. *Based on the results from these investigations, the AFM has the potential for being an effective technique to visualize full-field deformations at the micro-nanoscale through the tracking of microstructural features*. The efficacy of this technique will depend on the accuracy of acquiring images under load and the image analysis techniques used to track them.

1.3 Full-Field Deformation Measurement Techniques

1.3.1 Digital Image Correlation Technique

Digital image correlation is a full-field deformation measurement technique that mathematically compares a subset of a digital image from a reference configuration with a digital image from a deformed configuration. It has become an accepted method for measuring the surface displacement and displacement gradients in solid mechanics. It was originally proposed and used by researchers at the University of Southern Carolina [Peters 1982, Chu 1982, Sutton 1983, Sutton 1986, Bruck 1989]. This technique uses gray or laser speckles patterns on the specimen to obtain the deformation of a surface via comparison of the digitalized undeformed and deformed images. Different mathematical approaches have been used to determine the displacement and deformation values that minimize the correlation function, such as coarse-fine search [Chu and Peters 1982, Sutton 1983], Newton-Raphson method of partial differential correction [Bruck 1989], Hessian matrix computation [Vendroux 1998] and genetic algorithm [Brooks 1996, Piazza 2001].

In most of the previous work [Chu and Peters 1982, Sutton 1983, 1986, Bruck 1989, Luo 1993], a first-order, linear approximation of the deformation is assumed. This approximation holds well when the subset size is small and deformation is small. However, a unique gray-scale pattern may not exist in a very small subset, requiring the use of larger subset sizes. As the size of the subset increases, the linear approximation of the deformation may become less accurate. Higher-order deformation approximations can be used to provide more accurate descriptions of the displacement fields in large subsets. The large deformation formulation has been used

to determine the deformation field in large rigid body rotations. Lu and Cary [Lu 2000] refined the DIC method by using second-order displacement gradients for deformations when higher order displacement gradients occur. *While higher-order deformation approximations can provide more accurate descriptions of non-linear displacement fields, they become extremely complex when the deformation is rapidly varying or discontinuous.*

There have been many applications of DIC technique to measure the deformations of materials, include metal sheets, biological materials, composite, nanocrystalline coatings, smart materials and functionally graded materials. It has been used to characterize the mechanical response of thin steel sheets under tensile tests. DIC is used to map the full field deformation, characterize the necking and its propagation up to failure [Husson 2002, Wattrisse, 2001]. Zhang *et al* used DIC to evaluate the mechanical behavior of biological tissues [Zhang 2002, 2004]. A review of DIC applications in composite materials has been presented by Grediac [Grediac 2004]. The advantages and limitations of DIC were examined regarding to the applications of composite materials. Bruck *et al* used DIC to measure the bending actuation of polyurethane with shape memory alloy wire embedded inside [Moore 2002, Bruck 2002, 2004]. Wang *et al* applied DIC technique to capture the heterogeneous deformation fields during the compression of ultra-light polymeric foams [Wang 2002].

1.3.2 Moiré Method

Based on the interference of two moiré gratings (lines with periodic spacing), the geometric moiré method has been a useful tool for displacement measurements. It has been used to measure the deformation of specimens and to study the fracture of specimens [Parks 1987, Chona 1995]. High spatial resolution and high sensitivity microscopic moiré was developed by Wang and Dai [Wang 1999, Dai 1999]. The frequency of the reference gratings can be up to 1000 lines/mm.

The use of laser light has led to a significant development in the moiré method: a completely new method known as *Moiré Interferometry*. Post and Han summarized the method comprehensively. The moiré interferometry method uses the interference of two laser beams to form a moiré grating [Morimoto 1989, Post 1980, 1991]. The major advancement of the moiré interferometry method over the geometrical moiré method is the increase of frequency from about 50 lines/mm to 2400 lines/mm. The moiré interferometry method is useful for high accuracy measurement. Its applications have also proven to be feasible for microscopic measurement.

Han *et al* pushed the frequency of moiré gratings up to 4800 lines/mm [Han 1992, 1996]. However, further increase in grating frequency is hindered by the wavelength of laser light. To increase the frequency and hence the sensitivity of the moiré method, a technique independent of light source is preferred. Through a technique called the Electron Beam Moiré method, Kishimoto *et al* combined electron beam lithography and an SEM for microscopic measurements [Kishimoto 1993]. The Electron Beam Moiré (also known as SEM moiré) method is another

significant development in moiré methods. It is especially useful for measurements of microscopic deformation and has proven to be a reliable technique. Dally and Read investigated the details of the technique and established the fundamental theory of the SEM moiré method [Dally 1993a]. Dally and Read demonstrated that a frequency of 10,000 lines/mm or higher was possible [Dally 1996]. They have used the SEM moiré method to measure microscopic deformation of fiber-reinforced composite materials [Dally and Read 1993 b, 1993c, 1994]. The extension of its applications to electronic packaging has also been reported [Read and Dally 1995a, 1995b, Drexler 1999a, 1999b].

Xie *et al* developed a new scanning moiré method to measure the in-plane deformation of mica at the micro-nanoscale using an AFM [Xie, 2000]. Moiré patterns are formed by the scanning lines of the CRT display in the AFM system and the atomic lattice of mica or high-orientated pyrolytic graphite (HOPG). This new method was used to measure the residual deformation of a mica plate after irradiation by a Nd-YAG laser, and to determine the residual strain of HOPG under a tensile load. The AFM scanning moiré technique has also been applied to measure the thermal deformation of electronic packages successfully. This technique is convenient to perform the mismatch measurement. Also it could be obtained at a higher resolution than any other moiré method [Lu 2001, Zhong 2004a, 2004b]. Xie *et al* explained the formation mechanism of AFM moiré using the transmittance function and described the technique for preparing the AFM moiré specimen grating [Xie, 2002]. The sensitivity and accuracy of this method was also analyzed. This method was used to measure the shear strain at the different solders in the ball grid array

(BGA) electronic package. The result was compared with that from electron beam moiré method.

Liu *et al* developed a novel digital AFM moiré method to measure the displacement and strain fields [Liu and Chen 2004]. The difference between the previous AFM scanning moiré method and the digital AFM moiré method was that the reference scanning line grating was replaced by the virtual reference grating formed by digital image processing. The overlapped images from the specimen grating and reference grating were filtered by wavelet transformation to obtain clearer moiré patterns. By examining the resultant moiré patterns, the displacement and strain fields can be obtained. From experimental results, it was found that this technique was a convenient and efficient method to obtain deformation measurements at the nanoscale. However, it was still limited to the accuracy of constructing the virtual reference grating and filtering the overlapped image. *Therefore, it is desirable to determine deformations at the microscale and nanoscale directly from AFM images using a technique like DIC with the spatial resolution of the moiré method*.

2 Research Objectives and Research Approach

The previous chapter provided the motivation for the research objectives and the research approach that are described in this chapter. The specific research objectives and research approach are focused on addressing the need for measuring deformations at the microscale and nanoscale.

2.1 Research Objectives

As discussed in the previous chapter, there is a great deal of interest in studying the relationship between the processing, structures and properties of nanostructured materials. For example, how will the presence of a large volume fraction of grain boundaries play a role in the deformation of these materials? How will the deformation be affected by 2-D stress states? Answers to questions such as these are currently being predicted using advanced computational models. These models have been used to identify many possible explanations for the deformation mechanism of the nanostructured materials. For example, simulations based on molecular dynamics have provided insight into the atomic scale phenomena that may occur during plastic deformation. However, these mechanisms still need to be experimentally explored, and comparisons between simulation and experimental results need to be conducted to validate fundamental assumptions in these models.

One key assumption that is used in the computational models is the nature of the deformation mechanisms in a material. Unfortunately, the relationship between

deformation mechanisms and microstructural characteristics has not been very systematic. Microstructural characteristics such as texture, grain size distribution, grain shape through the cross section, and population of growth twins are often unique to a given material. The connection between these characteristics and mechanical properties has not been well established in many nanostructured materials. However, in order to create maximum synergy between simulation and experiment, detailed information on these relationships would facilitate an exact representation of the sample in the computational model. Therefore, an experimental technique is needed to mechanically characterize materials both at the microscale and nanoscale. The deformation of the materials needs to be measured at the microscale and nanoscale when the material is under load.

The research objectives here are to develop new metrological techniques to characterize the mechanical behavior of thin films and nanostructured materials at the microscale and nanoscale. The advantages of these new techniques are as follows:

(1) *Biaxial mechanical characterization with in situ measurement of full-field deformation*: Materials need to be characterized in more complex stress states than uniaxial. Biaxial mechanical characterization provides a more realistic -2-D stress state for certain geometries, such as membrane structures. With the *in situ* full-field deformation measurement capability, this technique can provide more insight into the nature of deformation mechanisms at the microscale and nanoscale.

(3) *Characterization of Imaging Accuracy of the AFM*: Measurements can be made at a spatial dimension comparable to the size of the microstructure of

nanostructured materials using an objective AFM. This capability makes it possible to study full-field deformations inside the microstructure and at interfaces such as grain boundaries. However, the accuracy of the surface imaging must be characterized to obtain actual deformation measurements.

(3) *Discontinuous full-field displacement measurement over an area of interest*. This capability provides details on the displacement field for each point in an AOI, which can be used to determine the strain field instead of the average strain over the area. Thus, this technique provides more detailed information to study the relation between microstructural features and mechanical properties.

2.2 Research Approach

The research approach undertaken in this thesis consists of three parts:

1. Development of a control system and integrated imaging capability for a new biaxial microtensile tester that is suitable for *in situ* microscale and nanoscale mechanically characterization of thin films and MEMS structures
2. Characterization of the imaging accuracy of an objective AFM used to visualize *in situ* deformation of materials at the microscale and nanoscale
2. Modification of the DIC image analysis technique to determine discontinuous full-field deformations from the images

Each of these parts is now briefly described:

Development of a Control System and Integrated Imaging Capability for a New Biaxial Microtensile Tester: Microtensile testing has been developed to study the mechanical properties of free standing thin films and MEMS structures. Progress

on accurate load control and miniaturized load cells has made tensile testing of specimens at the micron scale possible. Some efforts have been made to utilize visualization tools in tensile testing systems to study the specimen after deformation. SEM and AFM are the two most common instruments to obtain images for studying the deformation response of a specimen, but the current use of these instruments is limited to the deformation study after the material has undergone plastic deformation and after the load has been removed from the specimen. They cannot observe the evolution of deformation with each increment of load. In this part of the research approach, a novel biaxial microtensile testing system is constructed with integrated advanced imaging techniques for quantifying microstructural deformations *in situ* using an advanced image analysis technique. The challenge in this research approach is to design the testing system to demonstrate adequate load control for achieving a biaxial loading state and to obtain suitable imaging stability for *in situ* deformation measurements.

Accuracy of Advanced Imaging Technique: Atomic Force Microscopy (AFM) is an advanced imaging technique used to image both conductive materials and insulating materials. It has high resolution both in the x-y plane and z direction. It is generally operated under ambient conditions. These features of AFM and the commercial availability of AFM cantilevers make it appealing in the study of the surface features and nanostructured materials. It is also available in the form of a microscope objective that is suitable for integration with a variety of testing systems. However, it suffers from hysteresis of the piezo scanning element that causes nonlinearities during scanning that result in artificial distortions of the AFM images.

The challenge in this research approach is to integrate the AFM into the testing system and to characterize the distortion of images during *in situ* image acquisition in order to determine the accuracy of the imaging technique.

Modification of DIC Image Analysis Technique: The DIC technique is a full-field deformation measurement technique that mathematically compares a subset of intensity values from a digital image of a reference configuration with a digital image of a deformed configuration. It has become an accepted method for measuring the surface displacement and displacement gradients in solid mechanics using conventional white light digital cameras and painted speckle patterns. However, the analyses are obtained over subsets of an image that can smooth out discontinuities associated with microstructural features. Therefore, the conventional DIC technique was modified to permit pointwise determination of discontinuous displacement fields within a subset.

The specific tasks associated with the research approach are as follows:

1. Develop a control system for a new biaxial microtensile tester that is used for characterizing the mechanical behavior of thin films and MEMS structures.
2. Integrate an optical microscope and objective AFM into the microtensile testing system to obtain *in situ* microscale and nanoscale images.
3. Apply the DIC technique on the textured gray scale images which are obtained from AFM topographic images.
4. Determine the nonlinearity of AFM imaging and mitigate the error from the displacement measurement.

5. Study the effects of Genetic Algorithm (GA) parameters on the correlation function value and the convergence rate.
6. Develop the theoretical foundation for pointwise DIC, which is used to measure the discontinuous displacement field across interfaces and cracks.

2.3 Dissertation Organization

The dissertation is organized as follows. In Chapter 1, the motivations and the state-of-the-art of the new techniques for the mechanical characterization are reviewed. In Chapter 2, the research objective and the research approach are summarized. The details of the research that was conducted are discussed in Chapters 3 to 6. In Chapter 3, the development of the control system and integrated imaging capability for the biaxial microtensile testing system are discussed, while the conduction of biaxial testing at the microscale and the uniaxial tensile testing at the nanoscale will be described in detail in Chapter 4. In Chapter 5, a new technique using DIC to characterize the nonlinearity of AFM imaging will be discussed in detail. In Chapter 6, the theoretical development of pointwise DIC will be presented in detail, as well as a parametric study of a Genetic Algorithm optimization method for quickly and accurately determining the large number of displacements variables associated with the pointwise DIC technique. The scientific and technological contributions along with proposed future work are summarized in Chapter 7.

The dissertation organization is summarized in the following schematic diagram:

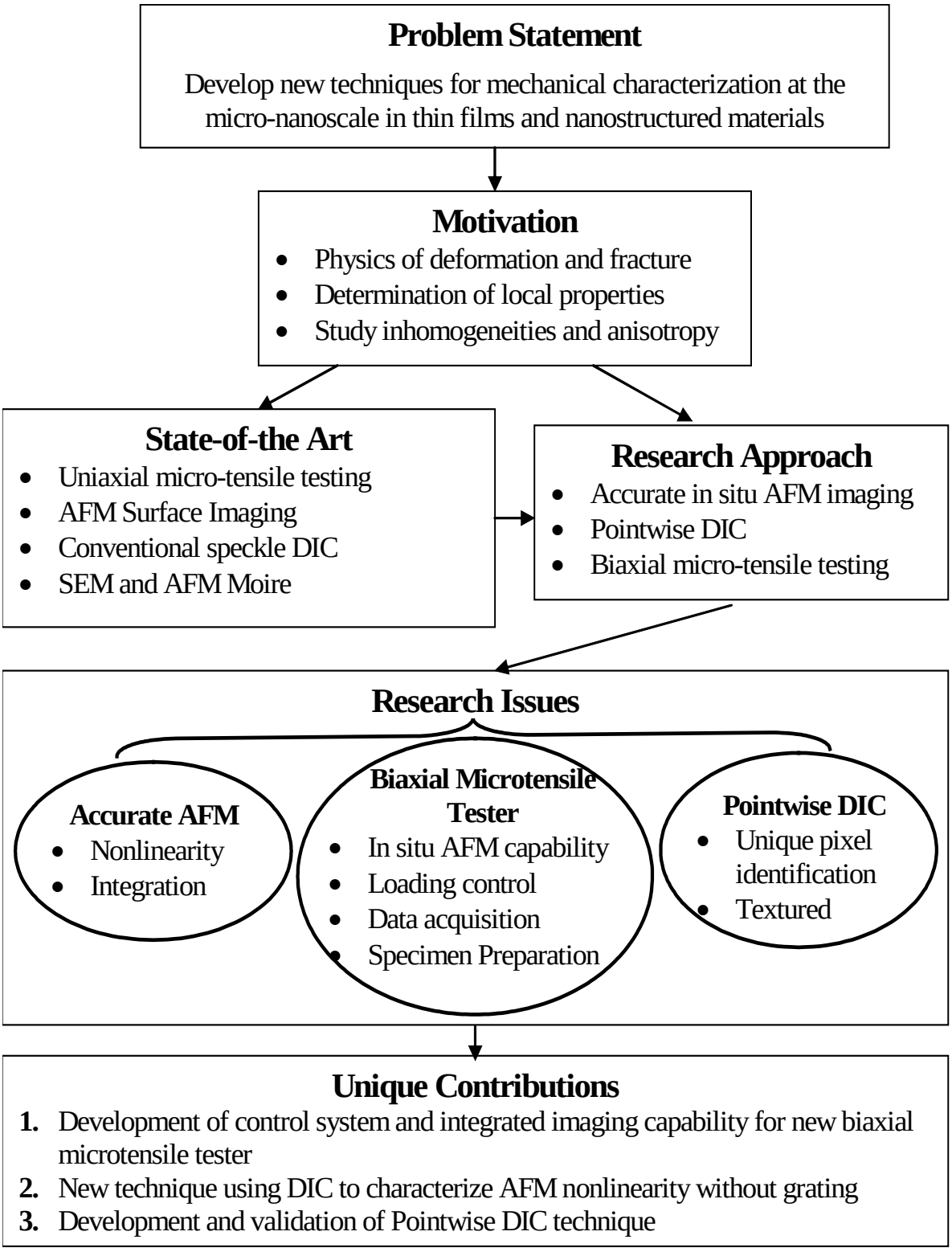

Figure 2.1: Schematic diagram of dissertation organization

3 Development of Control System and Integrated Imaging Capability for New Biaxial Microtensile Tester

In this chapter, the design and construction of the biaxial microtensile testing system is briefly introduced. For the work presented in this thesis, an objective AFM has been integrated into the biaxial microtensile testing system to obtain images with nanoscale resolution, while an optical microscope has been integrated to obtain images with microscale resolution. Also, a control system has been implemented for loading specimens and recording loads during a biaxial microtensile test, which will be discussed in detail.

3.1 Design and Construction of Biaxial Microtensile Testing System

3.1.1 Design of the Biaxial Microtensile Testing System

The design of the biaxial microtensile testing system includes several basic issues [*Cardenas-Garcia et al* 2004, in Review]:

(1) Accommodating specimens of different sizes

(2) Alignment and handling of specimen

(3) Actuation and control of the loading system

(4) Load measurement

(5) Deformation measurement

A schematic diagram of the conceptual design of the biaxial microtensile testing system is shown in *Figure 3.1*. The conceptual design reflects that the specimen is the central part of the whole design. It is mounted to the testing machine using an adhesive on the grip ends. The loading system includes:

(a) Vibration isolation table on which the microtensile testing system sits

(b) Mechanical frames comprising the base for the components

(c) Specimen grips

(d) Air bearing stages to eliminate friction during movements

The visualization system includes a microscope to monitor the handling of the specimen and a CCD camera to record digital images with microscale resolution. The force transducer system monitors the force being applied to the specimen during testing and has to be precisely aligned with the grips so that the effects of gravity and friction are minimized. The displacement transducer system includes the motorized picomotor actuators used to introduce the global axial deformation, and the objective AFM which is capable of independently measuring local displacements in an AOI on the specimen surface.

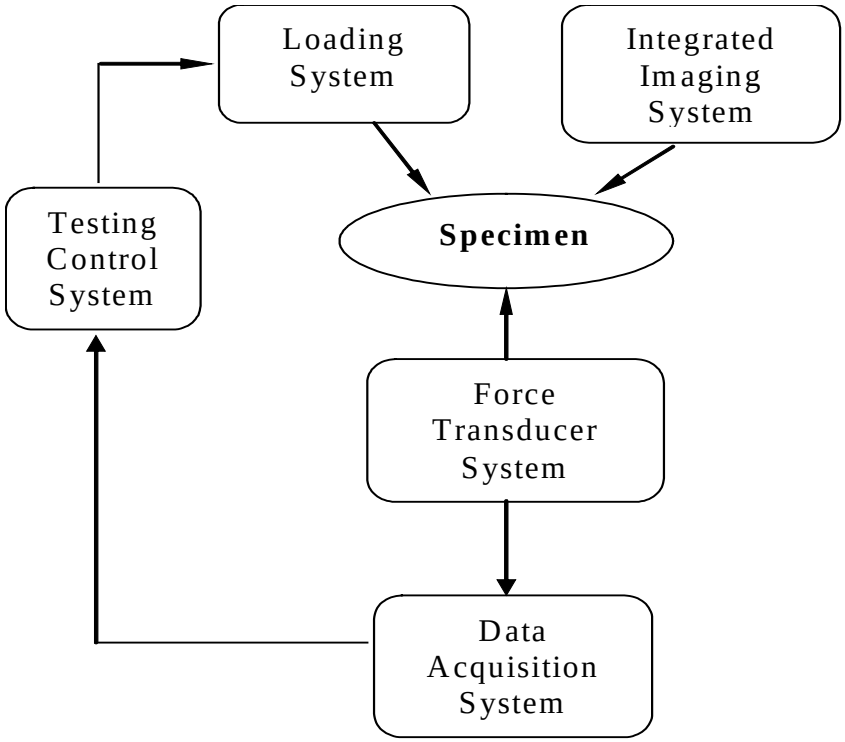

Figure 3.1: Conceptual design of the biaxial microtensile testing system

[adapted from NSF Proposal, 2000]

3.1.2 Construction of the Biaxial Microtensile Testing System

To satisfy the design requirements, each component of the biaxial microtensile testing system should be selected to fulfill certain requirements. It should be possible to apply the load in one axis for uniaxial testing and in both x and y axes simultaneously for biaxial testing. Also the loading should be easy to control and should have fine incremental steps. Picomotor actuators from New Focus Company are ideal devices for displacing the fine positioning stages. They have less than 30nm resolution, and can exert up to 5lb force. They have long-term stability and the ability to hold their position steady without continuously applying power. These last two

features are very important since the specimen needs to be held stationary during image acquisition.

In the biaxial microtensile testing system, the load was continuously measured by a miniature load cell throughout the test. The load cell LFS 270 from Cooper Instruments and System Company is a miniature tension/compression load cell. It has the unique combination of compact size and high load capacity. It has linearity error of less than 0.1% of full scale and repeatability error less than 0.05% of full scale. Three different scales of 100 grams, 1 lb, and 2 lb provide a range of loading capabilities depending on the specimen properties and dimensions. These three load levels can be obtained by simply replacing the load cell without changing the overall configuration of the biaxial microtensile tester. The picomotor and load cell are shown in *Figure 3.2.* A CCD camera can be mounted along the optical axis of the microscope for specimen alignment and positioning.

(a) (b)

Figure 3.2: (a) Load cell (b) Picomotor actuator

3.1.3 Integration of Imaging Capability into the Biaxial Microtensile Testing System

In the biaxial microtensile testing system, the full-field displacements and strains were obtained by using the DIC technique to images that are obtained from the specimen during the process of the loading. An objective AFM scanner head can be mounted to the microscope objective piece holder to obtain images with nanoscale resolution. The AFM used in this work is DualScope^{TM} DS-45 from Danish Micro Engineering A/S. It has scanning range of 40x40 microns in x-y plane and scanning height of 2.7 micron in z direction. A microscope objective piece and CCD camera can also be used to obtain images at lower magnification with micrometer resolution. The microscope was attached to a stage with x, y and z three-dimension motion. This enables the AFM or the microscope objective to be positioned over the AOI of the sample. The configuration of the main components of the biaxial microtensile tester is shown in *Figure 3.3.*

The digital camera can be used to record speckle patterns on the surface of a specimen with a resolution of 1280 by 1024 pixels, while the AFM can be used to record the specimen surface topography with a resolution of up to 1024 by 1024 pixels at the end of each incremental step of load. Undeformed and deformed images can then be correlated using the DIC technique in order to resolve full-field displacement over the AOI with either sub-micron or sub-nanometer resolution. Therefore, the mechanical behavior of the specimen can be obtained from the global load recorded using the load cell, and the local displacement obtained from the AFM and optical microscopy images using the DIC technique. At low AFM spatial resolution, averaged strains can be measured to determine macroscale mechanical

properties, while high-resolution images can be used to investigate the microscale and nanoscale deformation at microstructural features that are critical to understand the physics behind the mechanical behavior of the material.

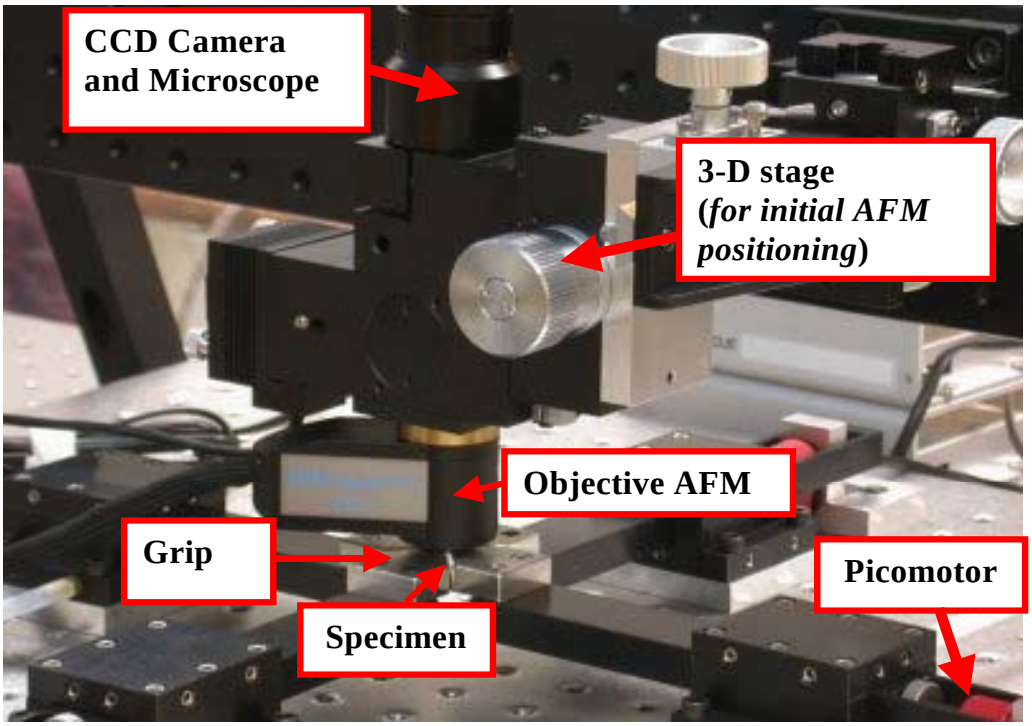

Figure 3.3: Experimental configuration of main components for biaxial tensile testing system

3.2 Control of Microtensile Testing System using PXI and LabView

3.2.1 Control of the Loading System

3.2.1.1 Hardware Configuration of the Control of the Loading System

In order to have computer control of the drivers using the DLL library, the picomotor and its controller need to be set up as shown in *Figure 3.4*. Each driver is responsible for controlling one picomotor. The four drivers for biaxial testing are

serial interconnected between each other using a RJ-45 cable. The first driver in the drivers network is connected to one of computer COM port using module 8761. Then the computer can communicate with the driver using a RS-485 interface.

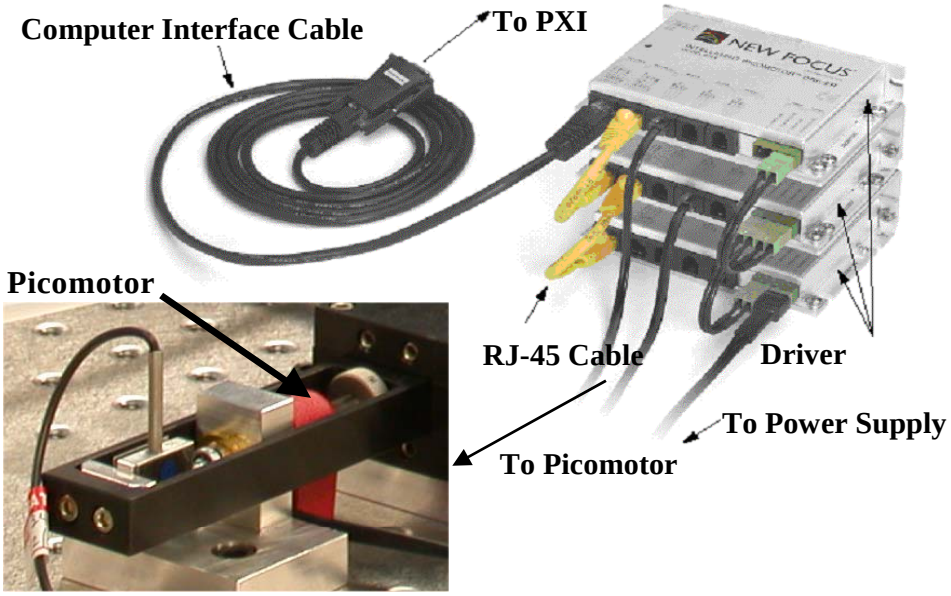

Figure 3.4: Hardware configuration of picomotor and its control system

3.2.1.2 Control Program for the Loading System

A LabView program is developed to control the drivers, and thus control the motion of the picomotors. The main SubVIs library tree used in the control program for a picomotor is shown in *Figure 3.5*. These SubVI programs are responsible for functions such as motor initialization, motor positioning, error notification, control of motion speed and direction. They are embedded into the main control program to build up the library tree to control the motion of the picomotor. *Figure 3.6* shows the typical graphic interface of the control program for a single picomotor. ComPort and

Address options define which motor that the program is controlling, and therefore the loading direction of the specimen. The motor can be controlled using either position mode for controlling the position the motor, with the resolution of the picomotor that is less than 30nm, or velocity mode for choosing the loading rate for the test. But the control system is open-loop configuration. There is no feedback of velocity and position from the motor to pass into the control program.

In order to set up the testing system for both uniaxial tensile testing and biaxial tensile testing, the LabView program should satisfy the following functions:

- Move each motor individually to optimum position for testing
- Control the motor position and speed for loading
- Control the two motors for each set of uniaxial loading simultaneously
- Be able to control each set of uniaxial loading motors consecutively
- Be able to control two sets of uniaxail loading systems simultaneously

The structure of the control program is shown in *Figure 3.7.*

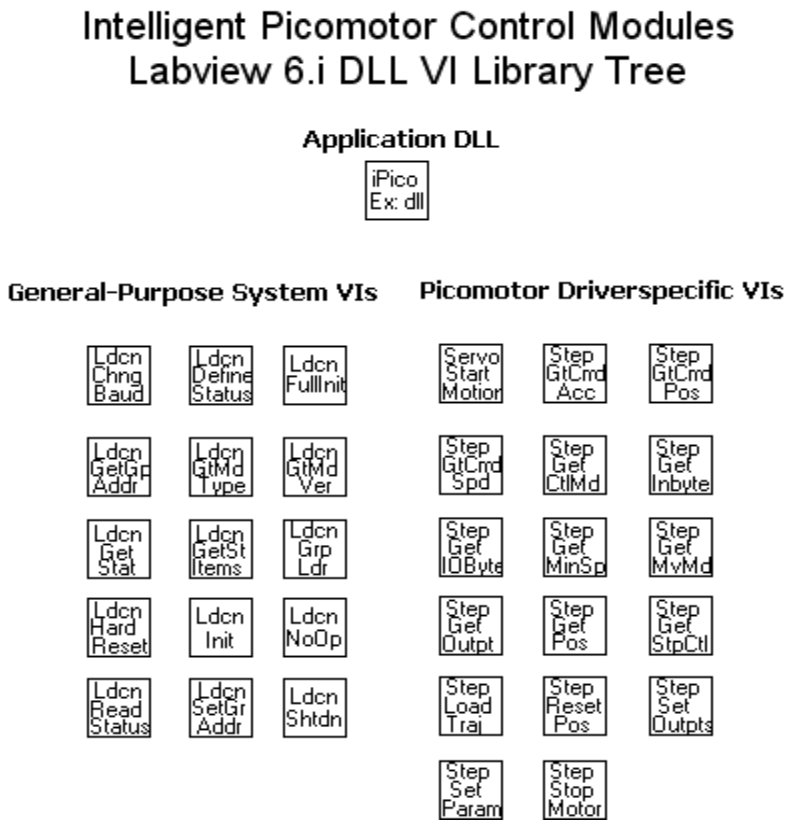

Figure 3.5: SubVIs library tree used in the control program of the picomotor

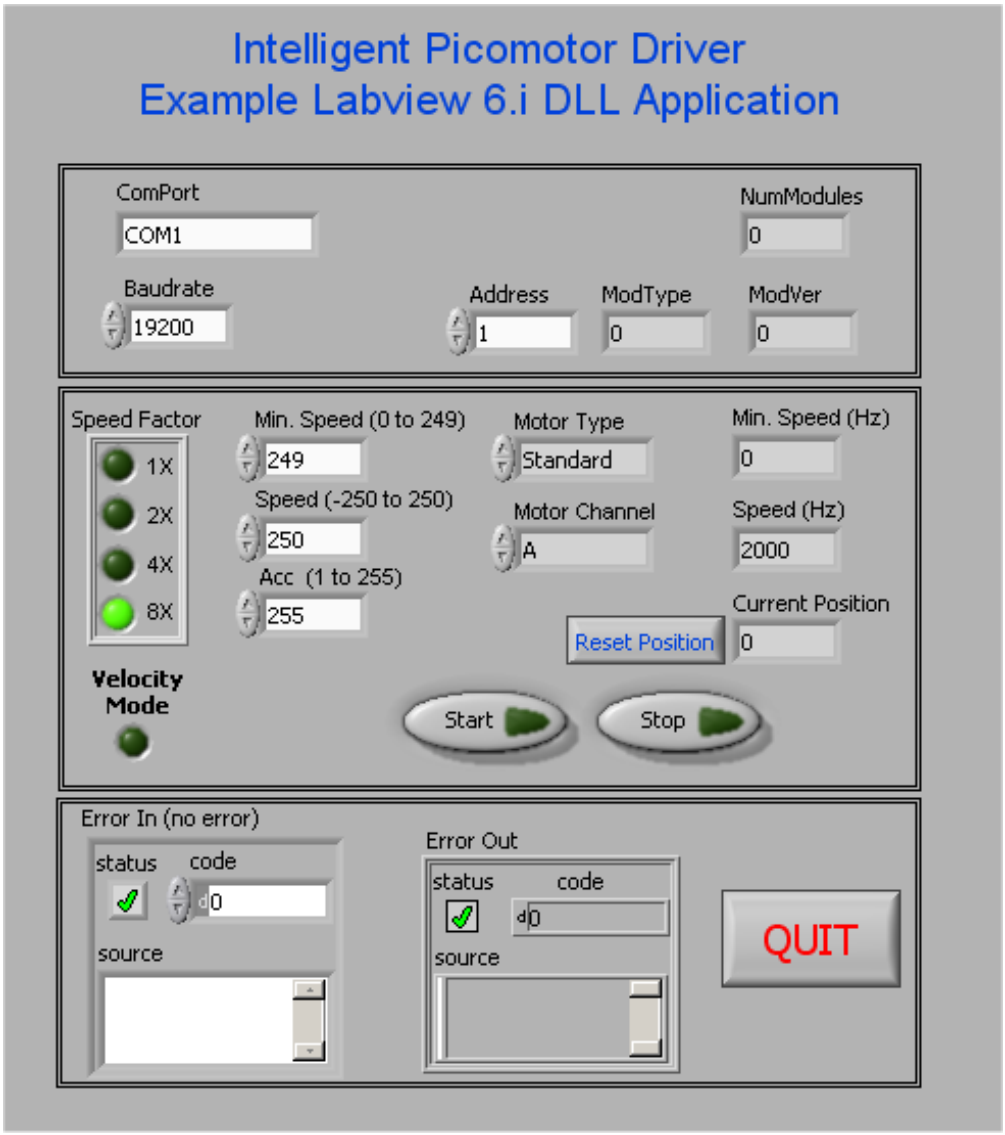

Figure 3.6: Example graphic user interface of the control program of the picomotor

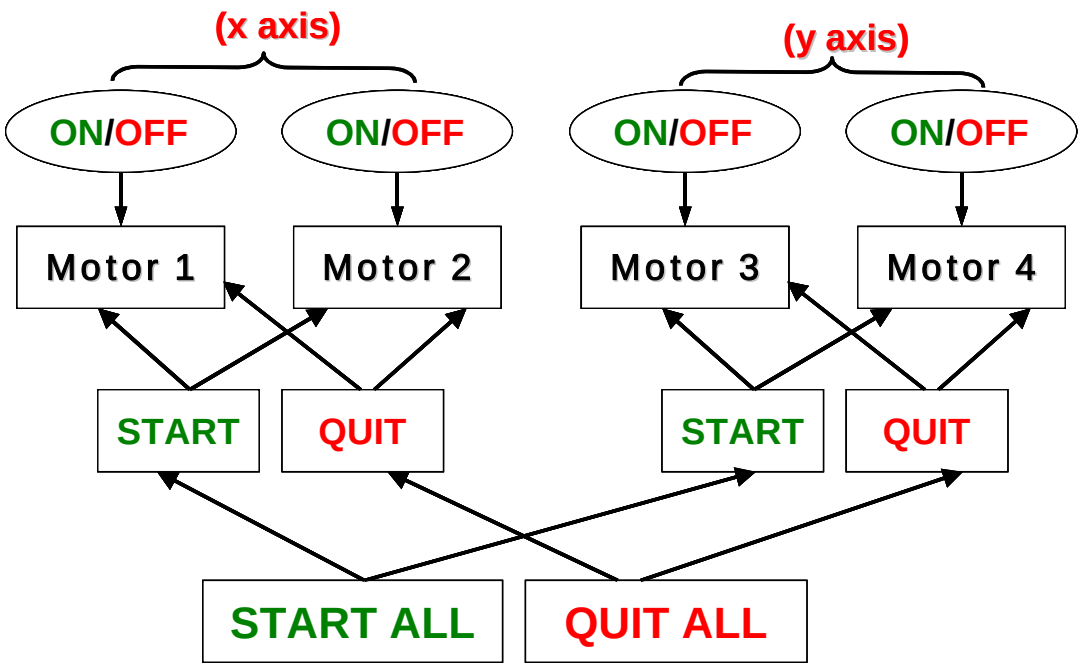

Figure 3.7: The structure of the control program for uniaxial and biaxial testing

3.2.2 Control of the Data Acquisition System

As discussed in the previous section, the load is measured using the load cell during the test. The load cell is first connected to the voltage bridge amplifier to convert to voltage signal and amplify the voltage from the millivolt range to the desired voltage value. Then the voltage signal is connected to a data acquisition system which includes the NI multifunction data acquisition device NI PXI 6025E, the accessory I/O connector board and cable. The load can be recorded during the whole testing process. Through the PXI card, the computer can communicate with the load cell.

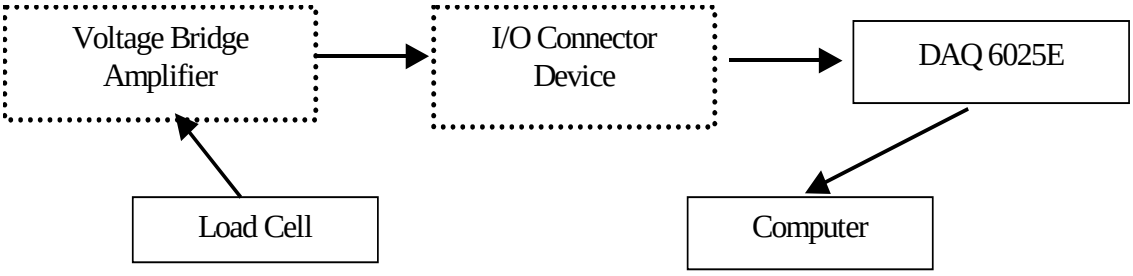

Figure 3.8: Diagram of data acquisition system

The PXI 6025E is capable of 8 channels of data collection simultaneously at up to 200 kS/s. The PXI 6025E is connected to the computer mainboard. It communicates with the voltage amplifier through the I/O connector and connection cable. The NI standard I/O connector for 6025E is shown in *Figure3. 9*. The load cell output is connected to the assigned channels in the I/O connector. The load cell outputs the different voltage values according to the tension or compression to the data acquisition board. The computer then acquires voltage data from the data acquisition board and records the data. The voltage data can then be converted to the force. Therefore, the LabView program for data acquisition has the following objectives:

- Set up and initialize DAQ device;
- Define channels for data acquisition;
- Define scan rate for data acquisition;
- Collect and convert voltage data into load;
- Real-time view of data;
- Save data to the desired directory;

The graphic interface of the data acquisition program is shown in *Figure 3.9*. The device number is the number assigned to the data acquisition board PXI 6025E. The channel numbers are defined as each pair of pins shown in *Figure 3.10*, depending which channels are used to connect the load cell. The scan rate defines the frequency of collecting data. The sample number defines the total data number to collect before the program stops. The path defines the directory to save the collected data. Also there is a *STOP* button to stop the data collection at any time when the program is running. The collected data is viewed in real-time base in the waveform chart.

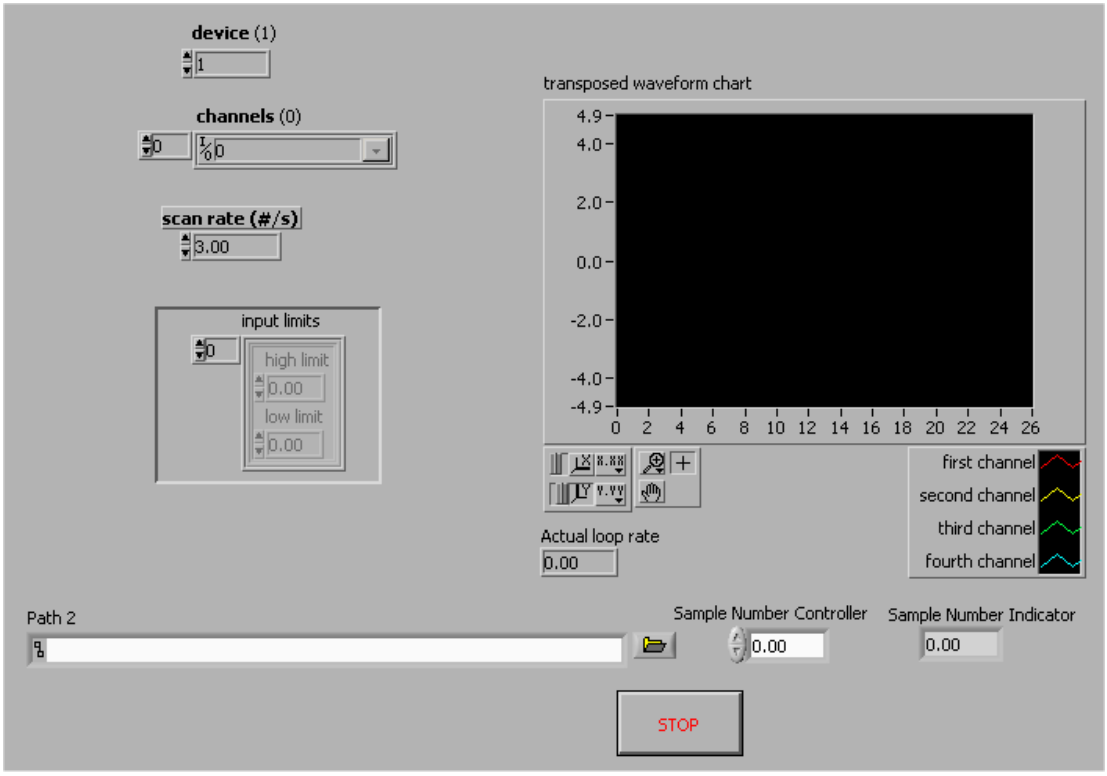

Figure 3.9: Graphic interface of the data acquisition program

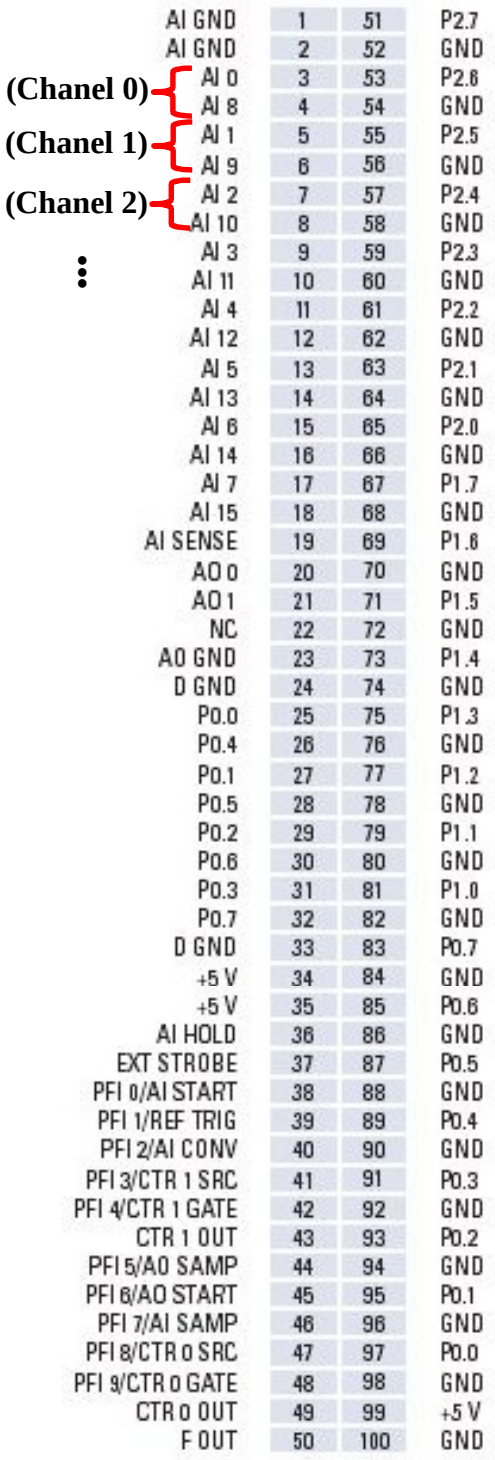

Figure 3.10: I/O connector device for PXI 6025E

3.3 Summary

In this chapter, the design and construction was introduced briefly and the control system of a novel biaxial microtensile testing system was discussed in detail. First, the conceptual design and the basic issues for the biaxial microtensile testing system were presented. Second, the selection of the components for the loading system and the data acquisition was discussed. The optical microscope has been integrated to acquire *in situ* digital images of deformed specimen surfaces at the microscale and an objective AFM was integrated to obtain images at the nanoscale . Then, the hardware configuration of the loading system and the data acquisition system, as well as the LabView programs to control the loading system and data acquisition were discussed.

4 Microtensile Testing at the Microscale and Nanoscale

4.1 Microtensile Testing of Vinyl Specimen at the Microscale

This section is focused on an experiment that was conducted to demonstrate the capability of biaxial testing of the microtensile testing system at the microscale.

4.1.1 Preparation of the Biaxial Testing Specimen

The plate with a hole specimen has been used by Cardenas-Garcia *et al* to demonstrate the application of the "microscopic hole method" as an alternative approach to assess the mechanical properties of freestanding thin films [Cho and Cardenas-Garcia, 2004]. In this thesis, the plate with a hole specimen was used to demonstrate the capability of the biaxial loading of this tensile testing system at the microscale.

Oracal® premium cast non-perf white color vinyl was used as the testing material in this investigation. It is feasible to generate speckle patterns on the surface of the vinyl specimen that is suitable for DIC. The thickness of the material is 2mil. The specimen was cut into the desired dimensions using razor plotter with a resolution of 25 microns. The dimension of the biaxial testing specimen is shown in the following *Figure 4.1*. The width is 4 mm and the length of each axis is 20mm. The center of the hole is located at the center of the specimen. The diameter of the hole is 0.8mm. The vinyl specimen was then painted with black speckles to generate a pattern suitable for DIC.

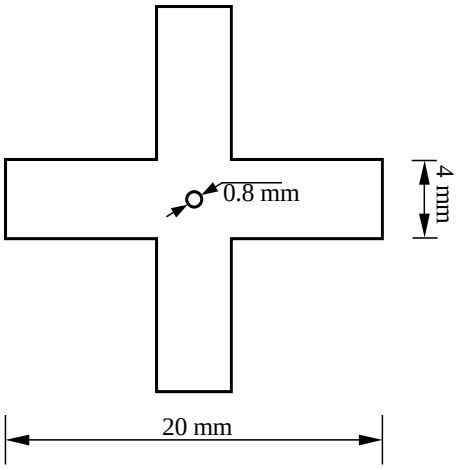

Figure 4.1: Dimensions of the biaxial testing specimen

4.1.2 Conduction of Biaxial Testing at the Microscale

For biaxial testing, digital images were obtained using a Q-Imaging Retiga 1300 CCD camera with 8 bit gray level resolution and a 1280x1024 pixel resolution. The configuration of the testing system with CCD camera and objective piece is shown in *Figure4. 2*. The Q-imaging CCD camera was mounted to the eyepiece holder of the microscope and a 3x objective piece was mounted to the microscope objective holder in order to observe a few millimeter square area around the hole in the vinyl specimen.

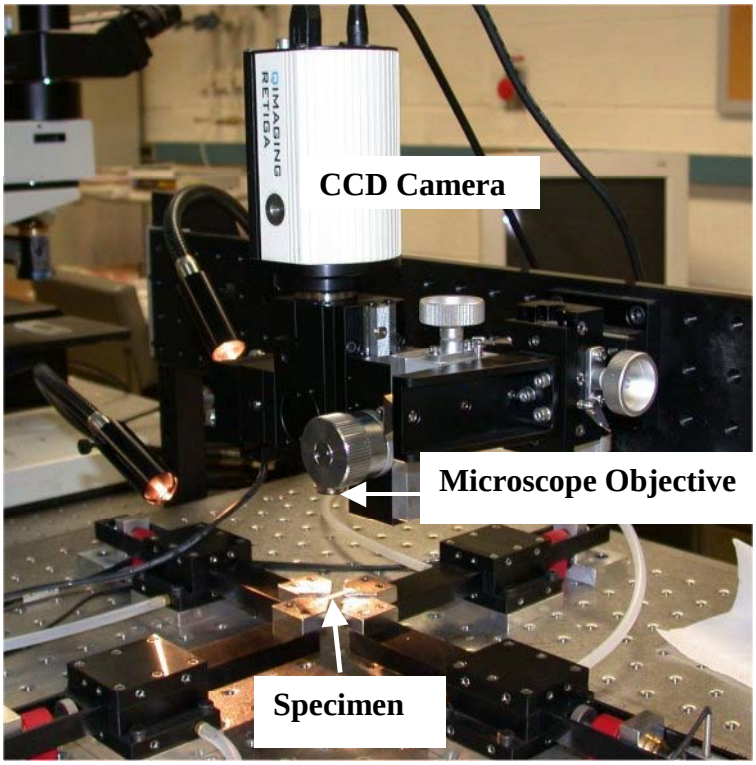

Figure 4.2: Configuration of the testing system with CCD camera and microscope objective piece

The spatial resolution of each pixel in the digital image for this configuration was calculated using the moiré grating with 10 pairs of line per mm. The digital images obtained from the gratings were shown in *Figure 4.3*. There are 46.3 pairs of lines shown along the axis with 1280 pixels and 37 pairs of lines along the axis with 1024 pixels. Therefore, the size of the imaging area over the specimen is 4.6mm by 3.7mm corresponding to a spatial resolution of 3.6 micron per pixel in the digital image.

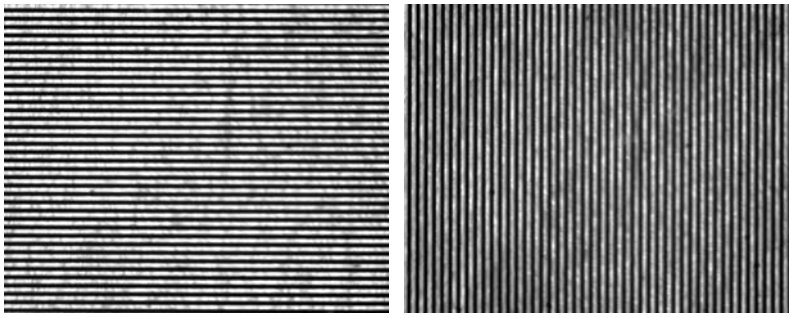

Figure.4.3: Digital images of the moiré gratings

After the specimen was painted to have the speckle pattern, it was removed from the base material and mounted to the grip of the microtensile tester using epoxy glue. Gauge length of the specimen is 10mm. Straight lines were drawn between the two opposite grips along one axis as the reference to place the specimen so that the center of the hole is positioned at the center of the view window. An image of the specimen with speckle patterns obtained using the CCD camera is shown in *Figure 4.4*. The pixel locations of the four points A, B, C and D were used to calculate the pixel location of the center of the hole. The position of the hole can be further adjusted using the independent motion of each motor till it is precisely located at the center of the view window. Then equal load is applied to the specimen by the opposing motion of the motors #1 and #2 along one axis and #3 and #4 along the other axis. The digital images are obtained from the specimen after each increment of load. DIC is then applied to the digital images to calculate the displacement and strain field around the hole. The displacement fields and strain fields are shown in *Figure 4.5(a)-(e*). From these results, it can be seen that the strain field is reasonably symmetric around the hole, which is consistent with the biaxial loading ratio of 1:1 being applied to the ends of the specimen. The tensile testing system is therefore

capable of conducting biaxial tensile testing at the microscale provided the specimen is properly positioned. The displacement resolution was approximately 0.18 microns, indicating that the technique is capable of measuring displacements with sub-micron resolution.

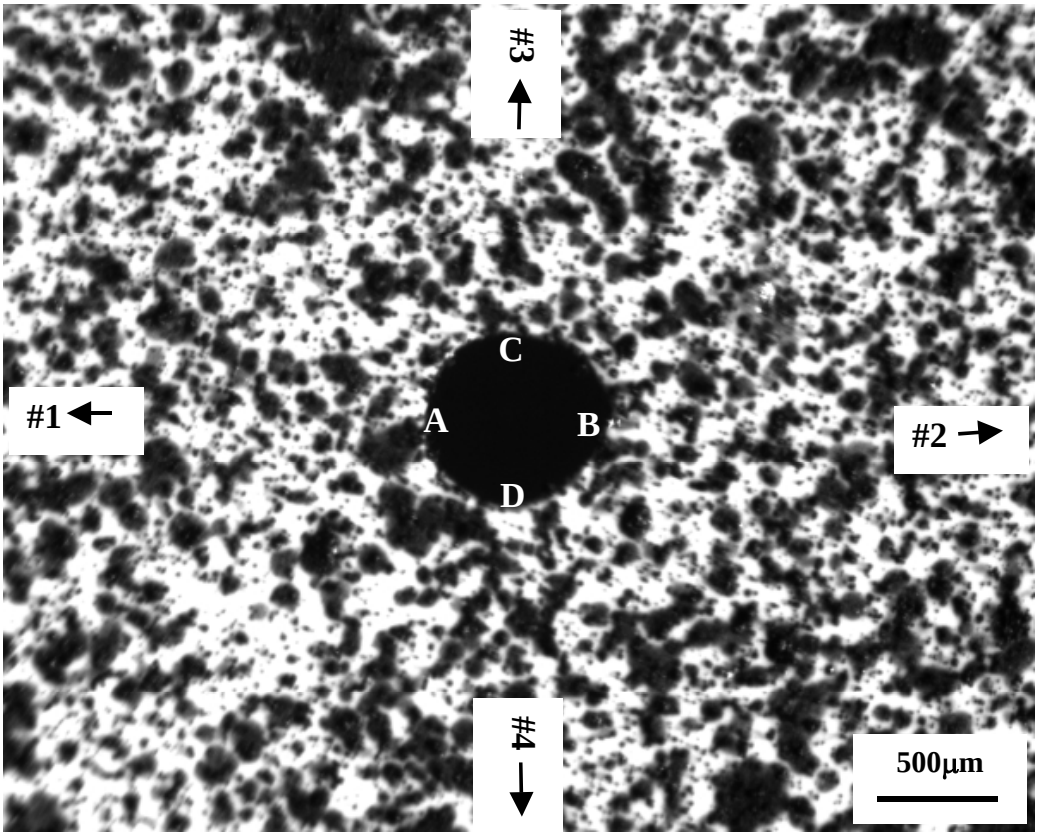

Figure 4.4: Digital image of specimen with speckle patterns

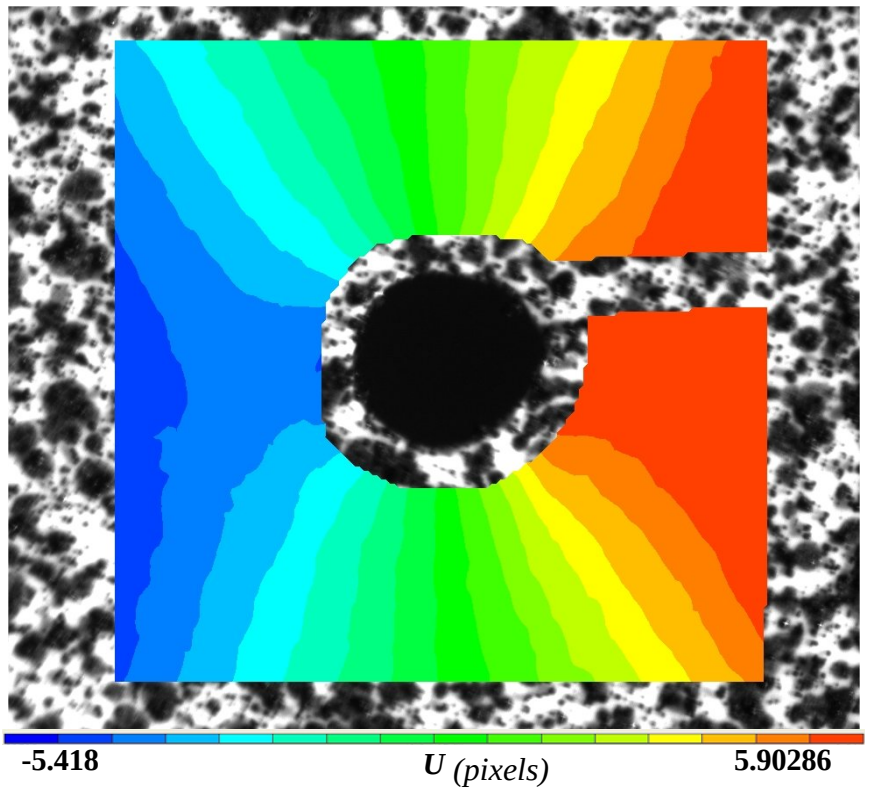

(a)

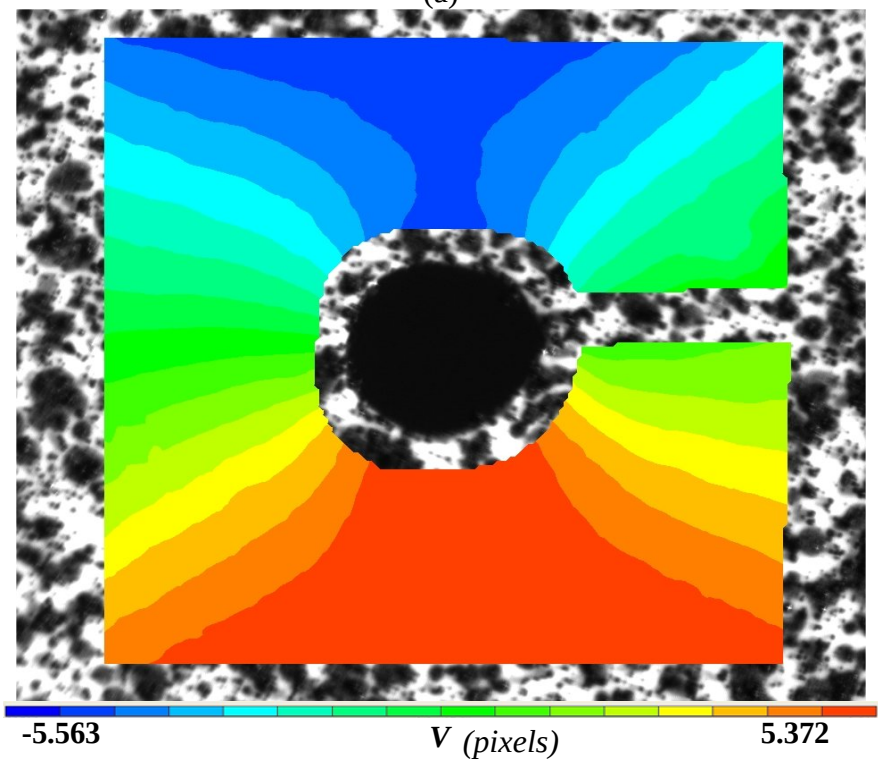

(b)

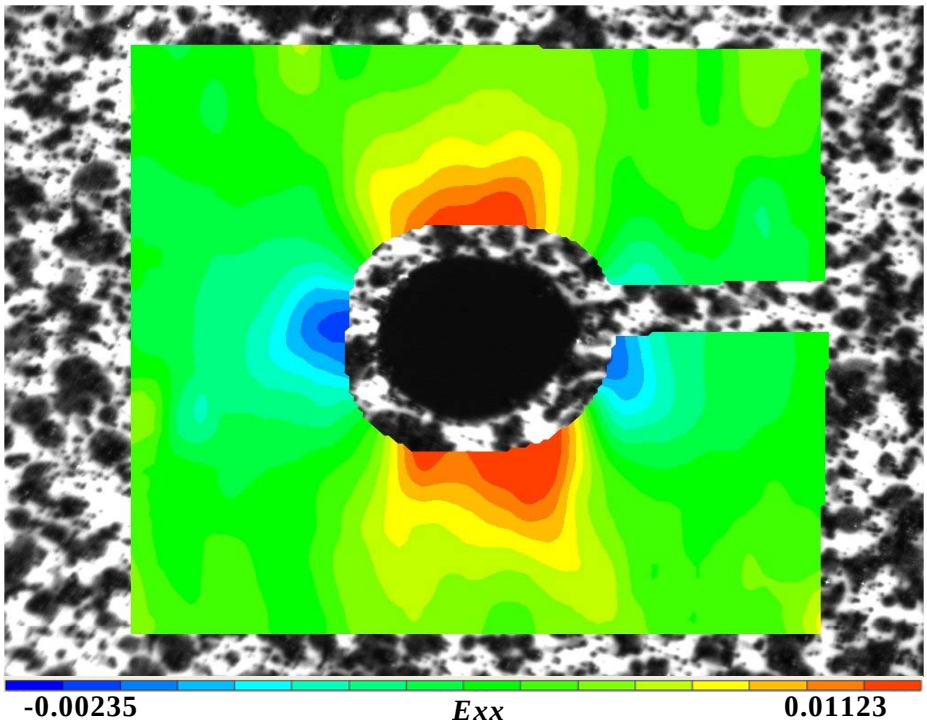

(c)

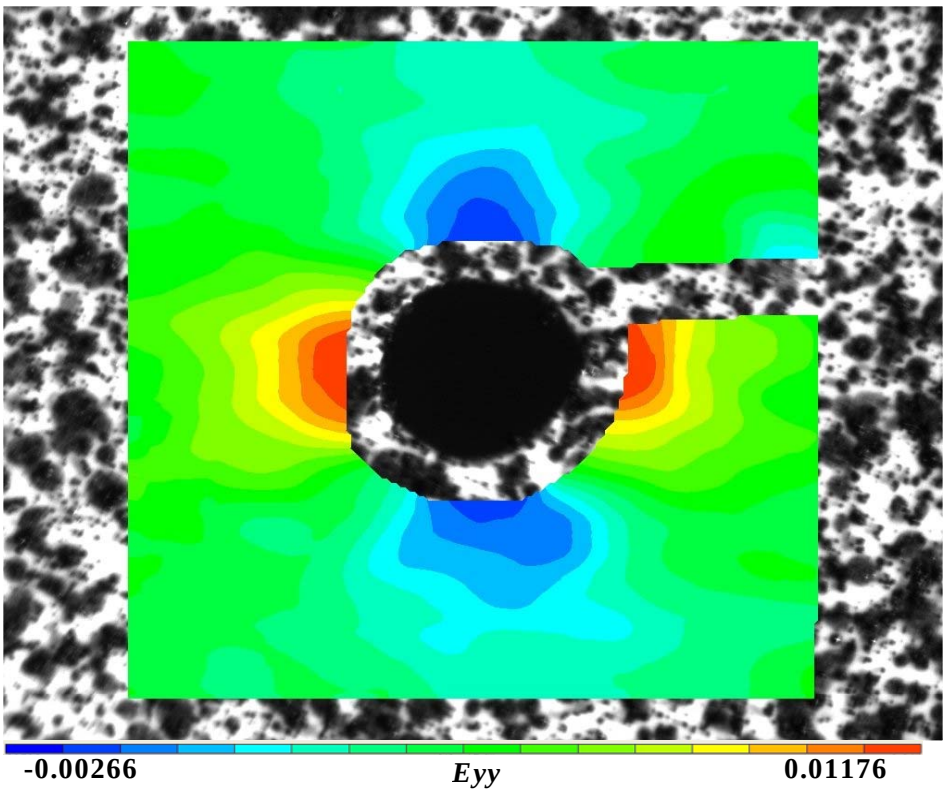

(d)

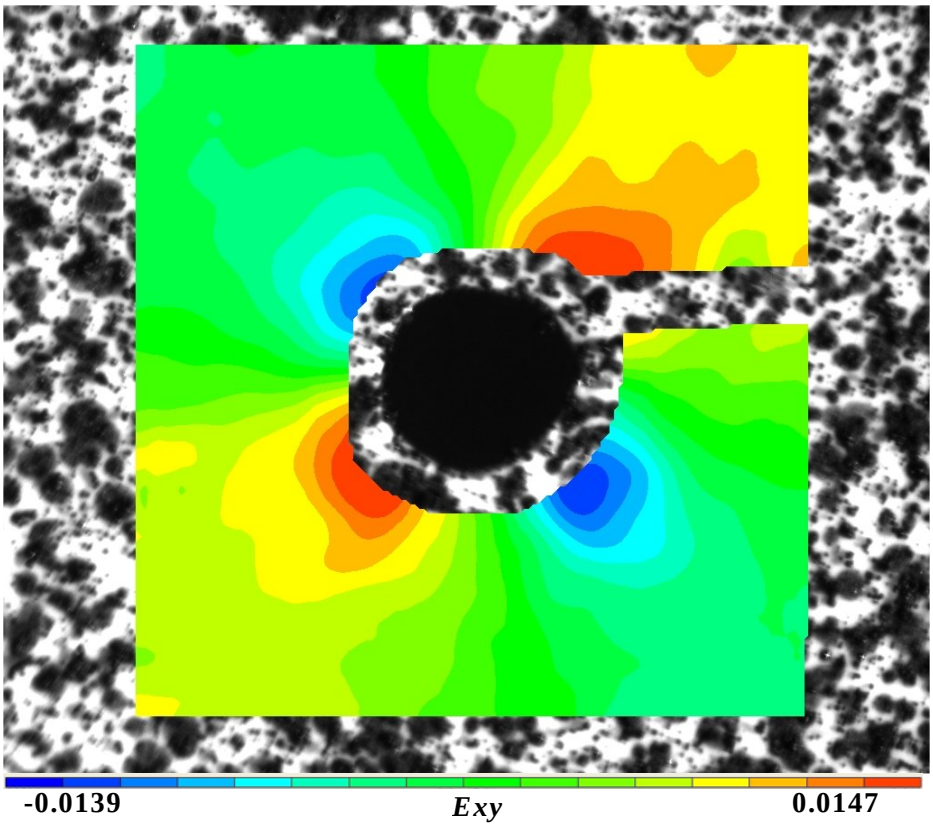

(e)

Figure 4.5: The displacement fields and strain fields from DIC, (a) U, (b) V, (c) Exx, (d) Eyy, (e) Exy

4.1.3 Finite Element Analysis (FEA) and Elasticity Analysis of a Plate with a Hole

A Finite Element Analysis (FEA) is conducted on the specimen shown in *Figure 4.1* to obtain the displacement and strain field around the hole when the specimen is under certain deformation. The geometry and meshing of the specimen is shown in Figure 4.6. Eight-node quadratic shell element was chosen for this analysis. A deformation of 0.03 mm was applied to two adjacent ends of the specimen. Material properties of a general vinyl were used, with a Young's modulus of 2.0 GPa

and Poisson's ratio of 0.4. The *U* and *V* displacement fields around the hole are shown in *Figure 4.7(a) and (b).* The strain fields Exx, Eyy and Exy are shown in *Figure 4.8(a)-(c).* Comparing the experimental data with the FEA results, it is clearly shown that the displacement fields and the strain fields around the hole exhibit the same symmetric distribution across the axes of symmetry.

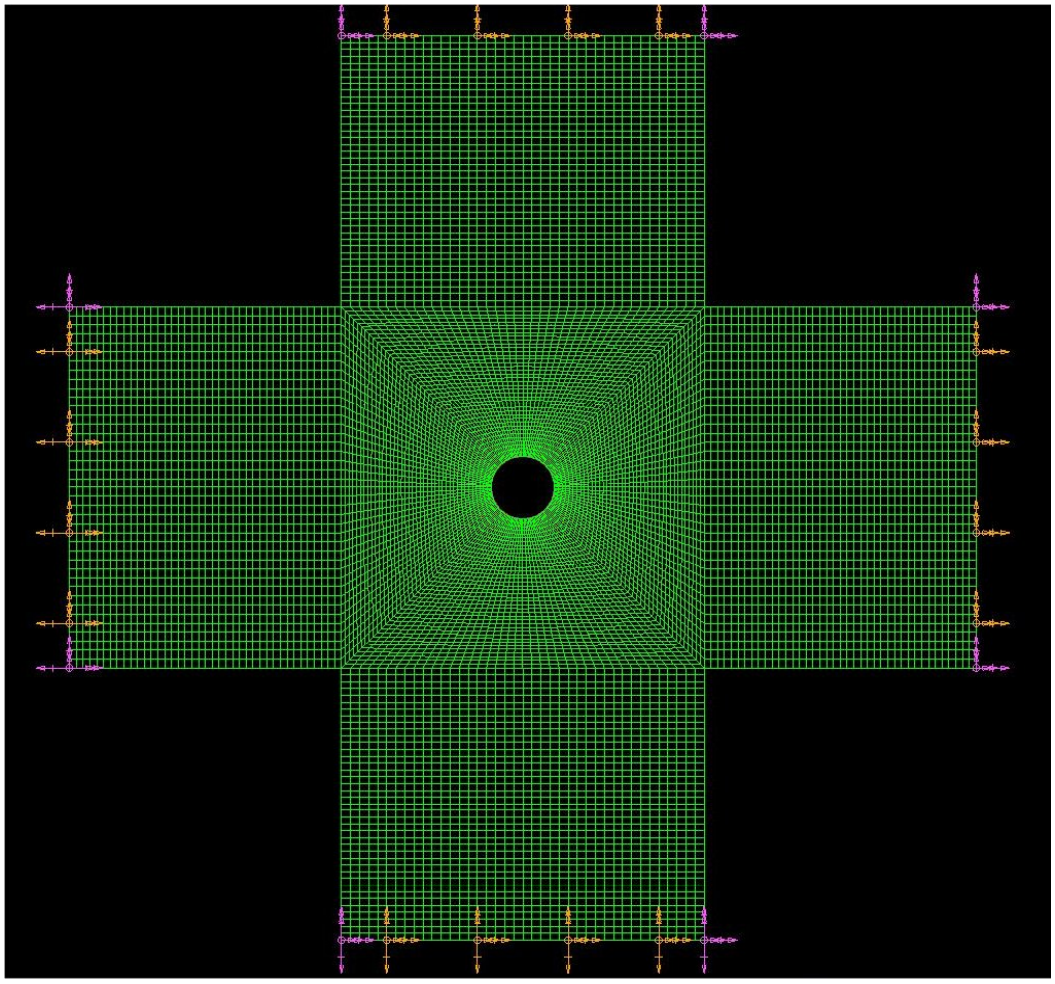

Figure 4.6: Mesh used for FEA of specimen

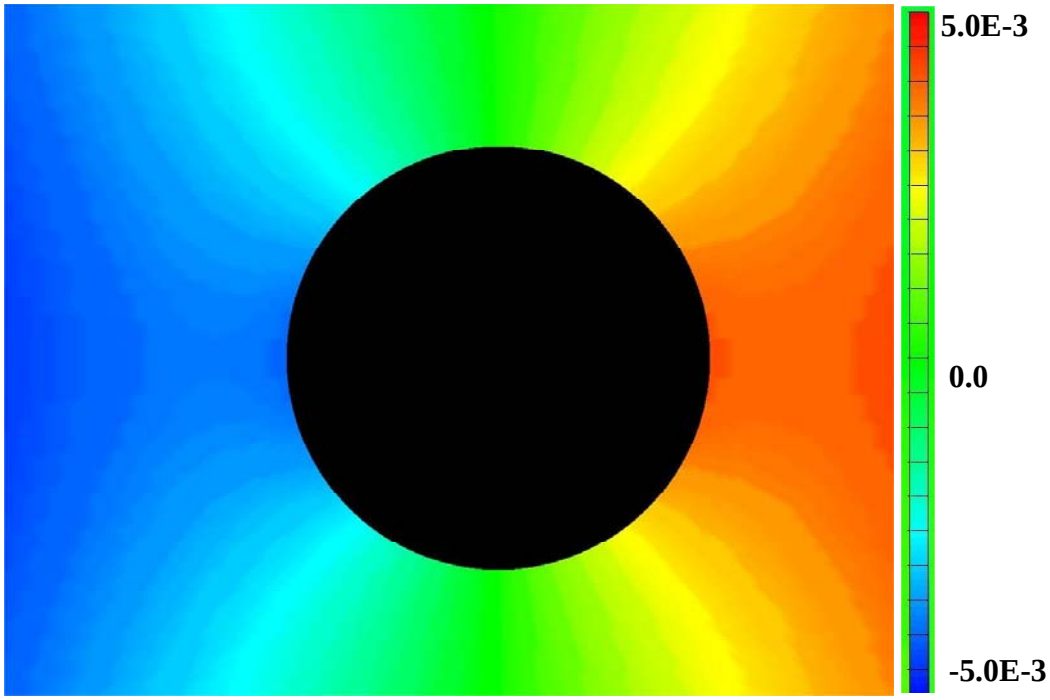

(a)

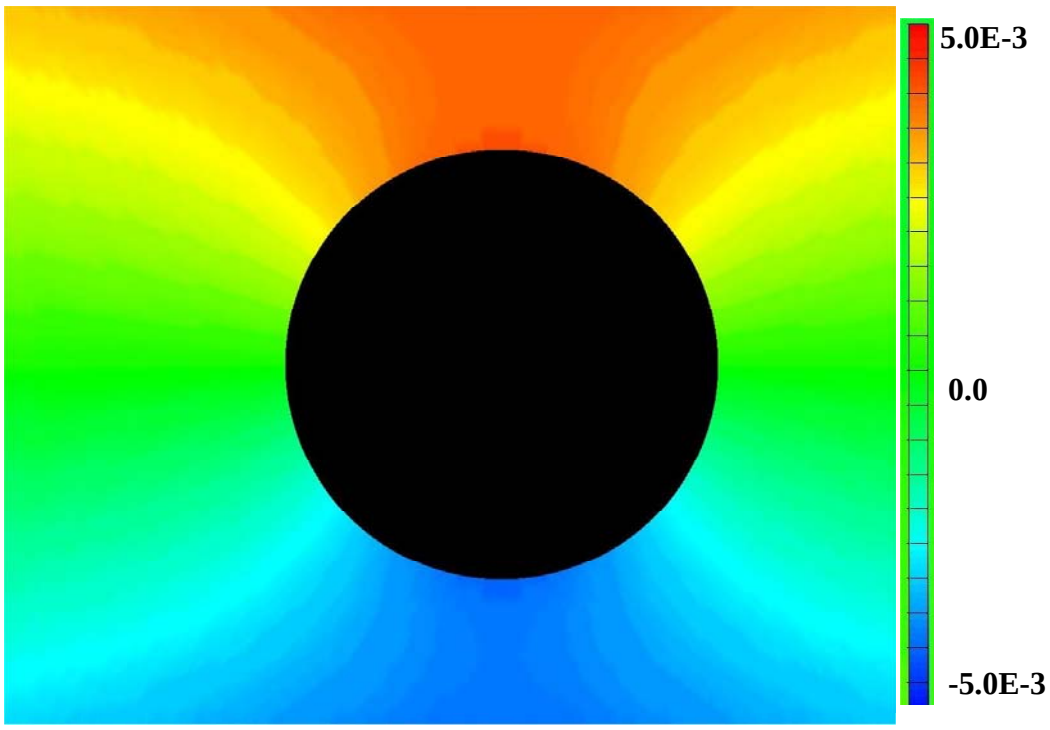

(b)

Figure 4.7: FEA predictions for: (a) U displacement field, and (b) V displacement field (in mm)

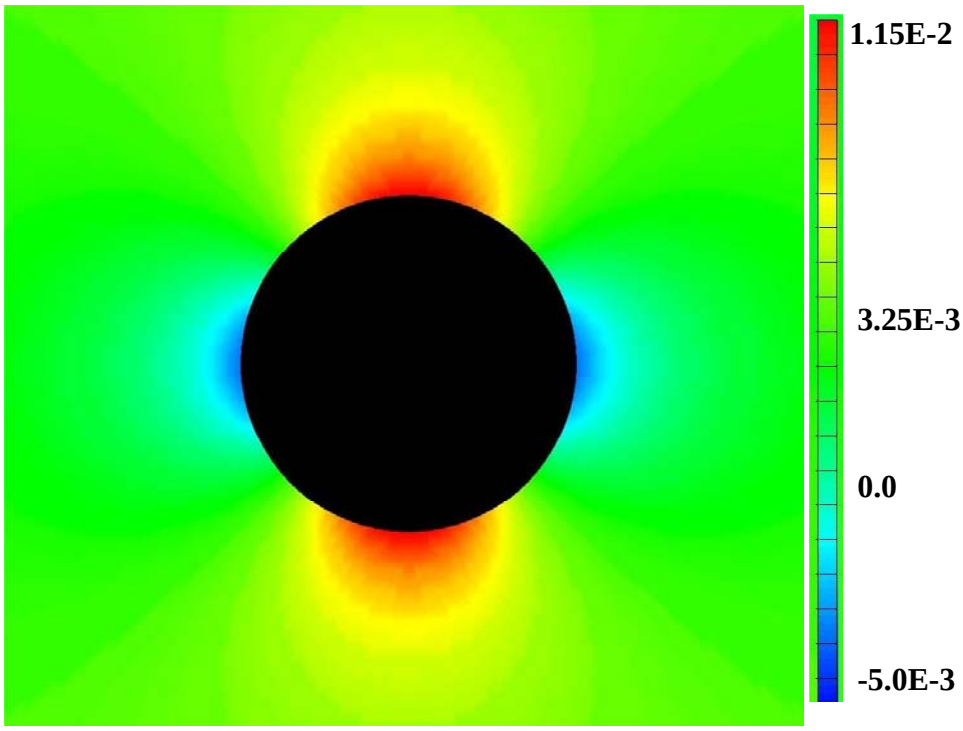

(a)

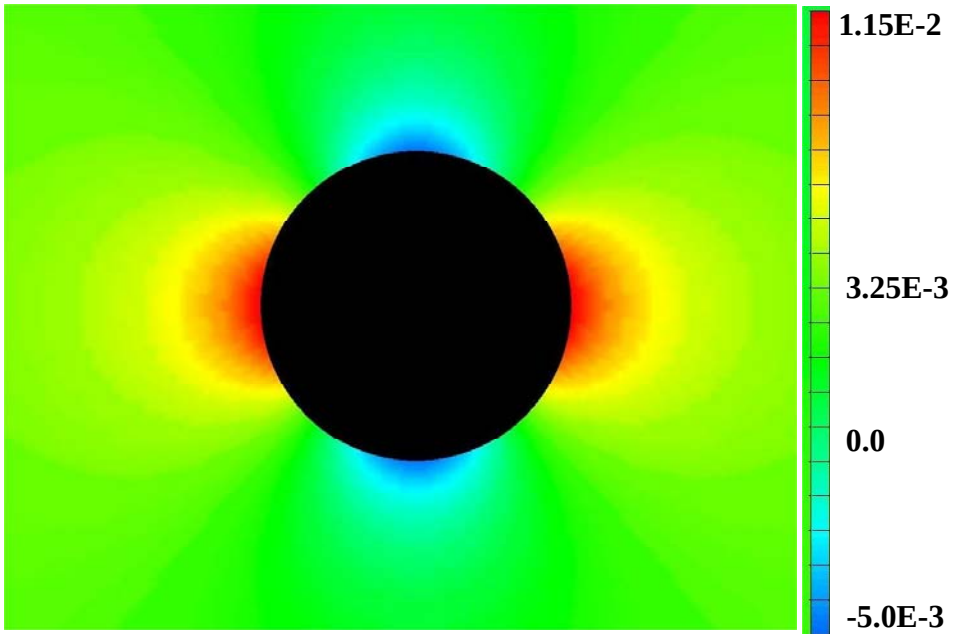

(b)

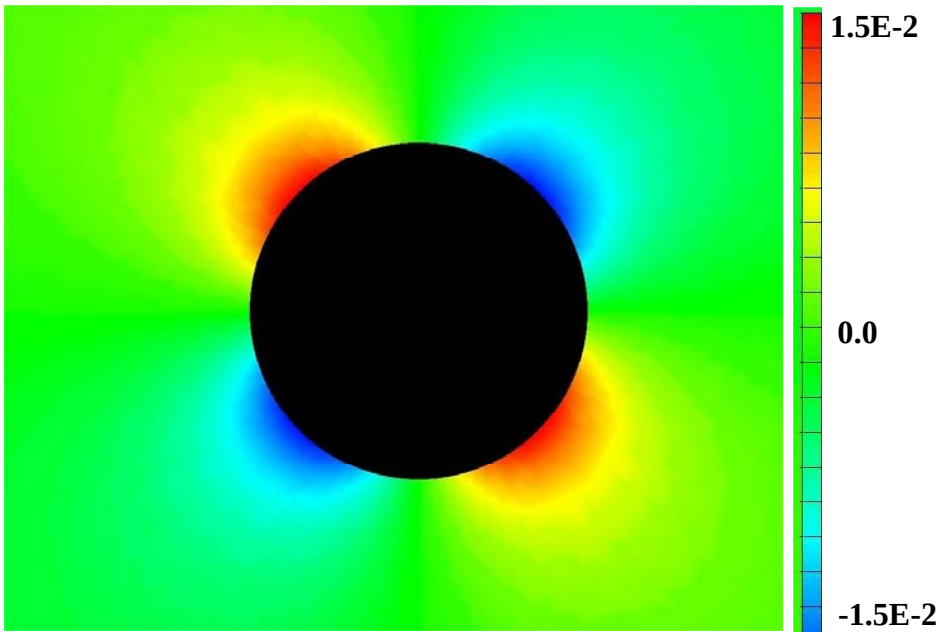

(c)

Figure 4.8: Strain fields predicted from FEA, (a) Exx, (b) Eyy, (c) Exy

The DIC strain results can be directly compared with a classical theoretical elasticity analysis for a hole in an infinite plate subjected to biaxial loading at various angular locations around the hole. The biaxial strain state for a loading ratio of 1:1 is as follows:

$$\varepsilon_{rr} = \frac{\sigma}{E}\left(1-\frac{a^2}{r^2}\right)-\frac{\nu\sigma}{E}\left(1+\frac{a^2}{r^2}\right)$$
$$\varepsilon_{\theta\theta} = \frac{\sigma}{E}\left(1+\frac{a^2}{r^2}\right)-\frac{\nu\sigma}{E}\left(1-\frac{a^2}{r^2}\right) \qquad (4.1)$$

Where ε_{rr} is the radial strain, $\varepsilon_{\vartheta\vartheta}$ the tangential strain, σ is the far-field stress, E is the Young's modulus, ν is Poisson's ratio, a is the diameter of the hole, and r is the radial position. The DIC and theoretical results can be seen in *Figure 4.9* for radial strain,

Err, angular strain, E_{JJ}, and shear strain, *Exy*. From these comparisons, it is evident that the DIC results are very close to those expected from the analytical solution. However, there is a much different trend for the Exy data that is most likely due to the effects of the finite geometry that are approached at the 45^{o} angles. These effects are easily quantified from the FEA results, shown in *Figure 4.10*. Clearly, at radial distances of greater than 300 pixels (~1.08 mm) from the center of the hole, the presence of the specimen boundary slightly increases the shear strain. However, within 300 pixels the FEA results were identical to the theoretical predictions for all 3 components of strain.

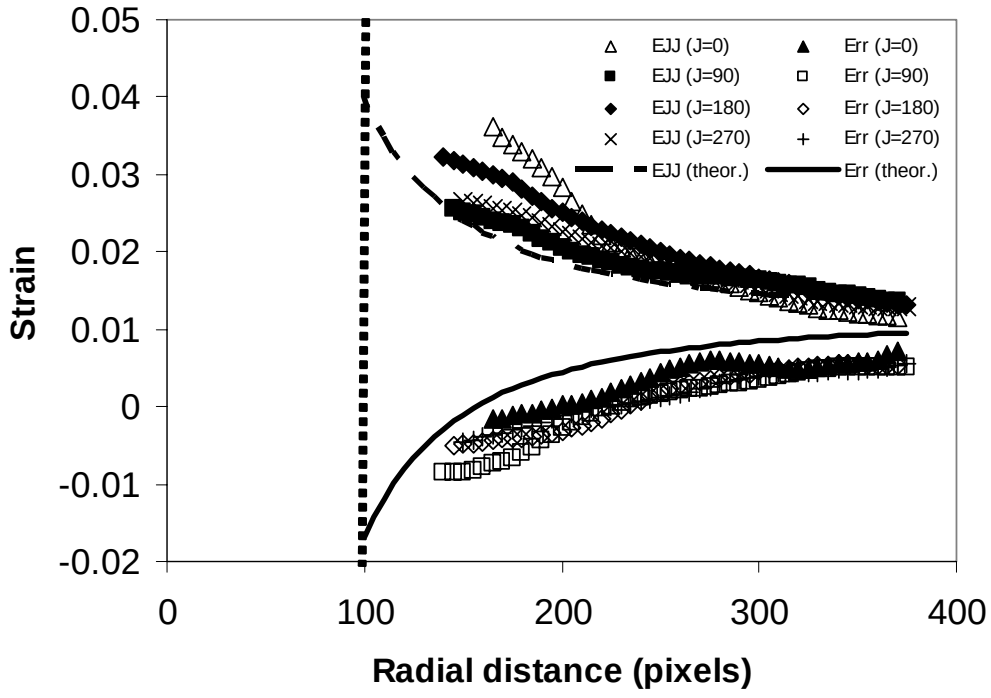

(a)

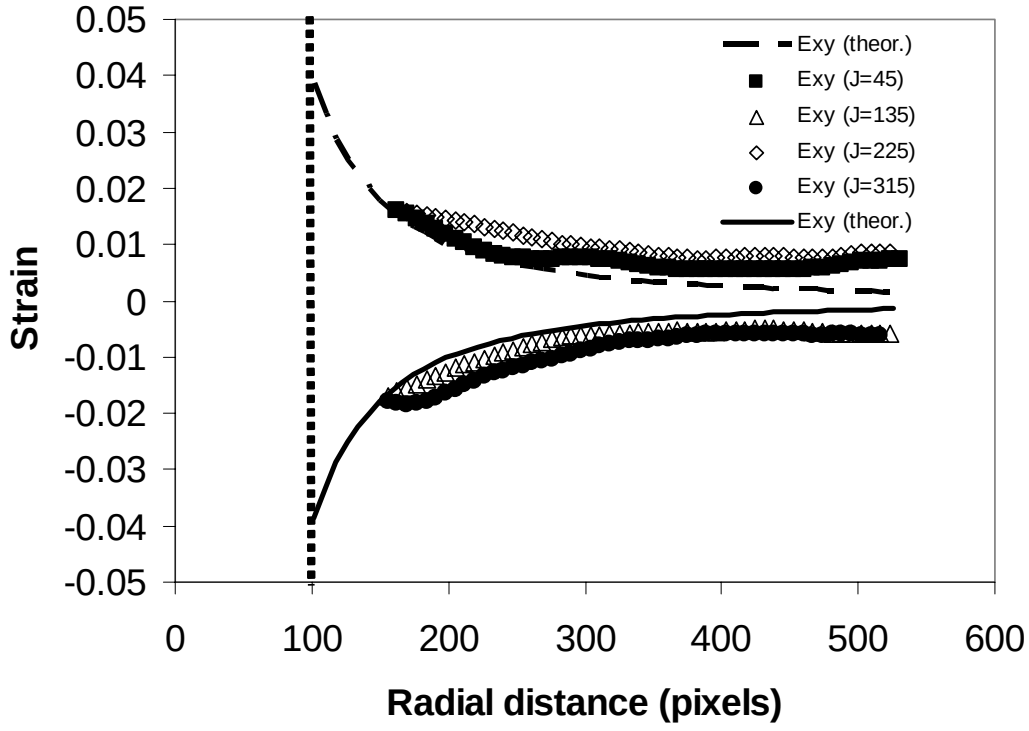

(b)

Figure 4.9: Comparison of DIC and theoretical solutions at various locations around the hole in the film for strains (a) Err and E_{JJ}, and (b) Exy.

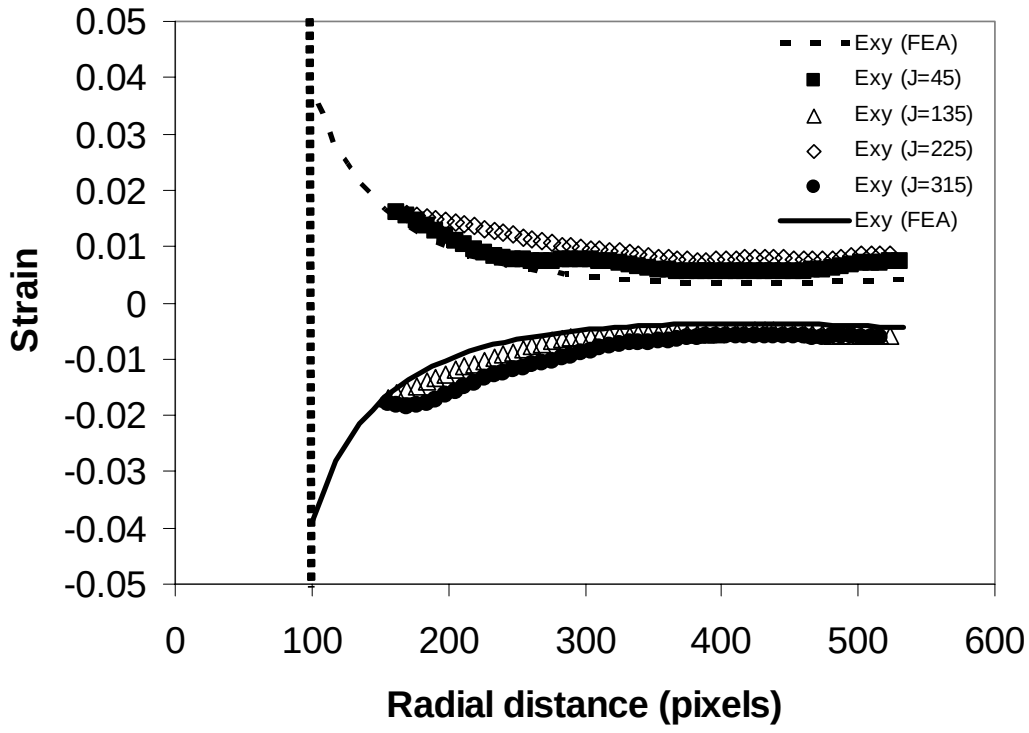

Figure 4.10: Comparison of DIC and FEA results at various locations around the hole in the film for strain Exy indicating effect of finite geometry on accuracy of DIC measurements.

4.2 Microtensile Testing of Sputtered Nanocrystalline Copper Film at the Nanoscale

The focus of this section is an experiment to demonstrate the capability of uniaxial tensile testing of nanocrystalline thin films at the nanoscale for the biaxial microtensile testing system. Uniaxial testing was performed since facilities had not yet been developed for preparing appropriate biaxial tensile testing specimens from nanocrystalline thin films.

4.2.1 Fabrication of Sputtered Nanocrystalline Copper Specimen

The sputtering process is defined as the ejection of particles from a condensed-matter target due to the impingement of energetic projectile particles. It occurs as a result of a momentum-exchange collision cascade process initiated near the target surface [Thin film processes II, 1991]. In operation, the target is mounted opposite to the substrate in a vacuum chamber, which is evacuated to a base pressure ranging from 10^{-6} to 10^{-10} Torr. Then the evacuated chamber is backfilled with an inert gas such as Argon and Nitrogen to provide the ion bombardment. Negative potential is applied to the target, while the substrate is grounded. The magnetron sputtering incorporates a crosswise magnetic field over the cathode, which traps the electrons in orbits near that location and thus greatly increases their path length before they finally escape to the anode by scattering.

For this research, an AJA international ATC 1200 DC magnetron sputtering system is used to sputter deposit copper thin films. A copper target of 99.99% purity with diameter of 2", thickness of 0.25" is chosen for deposition. The target is pressed tightly onto the cathode block by a clamping ring. Thin spacing rings are used to adjust the gap between the target and the clamping ring. The space between the top of the clamping ring and the ground shield is 1-2 mm to avoid an electrical short. A glass slide is used as the substrate for the sputtering since it has poor cohesion with the copper film and will make it easier to remove the specimen. The glass slide needs to be cleaned and handled with care in order to have fine and uniform copper film. The glass is first cleaned with acetone, methanal and isopropanol, then rinsed using DI water and dried using nitrogen, following the standard procedure for cleaning

silicon wafers in MEMS fabrication. After installation of the target and substrate, the chamber is cleaned and is first evacuated to pressure of 10^{-3} Torr using a mechanical roughing pump. It is then further evacuated to the base pressure of $2.0x10^{-7}$ Torr using a turbo pump. After evacuation, argon gas is used to refill the evacuated chamber until the pressure reaches $3.0E\times10^{-3}$ Torr for sputtering. The deposition power is 300W, while the distance between target and substrate is 2 inches. The film thickness is measured by a profilometer. The sputtering rate is about 0.4 μm/min. Films with a certain thickness can be fabricated using different sputtering times.

4.2.2 Conduction of Microtensile Testing at the Nanoscale

After fabrication of the copper film, a specimen with desired dimensions for uniaxial testing is cut out with special care to avoid breaking and folding the film. The film-substrate interface has a low adhesive strength, thus, the film can be easily peeled off the glass substrate and then mounted to the grips of the microtensile tester. The specimen is affixed to the grips using super glue. An optical microscope with a CCD camera that is mounted along the optical axis of the microscope is then used to observe the copper specimen during mounting so that the specimen can be mounted flat and aligned with the loading axis of the microtensile tester. The objective AFM is mounted to the objective piece holder of the microscope, which has been attached to the 3-D stage. AFM can then be positioned over the AOI of the specimen.

As discussed in section 3.1.2, the load in the specimen is introduced by the motion of the picomotor. Picomotor actuators have better than 30-nm resolution with minimal backlash and exceptional long-term stability and the ability to hold their positions without continuous application of power. This feature makes the picomotor

actuators suitable for the microtensile testing system. The picomotor is set up at the end of a linear air bearing stage. When the motors are pulling the linear air bearing stage from the end, they will induce a load on the specimen through the translation of the linear air bearing. The load in the specimen is increased as the picomotor continues to pull the specimen from the end. After each incremental step of load, an AFM image is acquired from the specimen. Normally, 1 Hz scanning rate is used in the AFM imaging. It takes about 4 minutes to acquire an image with a resolution of 256 by 256 pixels at this scanning rate. Therefore, the stability of the picomotor has to be sufficient to keep the specimen stationary during the AFM imaging. The loading and unloading of the specimen is controlled by the direction of the picomotor motion. The loading rate is controlled by the speed of the picomotor, which is a parameter designed in the LabView program for controlling the picomotor.

As mentioned previously, the AFM operates by measuring the interaction forces between the tip and sample. As the AFM tip moves over the sample, the distance between the tip and sample is controlled by the interaction force. The height of the tip is monitored through sensing the deflection of the cantilever beam. Therefore, the topographic information of each pixel in the whole scanning area is recorded for the specimen. The scanned topographic information from the AFM is presented in the form of a digital image. The crystal structures and grain boundaries can be clearly seen in the AFM topographic image. A typical AFM topographic image of the sputtered nanocrystalline copper specimen is shown in *Figure 4.11*. The scanning area is 2 μm by 2 μm and the resolution is 256 by 256 pixels. This is approximately 1000 times smaller than the spatial resolution of the optical

microscope used in section 4.1.2. These microstructural features also serve as references to keep track of the AOI for AFM imaging.

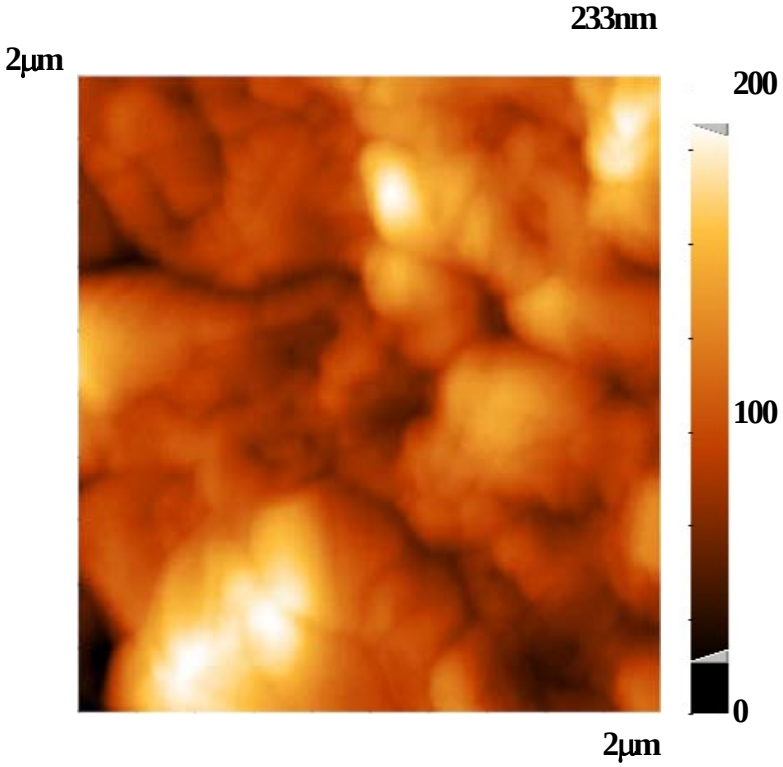

Figure 4.11: A typical AFM topographic image of sputtered nanocrystalline copper film

4.2.3 Nanoscale Displacement Acquisition of Microtensile Testing

4.2.3.1 Conversion of AFM Images

As discussed in the previous section, AFM topographic images are obtained showing microstructural features of the specimen. The topographic information of each pixel in the scanning area is recorded. This absolute height value is then converted to a relative value between 0 and 255, assigning the minimum height as 0 and the maximum height as 255. The height between minimum and maximum is

converted to some value between 0 and 255. Thus, a gray scale image can be obtained from these relative height values, with black color for 0, white color for 255 and shades of gray for values between 0 and 255. The intensity of each pixel in the gray scale image is corresponding to the topographic information of each individual point in the AOI. A gray scale image according to the topographic image in *Figure 4.7* is shown in *Figure 4.12.* The randomness of the grain structures produces the variation of the gray color through the image. This microstructural variation in the topographic image serves the same purpose as the painted speckle patterns in normal speckle DIC. The DIC technique based on the microstructural texture of the specimen is called "textured DIC", which is used to obtain the deformation at a scale comparable to the microstructure of the specimen.

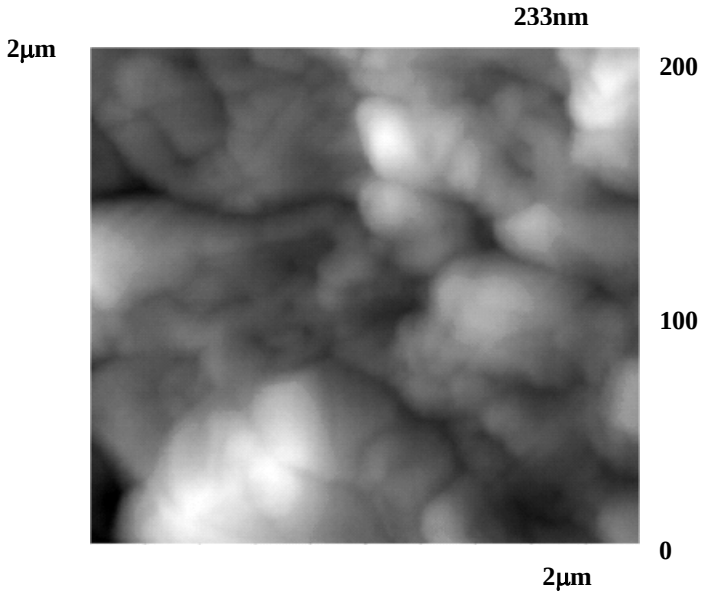

Figure 4.12: A gray scale topographic image of sputtered nanocrystalline copper film

4.2.3.2 DIC on Converted AFM Topographic Images

AFM topographic images are obtained during each incremental load step. These images are converted to gray scale images suitable for DIC. A test is conducted on a sputtered nanocrystalline copper specimen with a thickness of 6 μm, width of 2 mm, length of 10 mm and gauge length of 5 mm. The specimen is loaded until it experiences plastic deformation and breaks at the end. The load versus the loading steps of the picomotor is recorded and plotted as in *Figure 4.13*. The loading of the picomotor is increased every 200 steps as marked by letters "o, a, b, c…" in the loading curve. For each incremental step of load, the picomotor is held stationary at the position. AFM topographic images are then obtained for each of the position "o, a, b, c…". In order to apply DIC on the topographic images, these images have to share some common area. Thus, the AFM has to be able to obtain images from the same AOI over the specimen. This was accomplished by adjusting AFM probe position using the different offset values of the cantilever probe. By using the different probe offset values, the AFM was able to obtain images from the same AOI during each incremental step of the load. Topographic images from step *e* and step *j* are shown in *Figure 4.14* as the example. Topographic image from step *e* was obtained without probe offset, while the topographic image from step *j* was obtained with probe offset of 0.5 micron in y direction. The gray scale images according to these two images are also shown in *Figure 4.15*. The DIC image analysis technique was then applied on these two gray scale images from step *e* and step *j*. A subset size of 25 pixels was chosen for the DIC analysis. The *U* displacement and *V* displacement from the correlation of these two images are shown in *Figure 4.16*.

These results can clearly show inhomogenities in the displacement fields that are associated with microstructural features such as grains. The displacement fields are obtained at a spatial resolution of 20 nm per pixel and a displacement resolution of approximately 0.5 nm, indicating that the technique is capable of measuring displacements with sub-nanometer resolution. However, how will the offset value of the AFM cantilever probe affect the AFM imaging, thus affect the displacement field calculated from the topographic images? This effect has to be characterized so that it can be removed from the real displacement value.

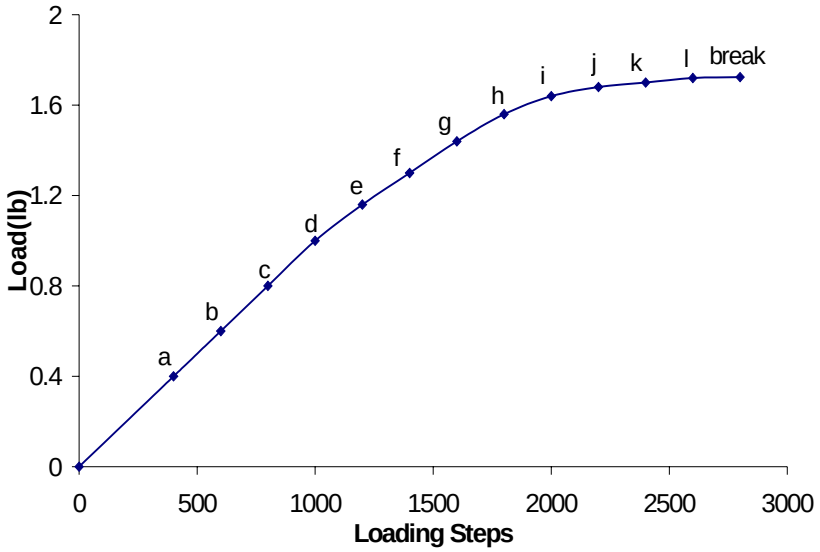

Figure 4.13: Load versus loading steps of picomotor

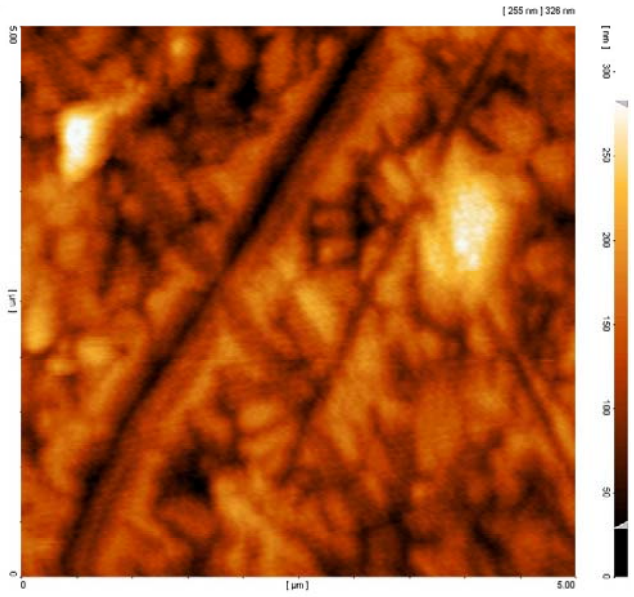

(a)

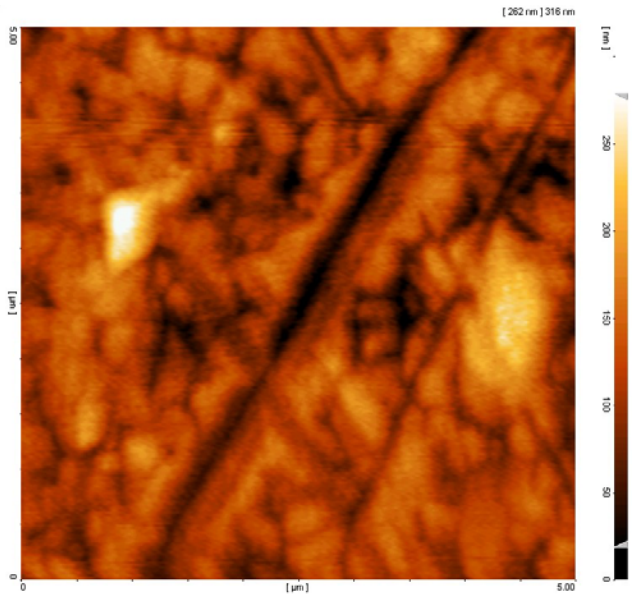

(b)

Figure 4.14: Topographic images from (a) step *e* and (b) step *j*

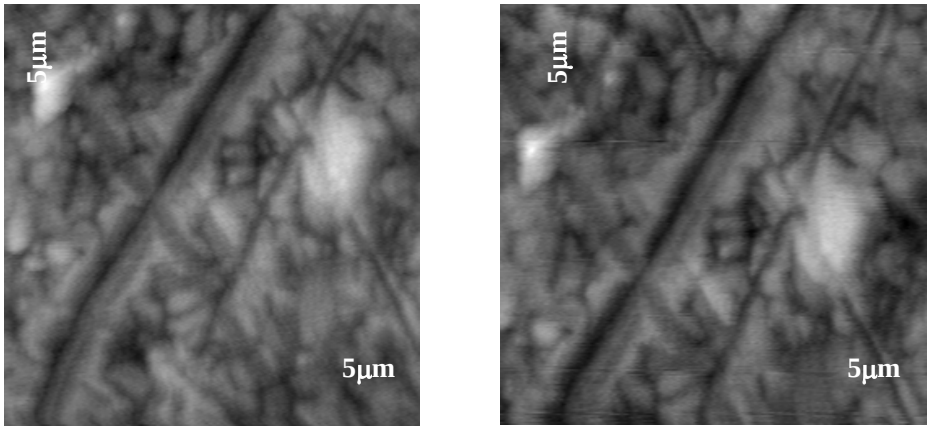

(a) (b)

Figure 4.15: Gray scale topographic images of (a) step *e* and (b) step *j*

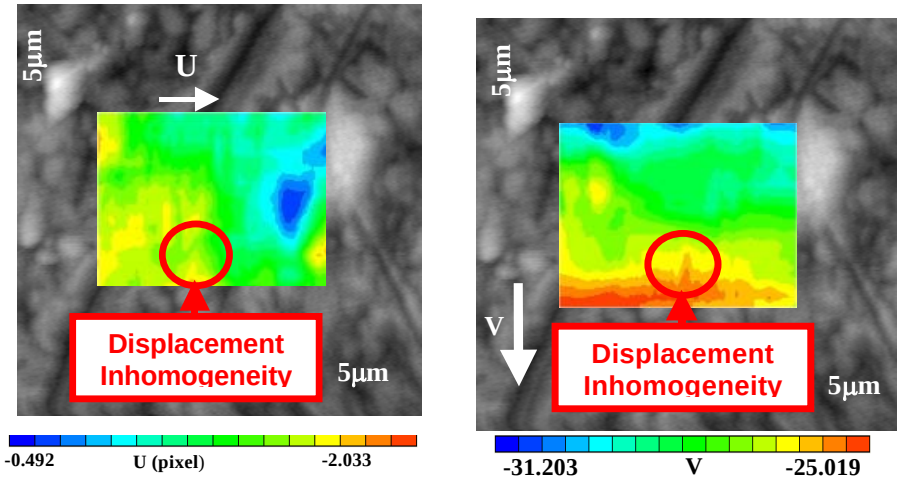

(a) (b)

Figure 4.16: Full-field *U* displacement and *V* displacement showing displacement inhomogeneity near a grain.

4.2.4 Challenges in Microtensile Testing

4.2.4.1 *Motion Control*: Minimizing Motion of Area of Interest

In order to apply the DIC technique to calculate the U and V displacement, the two images used for correlation analysis should share some common area. The AFM should scan on the same AOI during the whole process of loading, which means that the AOI on the specimen should keep stationary and unmoved during the whole loading process. In this research, this is accomplished by adjusting the different loading steps of the two picomotors at the end of loading axis. A CCD camera is connected to the eyepiece holder of the microscope as shown in previous *Figure 4.2*, but with AFM scanner head connected to the microscope objective holder. The AFM scanner is focused on some tracking features on the specimen as shown in *Figure 4.12*. These tracking features can be viewed with the CCD camera. The loading steps of each picomotor are adjusted so that the motion of these tracking features is not detectable within the resolution of the setup using CCD camera and 20x microscope objective, which is 0.5 micron spatial resolution per pixel. Using the adjusted ratio of the loading steps for picomotors during the whole process, the motion of AOI under AFM will be at the submicron scale. This small motion of the scanning area can be adjusted using the scanning probe offset value in the AFM measurement menu. Thus, the AFM can scan on the same area over the whole loading process. Topographic images of the same AOI can then be obtained to calculate the displacement field over the AOI.

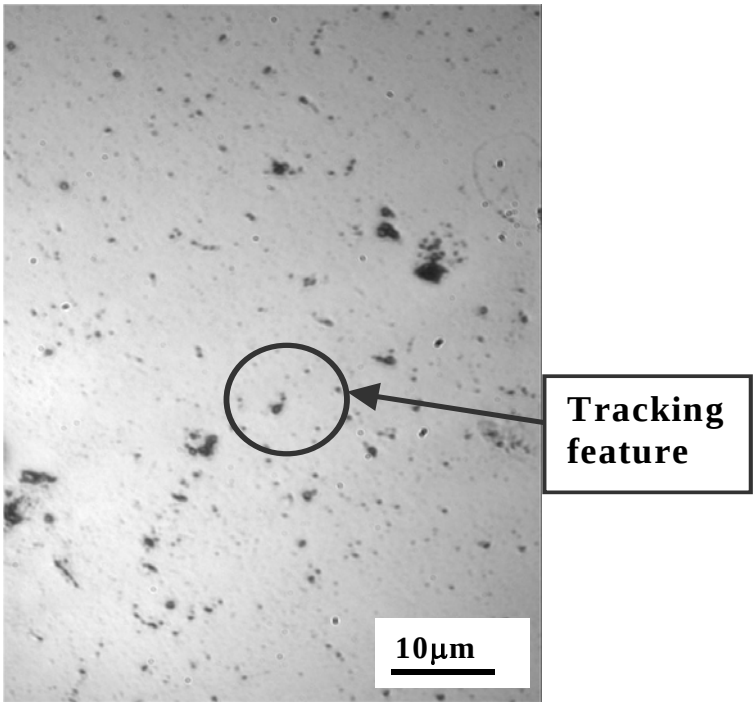

Figure 4.17: Surface tracking features used to adjust the motion of two picomotors

4.2.4.2 Noise Removal in Data Acquisition

As discussed in the previous section 3.1.2, the load was measured using the load cell during the test. The load was converted to voltage output and amplified by the voltage bridge amplifier. Then the voltage signal was output to a data acquisition system which included the NI multifunction data acquisition device NI PXI 6025E and the accessory I/O connector board and cable. In the original configuration, the amplifier and power supply are not shielded. Regular electrical wires were used to connect these components. The original setup is shown in *Figure 4.13*. Random noise was mixed together with the voltage signal during the acquisition of the load as shown in *Figure 4.14*. This noise showed up randomly and still existed after this testing system was set up on the vibration isolation table. It will also show up even

when the motor was not running and the load was constant. These characteristics of the noise indicate that the noise was possibly due to the effects of the ambient electrical noise. Thus, the amplifier and power supply were shielded in a box to reduce the noise to acceptable levels. A shielded connection card SCB-100 was used to replace the CB-100 card and a shielded cable was used to connect these components. The new configuration is shown in *Figure 4.15*.

Using this new configuration, the noise was eliminated from the voltage signal for the load, as shown in *Figure 4.16*.

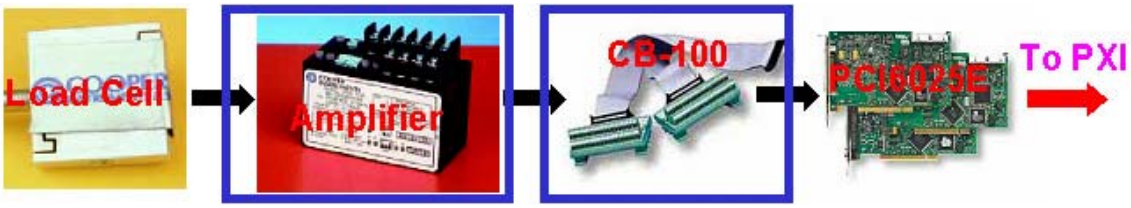

Figure 4.18: Configuration of the original data acquisition system

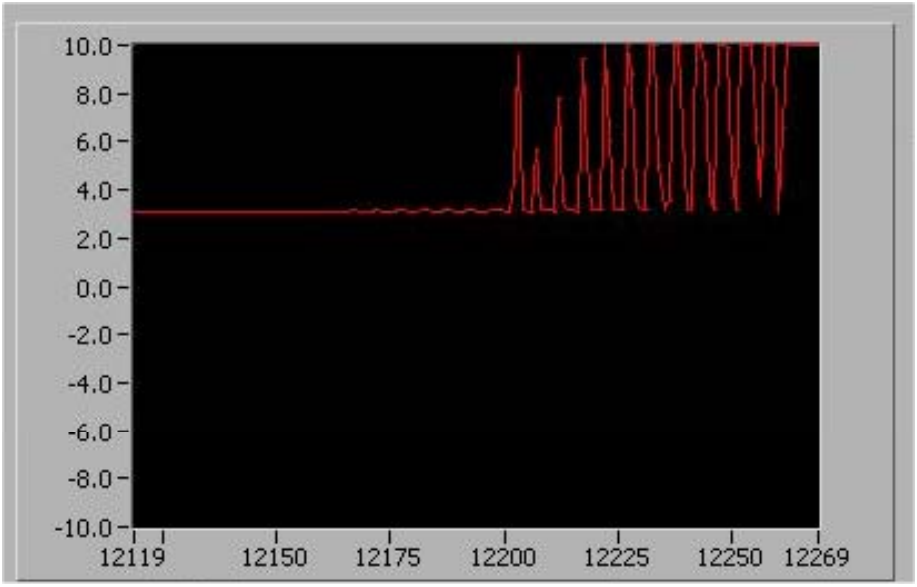

Figure 4.19: Random noise shown in the voltage signal

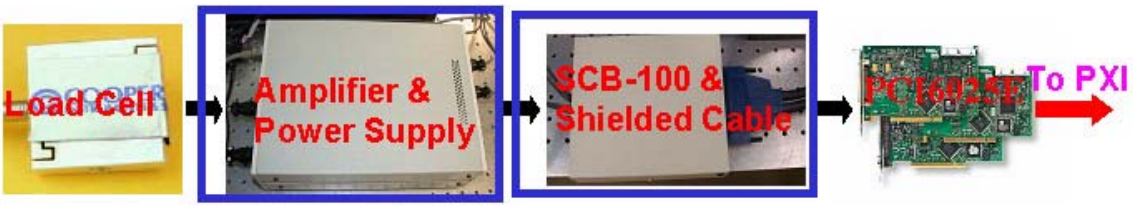

Figure 4.20: Configuration of the new data acquisition system

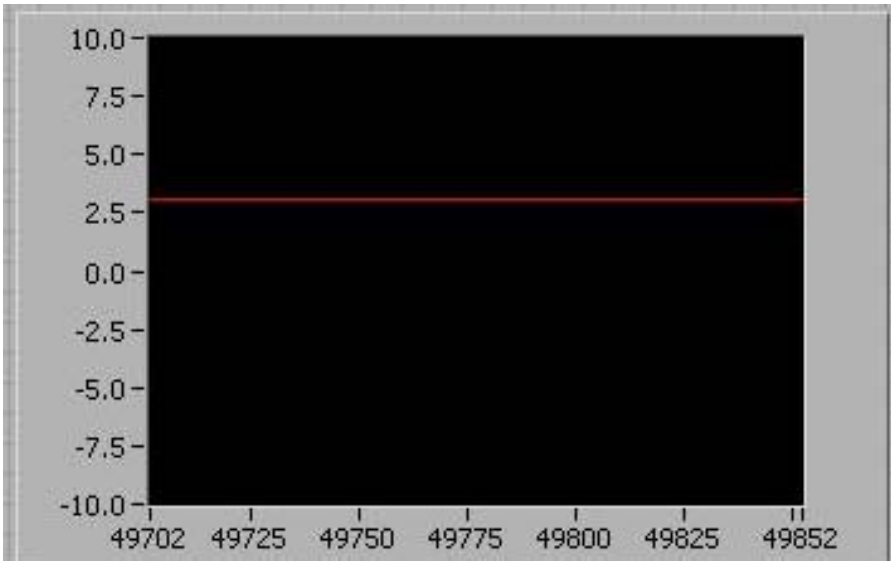

Figure 4.21: Voltage signal without random noise

4.2.4.3 Noise Removal in AFM Imaging

AFM measurement is based on the interaction force between the tip and sample. The interaction force is normally below 10^{-7}. AFM imaging should avoid any noise, including both electrical and vibration. The noise has very apparent effects on the quality of the AFM images, as shown in *Figure 4.19*. Even when the scanning area is 0 by 0 μm and the tip is just vibrating at resonant frequency without any lateral motion over the specimen, the image is very rough and the noise is clearly shown in

the signal window. When the scanning area is 10 by 10 μm, the topographic information can only be vaguely discerned through the noise covering the surface.

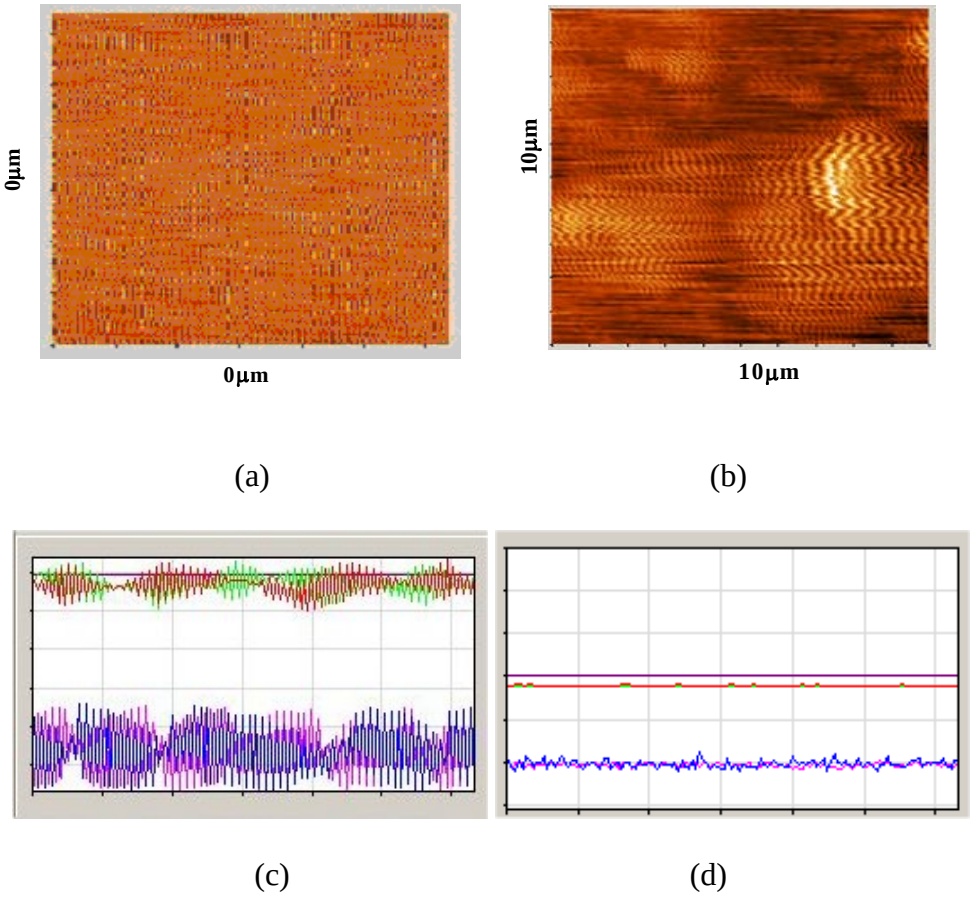

Figure 4.22: Noise in AFM imaging, (a). Scanning area 0 by 0 (b). Scanning area 10 by 10 (c) Noise signal for 0 by 0 μm scanning area (d) Signal without noise for 0 by 0 μm scanning area

There is no guaranteed method to get rid of the noise in the AFM imaging yet. But after extensive experience operating the AFM, there are several things that can be pursued with AFM to eliminate the noise. First, check the cantilever probe of AFM. There are two issues to check:

(a) Check to see if the cantilever probe is loose. The cantilever is attached to a disk using super glue or silver glue as shown in *Figure 4.18.* Then the disk

with the cantilever probe is mounted to the scanner head by magnetism. If the cantilever probe is loose on the top of the disk, the AFM tip won't work properly.

(b) Check to see if the tip is broken. If the tip is broken, the topographic information cannot be detected by the tip and the interaction between the tip and sample will be very random. Then the noise will be shown together with the topographic image.

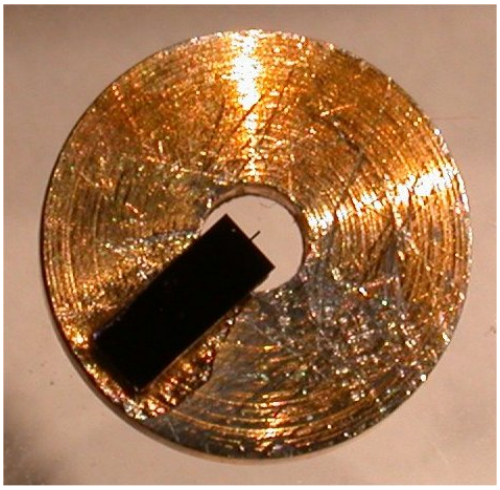

Figure 4.23: Cantilever probe mounted to the disk

Second, check if there is some instrument around with high power consumption and large periodic motion. Instruments with high power consumption may affect power sources to neighborhood. Instruments with large periodic motion, such as vibration and rotation, may cause vibration of the ground and building. Thus it will cause vibrational noise to be transmitted to the AFM. Third, try different cantilever probe directions relative to the scanner head. Normally, the cantilever is aligned along

the scanner head, with the tip pointing out. Sometimes, changing the cantilever direction so that the tip is facing the scanner head will eliminate the noise.

4.3 Summary

In this chapter, experiments were conducted to demonstrate the capability of the biaxial microtensile testing system both for biaxial testing at the microscale and uniaxial testing at the nanoscale. Biaxial testing was conducted on a vinyl specimen with a hole in its center. Digital images were obtained using a CCD camera and optical microscope, with a spatial resolution of 3.6 microns per pixel. The DIC technique was applied to the digital images to calculate the displacement fields and strain fields. The strain fields associated with a biaxial loading ratio of 1:1 are reasonably symmetric, which demonstrates that the system is capable of biaxial testing. Displacements were obtained with a resolution of 0.18 microns, indicating that the technique was capable of sub-micron displacement resolution. Microtensile test results were consistent with FEA and theoretical results, although the effect of finite geometry manifested through the shear strain distribution was better predicted by FEA.

Uniaxial testing was conducted on sputtered nanocrystalline copper film. AFM topographic images were recorded during each incremental loading step with a spatial resolution of 10 nm. These topographic images can be converted to gray scale images with textures that are suitable for DIC. The displacement fields can then be determined from these images with a sub-nanometer resolution of 0.5 nm. The main challenges in conducting the microtensile testing were also discussed, including the motion control, the noise in the data acquisition, and noise in the AFM imaging.

5 Characterization of Scanning Accuracy of Atomic Force Microscope (AFM)

5.1 The AFM Scanning Tube

A key component for an AFM is the scanning tube. The scanning tube is made of piezoelectric ceramics that can rapidly provide the small actuation displacements necessary for scanning at the microscale and nanoscale. Piezoelectric ceramics are a class of materials that expand or contract when in the presence of a voltage gradient or, conversely, create a voltage gradient when forced to expand or contract [Gallego-Juárez 1989]. The working principle for a piezo element is shown in *Figure 5.1(a).* Piezoelectric ceramics make it possible to create highly precise three-dimensional positioning devices.

Most scanning probe microscopes use a tube-shaped scanner head that is composed of four quadrants of piezoelectric ceramics. This is a simple geometric combination that is capable of providing the highly accurate three-dimensional positioning. Four electrodes cover the outer surface of the tube, while a single electrode covers the inner surface. Application of voltages to one or more of the electrodes causes the tube to bend or stretch, moving the cantilever probe in three-dimension as shown in *Figure 5.1(b).* When a positive voltage is applied to any of the quadrants, the tube will tilt away from that quadrant, which produces motion towards

the opposite direction. When same voltage is applied to four quadrants, they will extend or contract with same amount, which produces motion in the z direction.

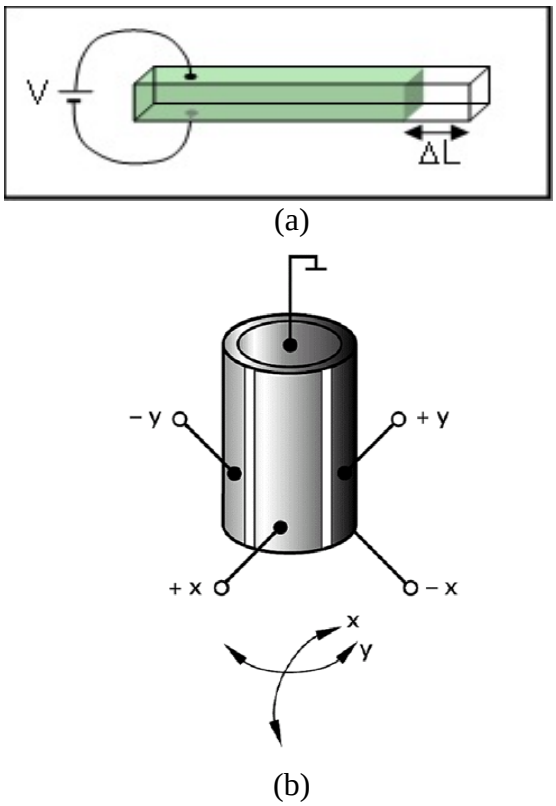

Figure 5.1: (a) Working principle of piezo element, (b) A scanning tube made of four quadrants of piezoelectric material

5.2 Hysteresis of AFM Scanner

The hysteresis of piezoelectric material between the externally applied electrical field and the internal polarization is well known. The internal polarization is proportional to the piezoelectric strain and the displacement of the material. Thus there exists hysteresis between the applied voltage and the deformation of the piezo material. This is the main cause of distortion in AFM images. The hysteresis between

the displacement of the piezo element and the applied voltage has been observed and recorded, as shown in *Figure 5.2* [Dirsche 2000]. The movement of the piezo element is nonlinear when voltage is linearly applied. This nonlinear behavior can be observed when calibration gratings with regular line spacing are scanned using the AFM. A calibration grating with a line spacing of 3 microns was used to illustrate the effects of the hysteresis in the AFM imaging. The image without hysteresis and distortion is shown in *Figure 5.3 (a).* A distorted image is shown *in Figure 5.3(b)* for the trace direction of AFM scanning and *(c)* for the retrace direction of AFM scanning [Dirsche 2000]. The image shows larger feature sizes from left to right in the trace image, while feature sizes become smaller from left to right in the retrace image. Because of the distortion caused by hysteresis, the AFM image can not exactly represent the sample provide the true dimensions of the underlying surface structure.

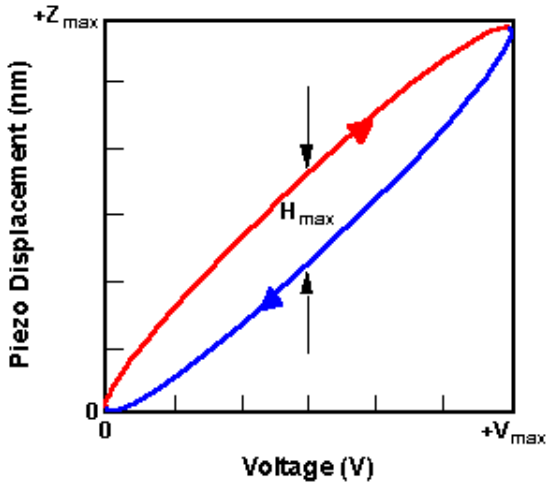

Figure 5.2: Illustration of hysteresis of piezoelectric elements

(a) Hysteresis-free image of a standard sample with line period of 3 micron

(b) Hysteretic image distortion in trace direction

(c) Hysteretic image distortion in retrace direction

Figure 5.3: Standard sample images showing hysteresis

5.3 AFM Nonlinearity Characterization using a Calibration Grating

The nonlinearity of the AFM scanner is always a problem when it is desirable to obtain accurate AFM images. Some newer AFMs have nonlinearity compensator circuits that provide in-situ nonlinearity calibration. Most AFMs do not have the calibration circuits, and the acquired AFM images need to be corrected for nonlinearity afterwards. The nonlinearity characterization of an AFM scanner is

complicated. There are numerous problems associated with obtaining good calibration of the AFM scanner under various operating conditions.

Nonlinearity in AFM scanning caused by the hysteresis of piezo element has been recognized for a long time. Standard micromachined calibration gratings have been conventionally used to measure the nonlinearity. *Figure 5.4* shows a general calibration grating for X-Y plane nonlinearity. It is micromachined from silicon-based material. It comprises a chessboard-like array of square pillars with edge shape determined by the silicon crystal structure, which guarantees the pitch uncertainty of the grating within ±8 nm range.

SPIP, the Scanning Probe Image Processor is an image processing software designed with a focus on characterizing images from Scanning Probe Microscopes, like the AFM, and quantifying the characteristics of the image. To characterize the nonlinearity of the AFM used in this research effort, scanning was first conducted over the surface of the standard calibration grating. SPIP was then applied to the AFM images of the calibration grating to calculate the pixel position errors. The AFM image of a standard X-Y calibration grating is shown in *Figure 5.5(a).* The x position pixel error across the x direction is calculated using SPIP software. The error is plotted versus the x direction position for the image as shown in *Figure 5.5(b).*

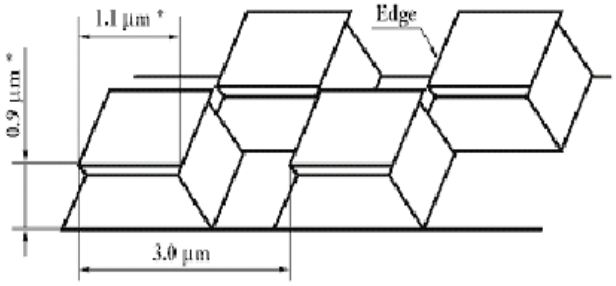

Figure 5.4: Micromachined nonlinearity calibration grating

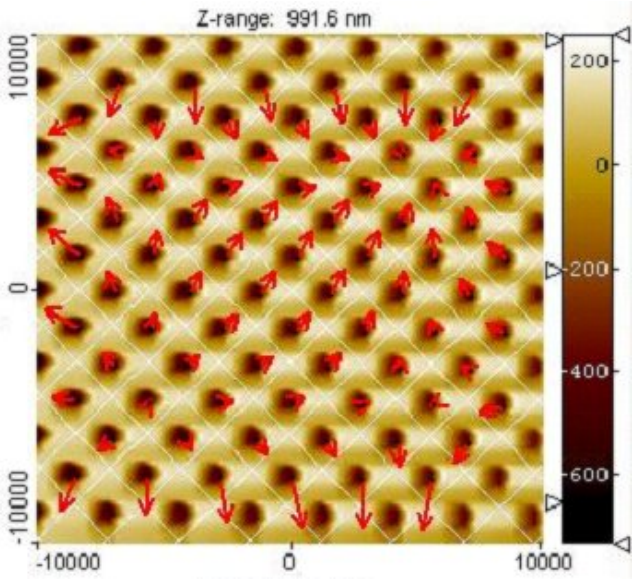

(a)

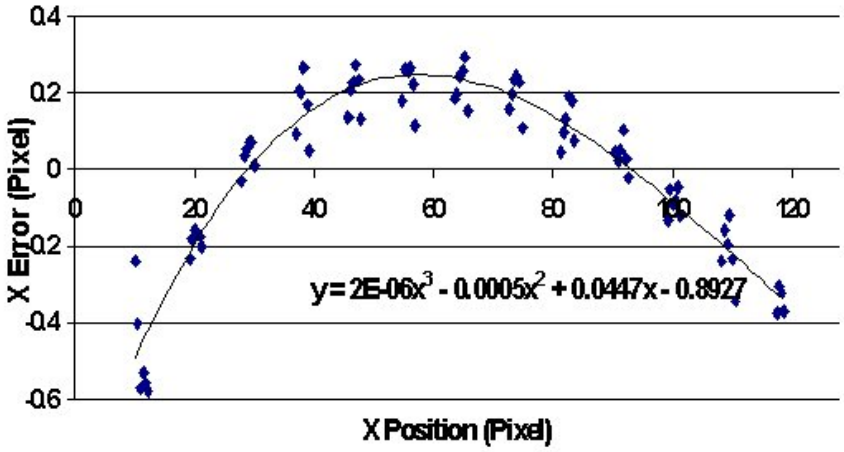

(b)

Figure 5.5: (a) AFM image of standard calibration grating for x-y nonlinearity, (b) X position pixel error versus x position

5.4 Observation of the Nonlinearity of AFM Scanner using DIC Technique on Sputtered Nanocrystalline NiTi Thin Films

As explained in section 5.1, the motion of the scanner head is caused by the deflection or extension of the scanner tube. The cantilever probe is attached to the end of the scanner tube, making interaction between the probe tip and the sample surface. The deflection of the scanner tube can produce the probe offset relative to the original position as illustrated in *Figure 5.6*. In the following work, the DIC technique is applied to topographic AFM images to calibrate the nonlinearity of AFM scanner. The nonlinearity of the AFM is calculated by correlating images with different probe offset values.

As discussed in the section 4.3, topographic AFM images record the microstructure and the grain boundaries of the specimen surface. The randomness of the microstructures forms textures that can be converted to a format which are suitable for the DIC technique. Two gray scale images shown in *Figure 5.7* were converted from AFM topographic images. The images were obtained from two consecutive AFM scanning on a sputtered NiTi sample, the first one with the probe at the original position and the second one with the probe offset of 1 micron in the positive x direction. The scanning area is 5 micron by 5 micron. The scanning resolution is 512 pixels by 512 pixels.

As shown in the *Figure 5.7*, these two images have a common area of 4 microns. The common area in image (a) is located in the second half of the image, while the common area in image (b) is located in the first half of the image. The common area is transferred toward the negative x direction by 1 micron from image

(a) to image (b). Commercial DIC software, Vic2D from Correlated Solutions in Columbia, SC, is applied to the common area of these two images. Theoretically, the DIC result should generate a uniform displacement field of –102.4 pixels as shown in *Figure 5.8(a)* since the displacement is 1/5 of the total scanning area and the scanning resolution is 512 pixel in each direction. However, the actual displacement field shows variation of displacement throughout the x direction, and the average magnitude is less than the ideal value. The actual value calculated from Vic2D using 49 pixel subsets is shown in *Figure 5.8(b).* Ten images both without probe offset and with probe offsets of 1 micron were obtained. DIC was applied to each pair of these images to calculate the displacement. All the displacement fields obtained from these images are very similar to the displacement field shown in *Figure 5.8(b).* The displacement variation is about 6 pixels over the AOI.

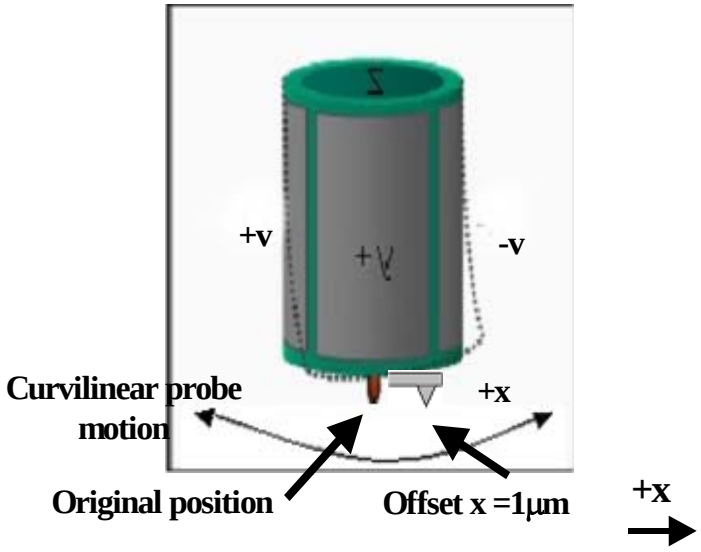

Figure 5.6: Conceptual design of scanner tube and the probe offset produced by the deflection of the scanner tube

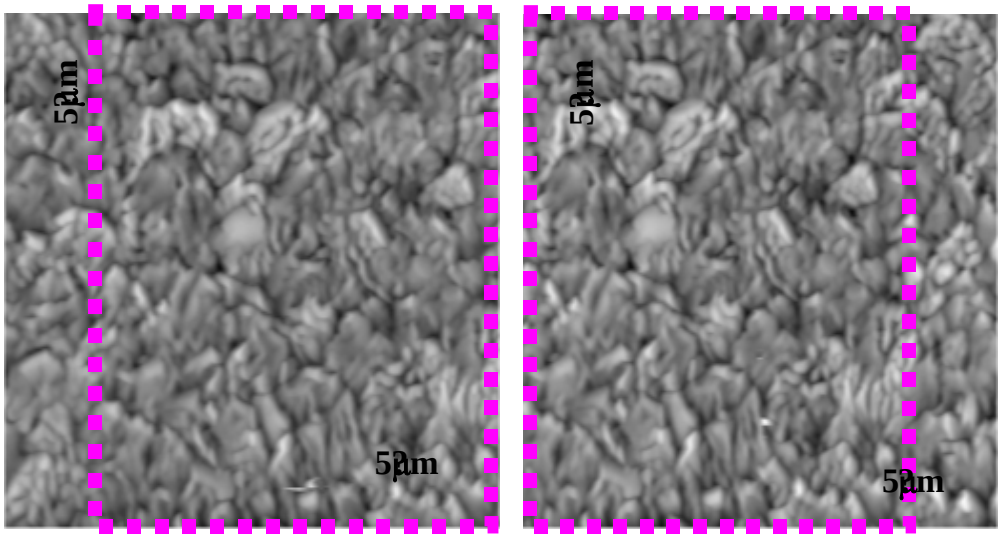

(a) (b)

Figure 5.7: Gray scale images converted from AFM topographic images of sputtered nanocrystalline NiTi film (a) Scanned with probe at the original position; (b) Scanned with probe offset x=1 micron

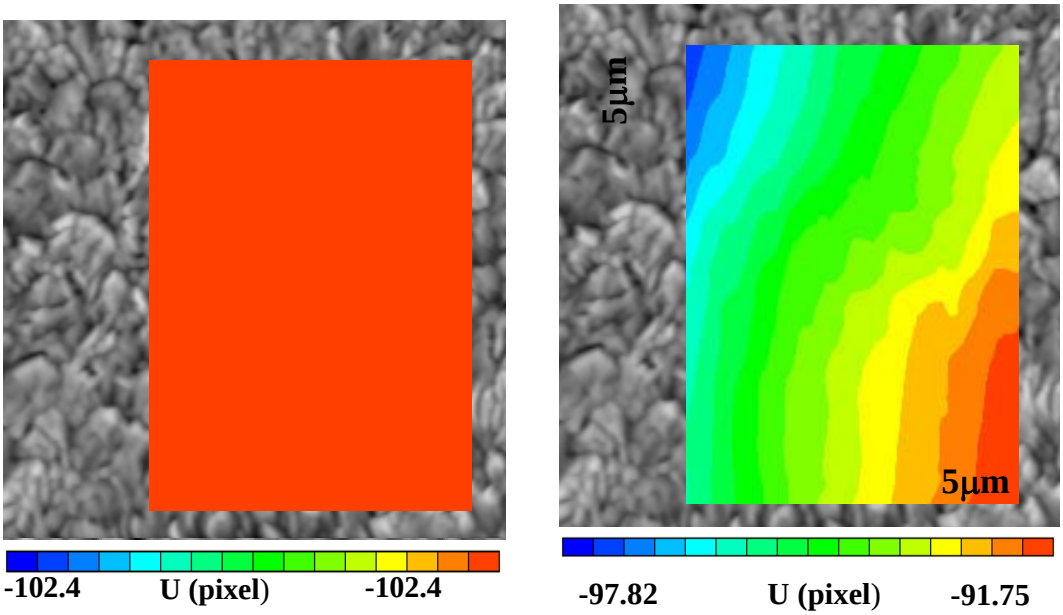

Figure 5.8: DIC results on common area of two images without probe offset and with probe offset x=1 µm, (a) ideal displacement field; (b) actual displacement field

DIC technique was also applied to images from consecutive scans with the same probe offset value. Shown in *Figure 5.9(a)* is the ideal displacement filed for two images without nonlinearity distortion. The displacement field should be all zero throughout the whole correlation field. The actual displacement field calculated from the Vic2D is shown in *Figure 5.9(b).* It shows some non-zero values. But all the absolute values are smaller than 0.05 pixel, which means that the AFM scanning has high repeatability among the consecutive scans with same probe offset value.

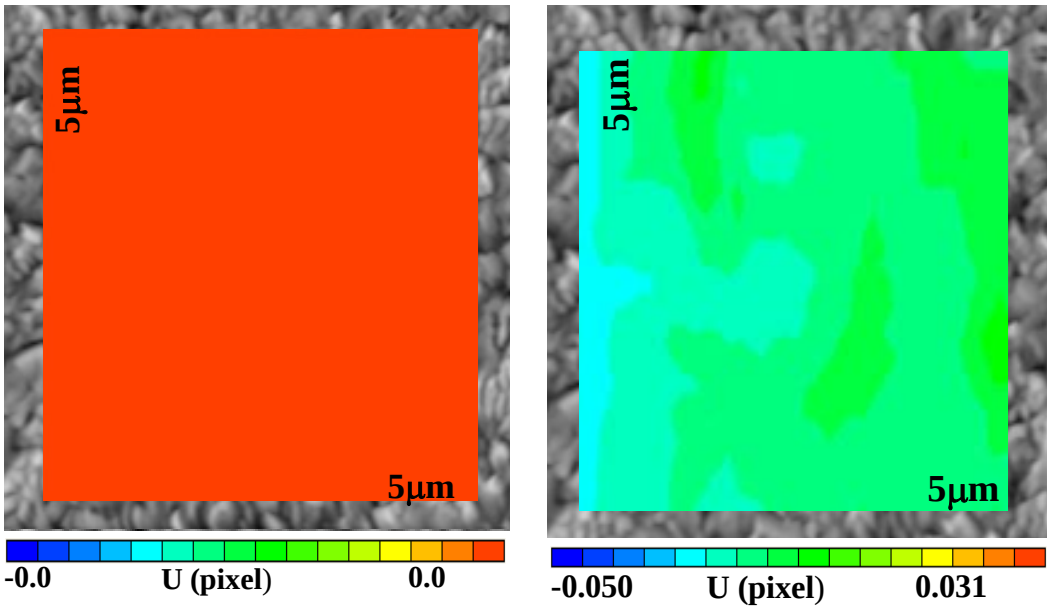

(a) (b)

Figure 5.9: DIC results on two consecutive scanning images with same probe offset value, (a) ideal displacement, (b) actual displacement from images with nonlinearity

Similarly, DIC technique was applied to images without probe offset and with probe offset value of 0.5μm, 1.5μm and 2μm. Ideally, the displacement between the image without probe offset and with probe offset of 0.5μm should be -51.2 pixels. The apparent displacement field calculated from DIC is shown in *Figure 5.10(a).* The

displacement field varies from –46.93 to –43.89 pixels. It has about 3 pixels displacement variation across the correlation field. The ideal displacement between the image without probe offset and with probe offset of 1.5μm should be -153.6 pixels. The apparent displacement field calculated from DIC is shown in *Figure 5.10(b).* The displacement field varies from –148.35 to –139.54 pixels. It has about 8.8 pixels displacement variation across the correlation field. The ideal displacement between the image without probe offset and with probe offset of 2μm should be –204.8 pixels. The apparent displacement field calculated from DIC is shown in *Figure 5.8(c)*. The displacement field varies from –198.51to –188.01 pixels. It has about 10.5 pixels displacement variation across the correlation field. This uniform variation in displacement equates to an artificial strain caused by the probe offset, and is plotted out for different offset values in *Figure 5.11.* The artificial strain due to the probe offset can be as large as 4% for images with a probe offset of only 2 microns in a 5 micron by 5 micron scanning area. This is a substantial amount of strain as compared to the deformations that are of interest in mechanical characterization, therefore the nonlinearity of AFM scanner needs to be characterized and eliminated from these displacement fields in order to obtain actual deformation measurements.

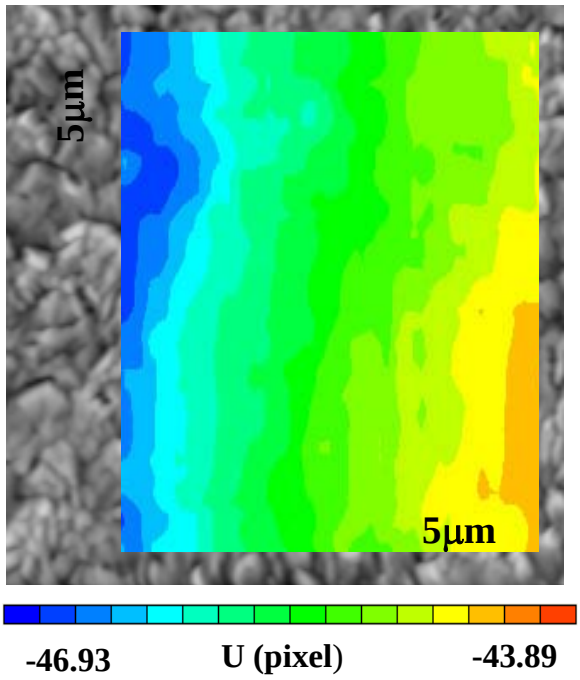

(a)

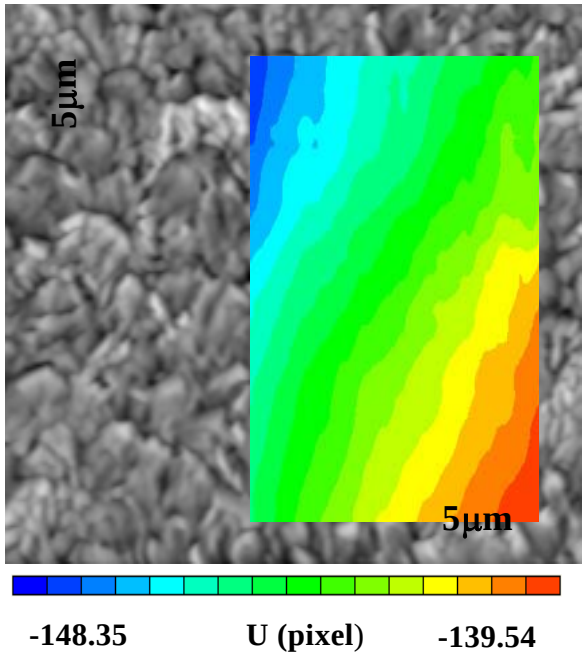

(b)

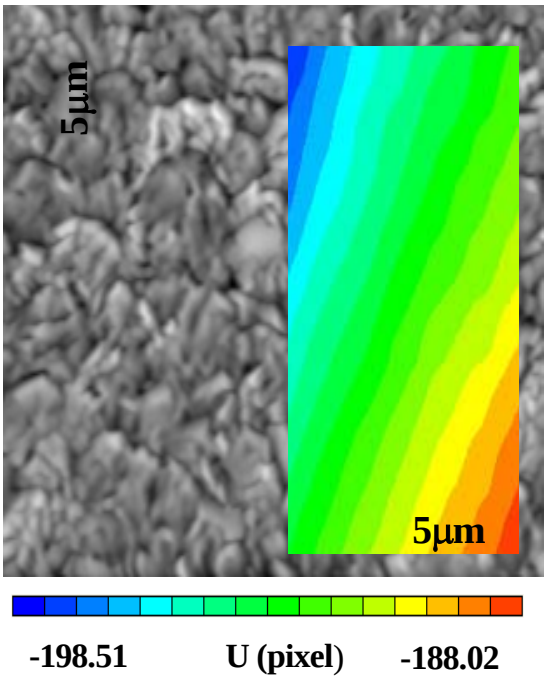

(c)

Figure 5.10: Displacement field calculated between images without probe offset and with probe offset of (a) 0.5µm, (b) 1.5µm, and (c) 2µm

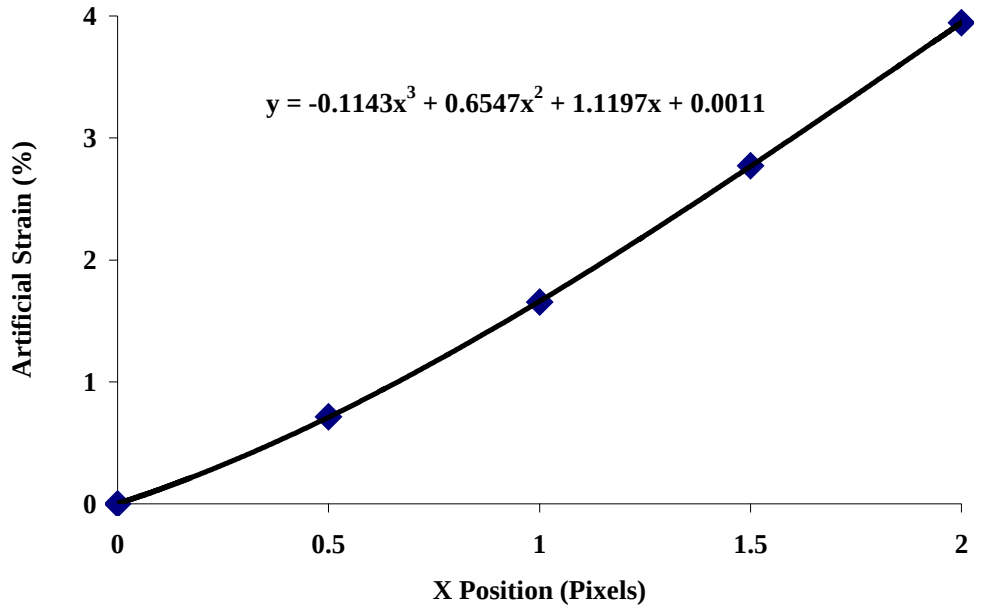

Figure 5.11: The artificial strain caused by different probe offset values

5.5 Comparison of Nonlinearity Results from SPIP and DIC

As discussed in section 5.3, conventional method for the calibration of nonlinearity of AFM scanner is to use micromachined calibration gratings. AFM images were obtained from the standard calibration grating. Then software SPIP was applied to these AFM images to calculate the position errors. The position error versus the position curve can be obtained from the calibration grating. The X-Y nonlinearity calibration grating was scanned with different probe offset values. The resolution of the scanned image is 128 pixels by 128 pixels. The curves for x position error versus x position were plotted out for different offset values as shown in *Figure 5.12.* It is shown that the nonlinearity curves are the same for images with different probe offset values.

The next step is to compare the nonlinearity calculated from the calibration grating with the displacement variation from the DIC results. For the common area in the two consecutive images, one with probe at the original position and the other with probe offset x=1 micron as shown in *Figure 5.13,* the relative position of this common area in these two images is different. It is located on the right side half of the first image, but on the left side half of the second image. Therefore, the position of the common area in the nonlinearity curve from SPIP is different. It corresponds to the right side part of curvature in the error curve for the first image, while it corresponds to the left side part of the curvature of the error curve for the second image. These two parts of curvatures are different as shown in *Figure 5.14.*

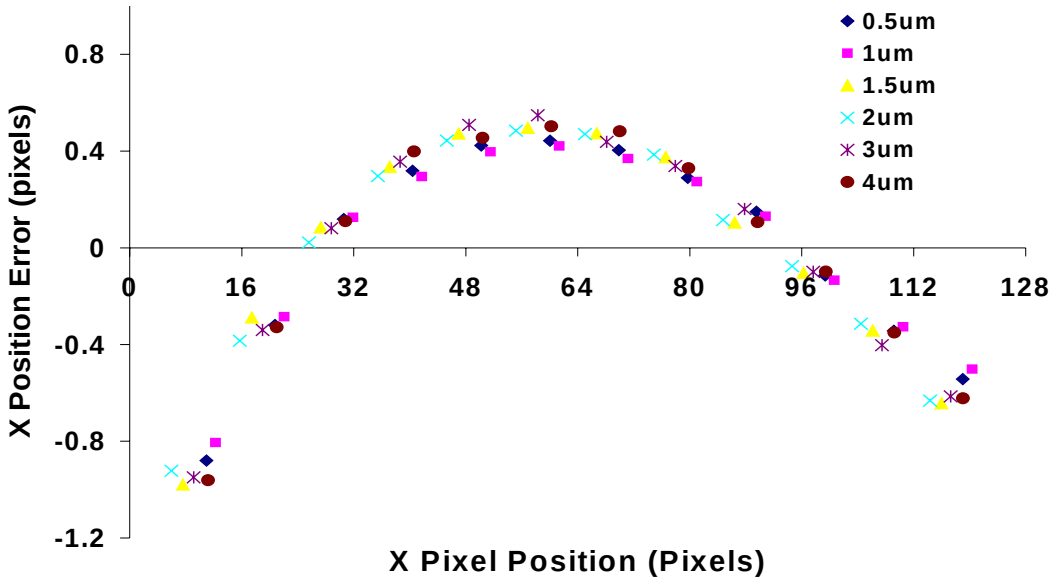

Figure 5.12: The x position errors for images with different probe offset values

Figure 5.13: Two consecutive AFM images of NiTi film, the first one with probe at the original position and the second one with probe offset of 1 micron

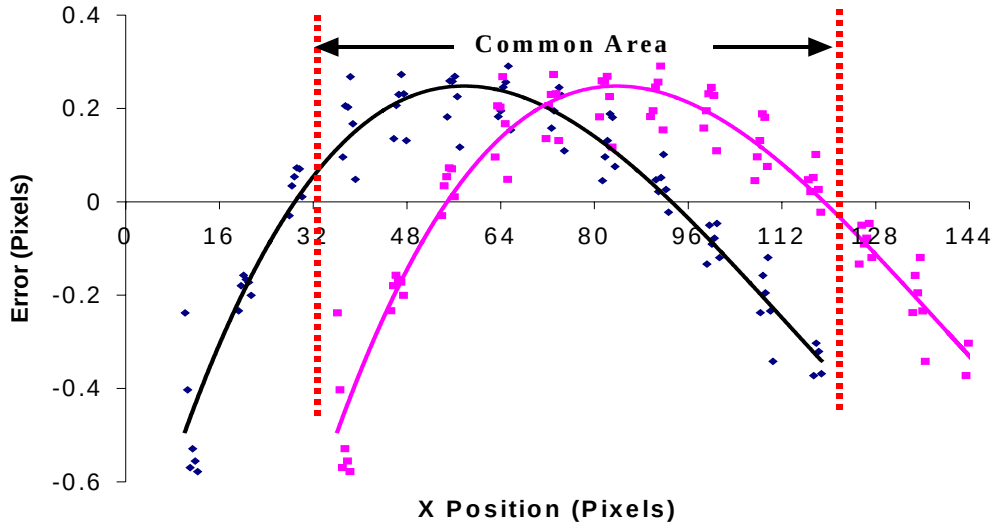

Figure 5.14: The position error curves calculated from two consecutive images

As shown in *Figure 5.14*, the two images with and without probe offset have different curvature in the nonlinearity curve. The difference of the position errors from these two curves is plotted out for the common area. In contrast, the displacement field from DIC has variation across the x direction as shown in *Figures 5.8* and *5.10*. The displacement variation relative to the mean value of the displacement is also plotted out for the correlation area. The difference of the x position error and the displacement variation were plotted together in *Figure 5.15 (a)* for the images without probe offset and with probe offset of 1 micron. It can be seen that these two curves match with each other for the common area. Also, the difference of the position error calculated from SPIP and the displacement variation from DIC were compared for images with a probe offset of 0.5 micron and a probe offset of 2 micron. The results are consistent over the common area.

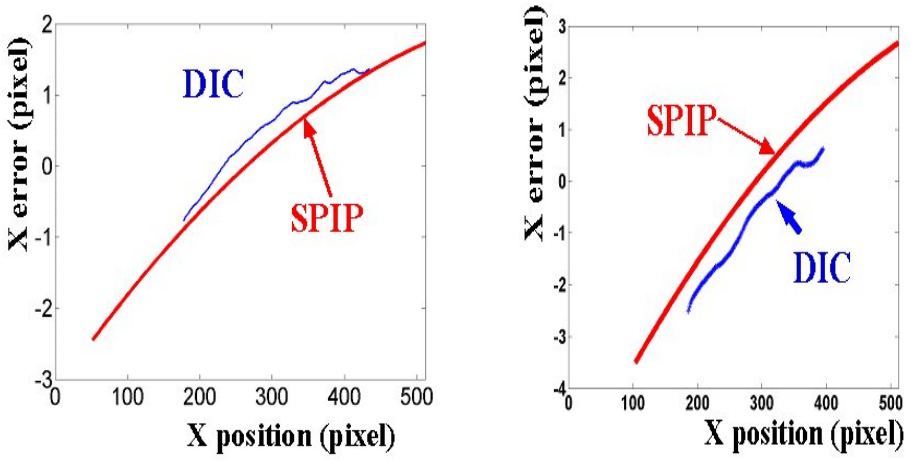

(a) (b)

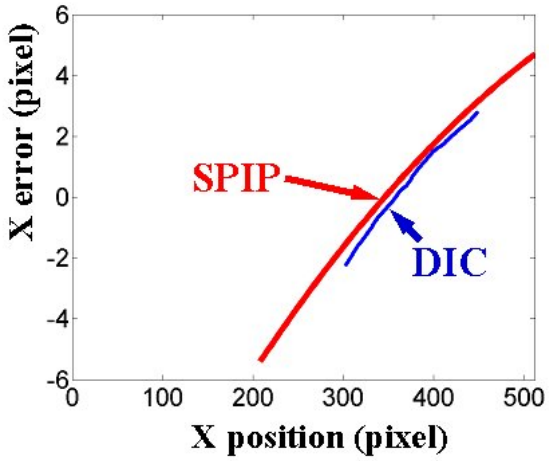

(c)

Figure 5.15: Comparison of displacement variation calculated using SPIP and DIC (a) Offset x=0.5 micron, (b) offset x=1 micron (c) offset x=2 micron

From the comparison results shown above, it is demonstrated that the new calibration method using DIC technique on AFM images of the NiTi film can be used to calibrate the nonlinearity of the AFM scanner. In the conventional calibration method, special micromachined calibration grating with high accuracy is needed. Due

to the limitation of the fabrication technique and cost, the size of the calibration grating is normally at the micron scale. Large scanning areas, normally about a few micrometers, are needed to have enough features of the calibration grating so that the nonlinearity can be calculated from these features. In the new calibration method, AFM images were obtained from materials with nanometer size features. The nonlinearity can be calibrated for scanning areas ranging from submicron to a few microns in dimension. This new method provides another option for calibrating the nonlinearity of AFM scanner that uses any surface of interest rather than a highly specialized calibration grating, resulting in a more direct assessment of the scanning accuracy for deformation measurements.

5.6 Apply New Nonlinearity Calibration Technique to the Displacement Field from the Microtensile Testing

As discussed in section 4.2.3.2 and 4.2.4.1, the different probe offset was used to obtain images from same AOI for the each incremental step of the load during the microtensile testing. The nonlinearity of displacement due to the different probe offset values has to be removed from the results to get the actual displacement values. The new proposed nonlinearity characterization technique is applied to the displacement field obtained from the microtensile testing, as shown in previous *Figure 4.16.* Thus, the nonlinearity of displacement field due to the probe offset for step *j* has to be characterized first. Two AFM topographic images were obtained from same step *j*, one with probe at the original position, the other one with probe offset of 0.5 micron in y direction. The DIC technique was then applied to these two images to

calculate the displacement caused by the probe offset value. The ideal displacement value due to probe offset of 0.5 micron should be –25.6 pixels since the total scanning resolution is 256 by 256 pixels over the area of 5 micron by 5 micron. But the actual displacement fields due to the probe offset show nonlinearity and variation as shown in *Figure 5.16.* It also shows that the *U* displacement field is not affected by the probe offset in y direction, while the *V* displacement field is clearly affected by the probe offset in y direction. Thus, in order to obtain the real displacement fields for the microtensile testing, the displacement fields due to probe offset as shown in *Figure 5.16* should be subtracted from the results shown in *Figure 4.16.*

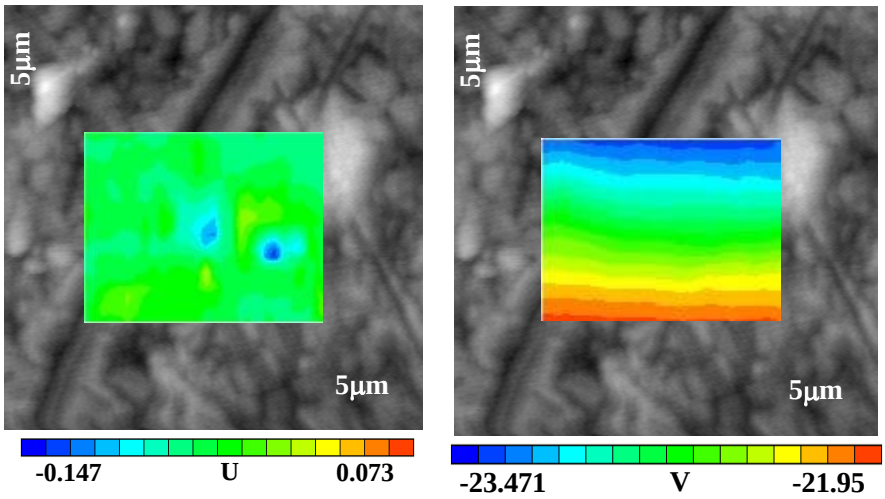

(a) (b)

Figure 5.16: The *U* and *V* displacement fields due to the probe offset in y direction of 0.5 micron

5.7 Summary

The nonlinearity of AFM scanning due to the hysteresis of the piezo element is well recognized and characterized. The conventional method to characterize the nonlinearity is to use a specialized micromachined calibration grating. In this work, a new method using DIC technique on the AFM images of nanostructured materials was proposed. The nonlinearity of AFM imaging due to the probe offset was calculated using this new method in order to determine the apparent strain induced when measuring displacement fields at the nanoscale. The results matched well with those from the conventional method. In this new method, a specialized micromachined grating is not needed. The calibration can therefore be conducted on any surface of interest with areas ranging from submicron to several microns in dimension to provide a more direct assessment of the scanning accuracy for deformation measurements.

6 Development of Pointwise Digital Image Correlation (DIC) Technique

6.1 Limitations of Conventional Digital Image Correlation Technique

Digital image correlation is a full-field deformation measurement technique that mathematically compares a subset of image from a reference configuration with a subset of image from deformed configuration. This technique uses gray or laser speckle patterns on the specimen to obtain the deformation of a surface via comparison of the digitized undeformed and deformed images. A CCD camera was first used to obtain the images, which were digitized into an array of pixels that can be as large as 4 megapixels. The intensity of each pixel was represented by an integer ranging from 0 to 255, where 0 represents black and 255 represents white. Digital image correlation then becomes the job of comparing subsets of numbers representing these two images [Bruck *et al*, 1989]. The typical objective correlation function $S(x,y,u,v,u_x,u_y,v_x,v_y)$, which measures how well subsets match, is given in as follows:

$$S(x,y,u,v,u_x,u_y,v_x,v_y) = 1 - \frac{\sum [F(x,y) * G(x^*,y^*)]}{[\sum F(x,y)^2 * \sum G(x^*,y^*)^2]^{1/2}} \tag{6.1}$$

$$\begin{aligned} x^* &= x + u + u_x \Delta x + u_y \Delta y \\ y^* &= y + v + v_x \Delta x + v_y \Delta y \end{aligned} \tag{6.2}$$

where $F(x, y)$ is the gray value for subset at coordinate (x, y) in the reference image, $G(x^*, y^*)$ is the gray value at coordinate (x^*, y^*) in the deformed image. The coordinates (x, y) and (x^*, y^*) are related by the displacements (u, v) as in *equation (6.2)*, where (u, v) are displacements for the subset centers in the x and y directions respectively. The terms Δx and Δy are the distances of point (x,y) to the center of the subset. The image correlation is performed to determine the values for u, v, u_x, u_y, v_x, v_y that minimize the correlation function $S(x, y, u, v, u_x, u_y, v_x, v_y)$. Generally, the deformation within the subset is approximated by first order displacement gradients u_x, u_y, v_x, v_y.

In the conventional DIC technique, a subset-based correlation algorithm is employed to mathematically match subsets of intensity data from an initially undeformed image with subsets of intensity data from a deformed image that are reconstructed with subpixel accuracy using interpolation schemes. A zero-order or first order approximation of the variation in displacement fields (i.e., displacement gradients) relative to the subset center must be assumed to describe the deformations of pixels within the subset in order to resolve displacement fields using the DIC technique, while higher-order approximations must be used for more inhomogeneous deformations. The lower-order assumption is usually adequate for measuring mechanical deformations in homogeneous materials, unless a boundary associated with a crack or interface is encountered. In these instances, the deformation field changes extremely rapidly or discontinuously within the subset, violating the assumed nature of the displacement gradients and making it impossible to converge on a solution for displacement fields using the correlation algorithm. Therefore, the

conventional DIC technique needs to be modified in order to be suitable for rapidly varying or discontinuous deformation fields, such as those associated with the interfaces like grain boundaries.

6.2 Parametric Study of the Pointwise Digital Image Correlation Technique

The purpose of the pointwise DIC is to remove the constraint of constant displacement and displacement gradients within a subset, and to permit the displacement field to vary discontinuously, as might be expected when a subset overlays an interface or crack. This will enable the technique of DIC to achieve the sub-pixel spatial resolution even the displacement field is associated with crack or interface. Pointwise DIC provides kinematic descriptions of the displacement field that are independent of position in a subset (i.e., *pointwise*). The kinematic description that is employed involves assessing the displacement of each pixel independently (i.e., pointwise) with sub-pixel accuracy. This results in a larger number of parameters to optimize in the objective correlation function. Therefore, a Genetic Algorithm (GA) was employed in the pointwise DIC technique to provide a simpler and more robust optimization method than those achieved using other gradient-based or coarse-fine search methods. The effects of GA parameters, Crossover probability and Mutation rate on the correlation function value were studied. Also the effects of the different constraint types over the displacement fields have been compared.

6.2.1 Correlation Function of Pointwise DIC

Unlike conventional DIC, the objective correlation function of pointwise DIC, $S(x_\alpha(i,j), x_\alpha^*(i,j))$, is given as follows:

$$S(x_\alpha(i,j), x_\alpha^*(i,j)) = 1 - \frac{\sum[F(x_\alpha(i,j)) * G(x_\alpha^*(i,j))]}{[\sum(F(x_\alpha(i,j)))^2 * \sum(G(x_\alpha^*(i,j)))^2]^{1/2}} \quad (6.3)$$

Where $F(x_\alpha(i,j))$ is the intensity value at coordinate $x_\alpha(i,j)$ in the undeformed image, while $G(x_\alpha^*(i,j))$ is the intensity value at coordinate $x_\alpha^*(i,j)$ in the deformed image. The coordinates $x_\alpha(i,j)$ and $x_\alpha^*(i,j)$ are related by the displacements $u_\alpha(i,j)$ as follows:

$$x_\alpha^*(i,j) = x_\alpha(i,j) + u_\alpha(i,j) \quad (6.4)$$

In all previous work, the subsets in deformed image are defined using displacement u and v, displacement gradient u_x, u_y, v_x, v_y, for first order approximation and $u_{xx}, u_{yy}, v_{xx}, v_{yy}, u_{xy}, v_{xy}$ for the second order approximation. For pointwise DIC, each pixel is given an independent displacement $(u_1(i,j), u_2(i,j))$. The total number of displacement variables will be twice of the number of the pixels in the subset instead of the 2 displacements and 4 displacement gradients in conventional DIC.

The coordinate system chosen for the description of pixel locations in the image is shown in *Figure 6.1*. Where x_1, x_2 are coordinate positions of pixels, u_1, u_2 are

displacements in x_1 and x_2 directions, and (i, j) is the relative location of each pixel in the subset. A speckle pattern image used in this investigation is shown in *Figure 6.2* representing the rotation of a specimen.

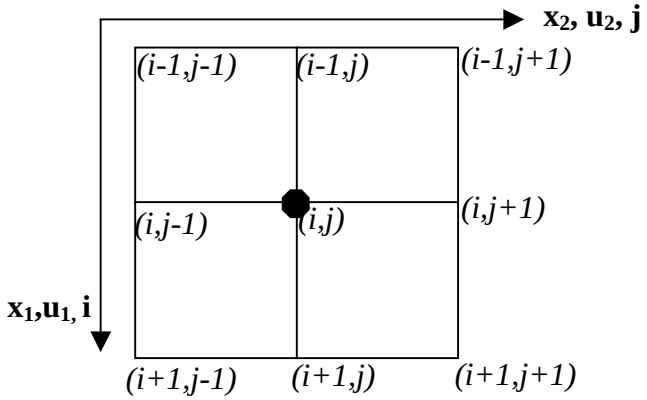

Figure 6.1: Coordinate system for description of location of pixels in the pointwise DIC analysis

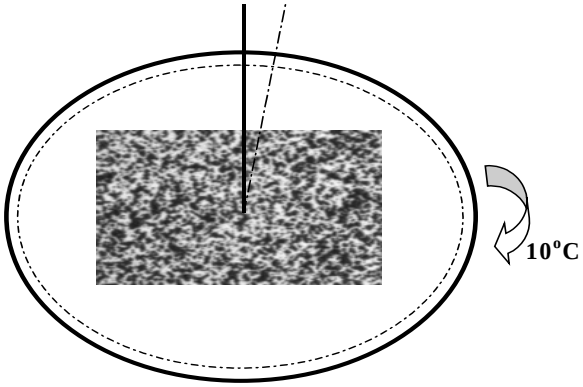

Figure 6.2: Speckle image used for comparative DIC analysis on rotating disc specimen

6.2.2 **Bilinear and Bicubic Interpolation Scheme**

Because the displacements in *equation (6.4)* can assume sub-pixel values, an interpolation scheme must be employed to determine the intensity values at sub-pixel locations. Thus, sub-pixel displacement resolution can be achieved. The simplest form of interpolation is the bilinear scheme. In bilinear interpolation, the intensity at point $(x_1^*(i,j), x_2^*(i,j))$, which is located among pixels numbered (i,j), $(i+1,j)$, $(i,j+1)$, $(i+1,j+1)$, is approximated as follows:

$$G(x_\alpha^*(i,j)) = a_{00} + (a_{10} - a_{00})\Delta x_1 + (a_{01} - a_{00})\Delta x_2 + (a_{11} + a_{00} - a_{01} - a_{10})\Delta x_1 \Delta x_2 \qquad (6.5)$$

Where a_{00} = intensity value of pixel (i,j)

a_{10} = intensity value of pixel $(i+1,j)$

a_{01} = intensity value of pixel $(i,j+1)$

a_{11} = intensity value of pixel $(i+1,j+1)$

Δx_1 and Δx_2 are the sub-pixel distances of the point from pixel (i,j). There are only four coefficients to calculate the sub-pixel intensities in bilinear interpolation schemes. The bilinear interpolation is the most computationally efficient scheme, but with the sacrifice of accuracy in reconstructing the image. Some more complex higher order interpolation schemes, such as bicubic interpolation, have been previously employed for DIC analysis [Bruck *et al*, 1989].

Bicubic interpolation uses sixteen coefficients to calculate the subpixel intensity values. The formula for calculating the intensity is given as follows:

$$G(x_\alpha^*(i,j)) = a_{00} + a_{10}(\Delta x_1) + a_{20}(\Delta x_1)^2 + a_{30}(\Delta x_1)^3 + a_{01}(\Delta x_2) + a_{11}(\Delta x_1)(\Delta x_2) + a_{21}(\Delta x_1)^2(\Delta x_2) + a_{31}(\Delta x_1)^3(\Delta x_2) + a_{02}(\Delta x_2)^2 + a_{12}(\Delta x_1)(\Delta x_2)^2 + a_{22}(\Delta x_1)^2(\Delta x_2)^2 + a_{32}(\Delta x_1)^3(\Delta x_2)^2 + a_{03}(\Delta x_2)^3 + a_{13}(\Delta x_1)(\Delta x_2)^3 + a_{23}(\Delta x_1)^2(\Delta x_2)^3 + a_{33}(\Delta x_1)^3(\Delta x_2)^3 \quad (6.6)$$

where all the coefficients can be calculated to guarantee C^2 continuity by using bicubic spline functions, and the Δx_1 and Δx_2 are the relative sub-pixel locations. This makes bicubic interpolation far more computationally intensive than bilinear interpolation but more accurate. In the following work, both bilinear and bicubic interpolation schemes are applied to different deformation cases to investigate the accuracy of reconstructing the deformed and undeformed images for pointwise DIC.

6.2.3 Correlation Function Optimization using Genetic Algorithms (GAs)

6.2.3.1 Genetic Algorithms Optimization Method

The Genetic Algorithm (GA) is an optimization method inspired by natural evolution: the Darwinian principle of survival and reproduction of the fittest [Koza *et al*, 1999]. It is an optimization technique based on concepts of natural selection and genetics. In this approach, the variables are represented as genes on a chromosome. Genetic Algorithm creates a population of chromosomes, then applies crossover and mutation to the individuals in the population to generate new individuals. It uses various selection criteria so that it picks the best individuals for mating (and subsequent crossover). The objective function determines how 'good' each individual

is. Through natural selections and the genetic operations, crossover and mutation, chromosomes with better fitness will propagate in future populations.

The GA starts with initial population (generation 0) that consists of random individuals (Chromosomes). It iteratively performs the following sub-steps on the population in each generation until the termination criterion has been satisfied.

(1). Calculate the fitness for each individual population and select the best one in the generation.

(2). Create new population by applying genetic operations with specified probabilities.

(a) *Reproduction*: Copy the selected member into the new generation.

(b) *Crossover*: Create new population members by recombining sub-string from selected individuals at a chosen crossover probability.

(c) *Mutation*: Create new population member by randomly mutating the individuals at given percentage. This introduces a certain amount of randomness to the search which crossover itself cannot provide.

6.2.3.2 Implementation of GA in pointwise DIC

The pointwise DIC technique can permit a large number of unknown displacement variables to be determined simultaneously. To determine the optimal value of the correlation function given in *equation (6.3)* for a large number of variables, a Genetic Algorithm (GA) can be employed. GA has several advantages over more conventional optimization schemes, such as gradient descent, though it is more computationally intensive:

(a) It is less likely to get stuck on a local maximum or minimum.

(b) It can handle large-scale optimization problems.

(c) It can be employed to many different optimization problems.

In pointwise DIC, each pixel is given variation in the x_1 and x_2 directions. For an area of 20 by 20 pixels, the number of variables will be 800. Therefore, the optimization is very computationally intensive. Meanwhile, the exact analytical relation between the variables and the objective function is not known. These two features of the correlation function optimization problem make the GA optimization method the best choice for this problem.

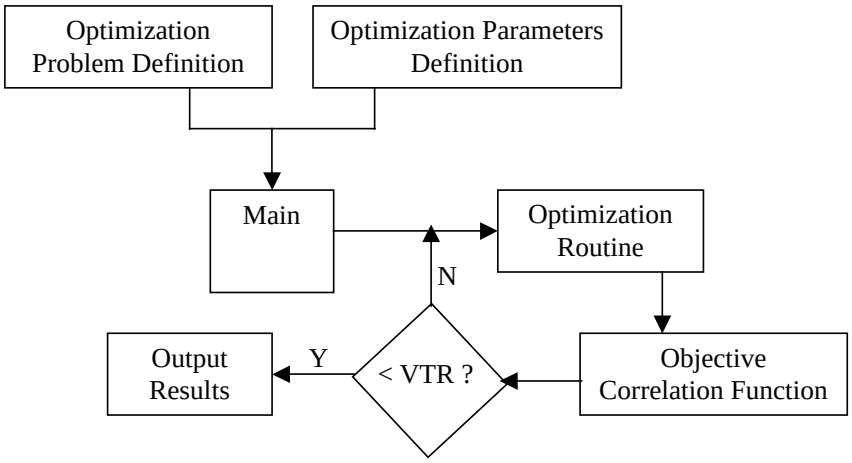

Figure 6.3: The diagram of the implementation of GA

First, the user needs to define the problem of optimization and optimization parameters in the main function. In the case of pointwise DIC, both undeformed and deformed images should be digitized and imported into the main program. The area for correlation is specified from the original undeformed image. The optimization variables, $x_1^*(i, j)$ and $x_2^*(i, j)$ displacement for each pixel are also defined and the

maximum and minimum values for the variables are specified. Second, these parameters are passed into the GA optimization routine program to randomly generate the initial population members. These population members are evaluated and the fitness is computed in the correlation program. The population members with better fitness will pass into the next generation for mutation and crossover. The correlation function value from the fittest member is compared with the value-to-reach (VTR). If the correlation function value is smaller than VTR, the fittest population member will be output as the final value to the optimization variables. If the correlation function value is larger than VTR, these members will be used as the parent members to generate the children members for mutation and crossover operations. The optimization routine will continue until the VTR value or the total number of the iterations is reached.

6.2.4 Parametric Study for Genetic Algorithm Optimization Method in DIC

The GA optimization algorithm used in this problem is a Differential Evolution (DE) method. DE uses a weighted difference (*F*) of population members to generate new members before crossover, thereby resulting in faster convergence characteristics [Storn 1997]. The main parameters required for this optimization are as following:

(1). *VTR* (Value to Reach): This is the determination for the termination of the optimization procedure. If the value is reached, the optimization is terminated and the values of the optimization variables are output. A value of 1.0e-6 is normally chosen to terminate the optimization;

(2). *XVmin and XVmax*: They are the vectors of bounds of the initial population. The interval of [XVmin, XVmax] should cover the region where the global minimum is expected. The initial population will be generated randomly in the range of these two vectors. In pointwise DIC, assuming that the extension and compression strain should be less than 100% and the pixels should not overlay with each other, the minimum and maximum value is set to be –1 and 1;

(3). *D*: the number of parameters in the objective function. In pointwise DIC, there are two variables for each pixel. The total variables will be twice of the pixel numbers $N \times N$. In case of 20x20 pixel area, D is equal to 800;

(4). *NP*: the number of individual population members. Each population member has number of D variables;

(5). *Itermax*: the maximum iteration number. The optimization will be terminated after this number of iterations even if the VTR is not reached;

(6). *F*: the DE stepsize,

(7). *CR*: crossover probability;

(8). *Strategy*: There are 10 different strategies to generate the new population from their parents;

(9). *Refresh*: the number of iterations to print out the intermediate results;

Among the above nine parameters, only four of them will affect the optimization routine and results. (1) *D*: number of variables for the objective function (analogous to the length of a chromosome, i.e., the number of genes present on the chromosome), (2) *NP*: number of individual population member (i.e., the number of chromosomes in the population), (3) *CR*: crossover probability, and (4) *F*: the DE step size.

In this investigation, 20×20 subsets were chosen from a gray digital image with random speckles. As previously discussed, each pixel has two variables, $(u_1(i, j), u_2(i, j))$, to describe their deformation. Therefore, there are 800 variables for the objective function, that is, the chromosome includes 800 independent genes.

Larger population sizes (NP) increase the amount of variation present in the population at the expense of requiring more fitness function evaluations that will intensively increase the computation time. The best population size is dependent upon both the application and the length of the chromosome. Considering both computation time and performance of GA, a population size of 20 was chosen.

Crossover probability has a significant effect on the convergence rate and correlation function value. The convergence rate and optimum correlation function value were studied for different CR values of 0.05, 0.1, 0.2, 0.25, 0.3, 0.5, 0.75 and 0.95 under same mutation value of 0.8. The results are compared in *Figure 6.4(a) and (b).* From this complete study, it shows better initial convergence rate for a larger CR value. A CR value of 0.95 gives the fastest initial convergence, but it ends up a large optimal correlation function value of 0.0039. A CR value of 0.25 gives a slower initial convergence rate than CR of 0.95, but it gives the best correlation function value of 0.000813 after 15000 iterations.

In this investigation, the Differential Evolution (DE) method was employed in the crossover algorithm because of its superior efficiency [Storn 1997]. New population members were generated by multiplication of the DE step size and the difference between two randomly selected population members. F can be varied between 0 and 2. Constant F values of 2.0, 1.6, 1.2, 1.0, 0.9, 0.8, 0.6, 0.4 and 0 were tested for the

optimal CR value of 0.25. The convergence rates and the corresponding ultimate correlation function values after 15,000 iterations for different F values are shown in *Figure 6.5(a) and (b).* From the convergence rate, it is clear that larger Fvalues give faster initial convergence rates. Different F values gave different optimal correlation function values, with F=0.8 obtaining the best objective function value. The F value of 0.8 was therefore chosen as the optimum value for use in this investigation.

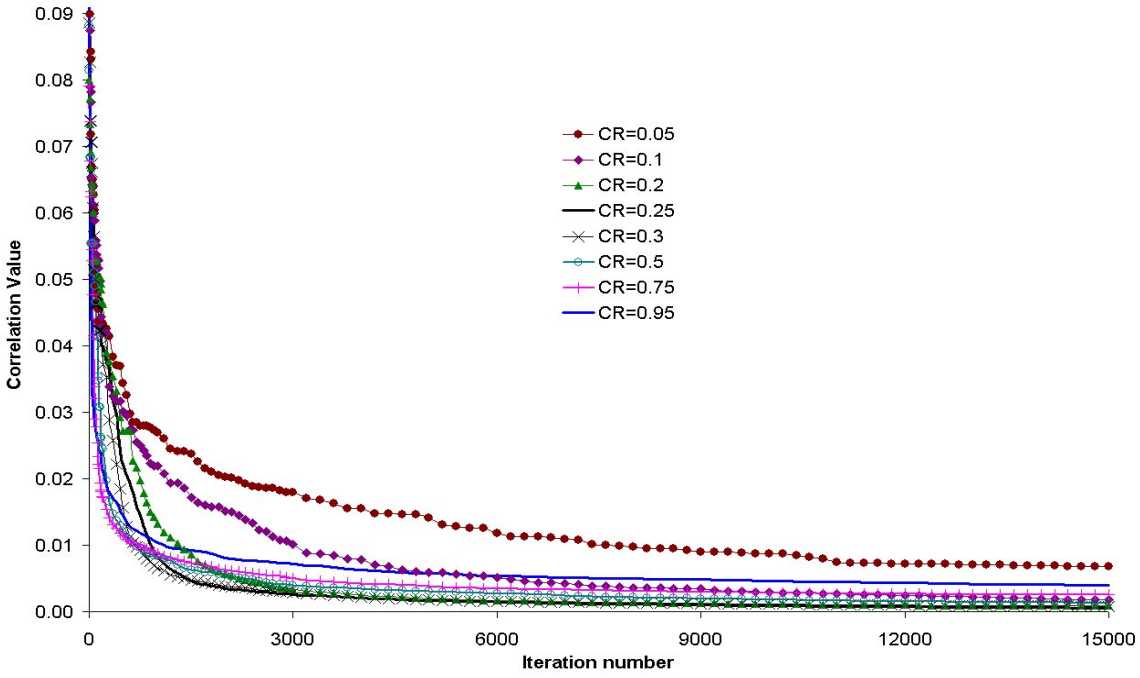

(a)

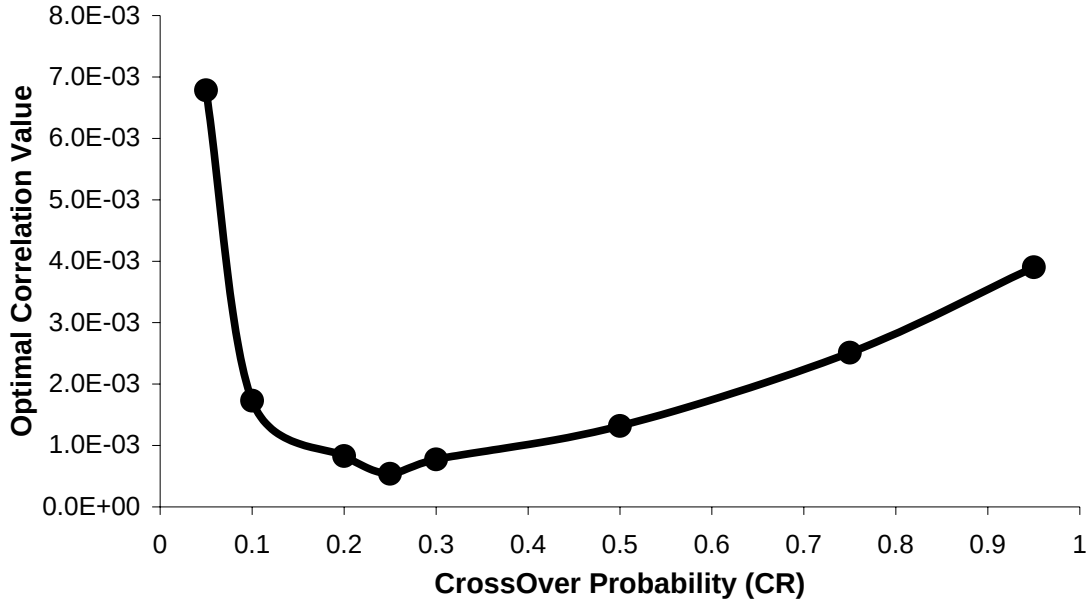

(b)

Figure 6.4: (a) Convergence rates for different crossover CR values (F=0.8) and (b) Optimal correlation function values for different crossover CR values (F=0.8)

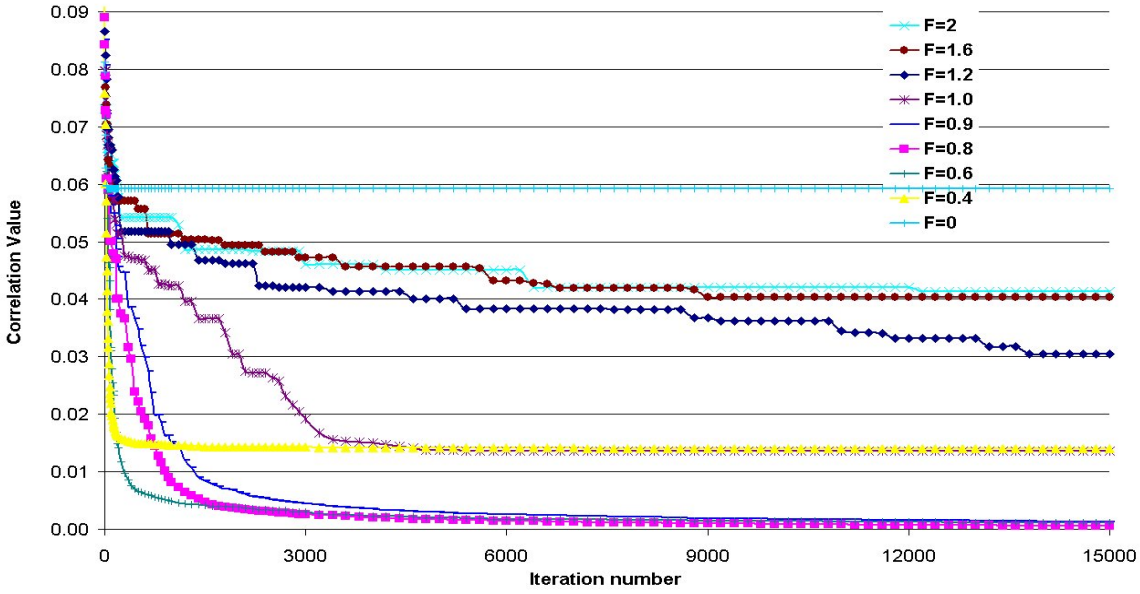

(a)

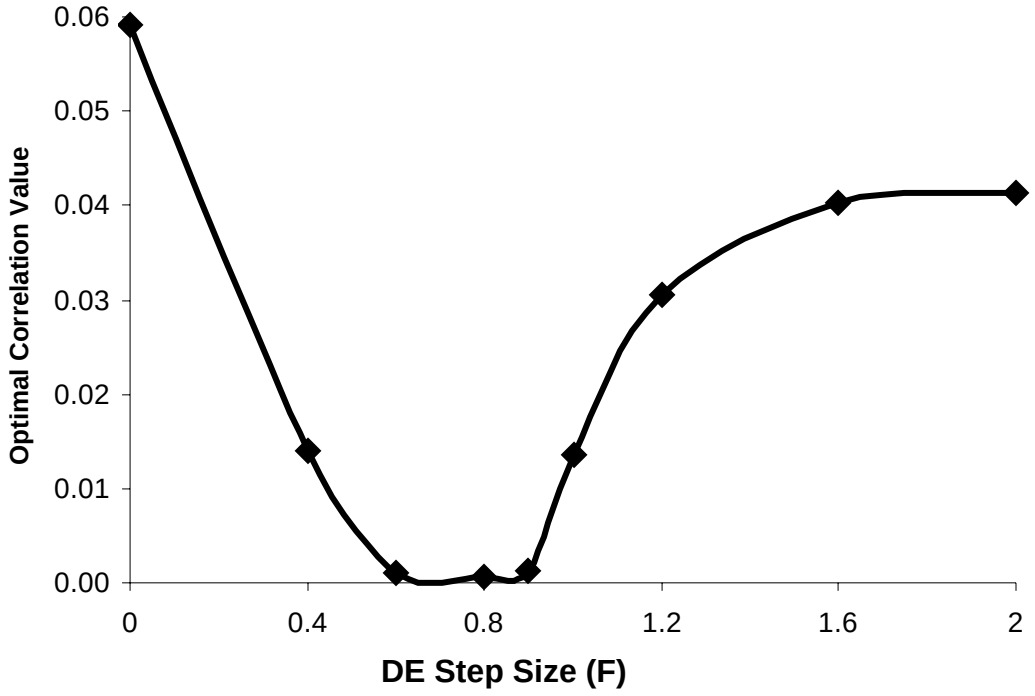

(b)

Figure 6.5: (a) Convergence rates for different DE step sizes F (CR=0.25), (b) Optimal correlation function values for different DE step sizes F (CR=0.25)

6.2.5 Evaluation of Different Types of Constraints for the Pointwise DIC Technique

Since the deformations within a subset are allowed to vary independently, it is possible that the deformation of each pixel will find an optimal value at many different locations within the deformed image, yielding a completely random deformation field with a correlation coefficient of 0. It is therefore imperative to add proper constraints between the deformation variables in order to get physically realistic deformation fields. Six main types of constraints were tested in this work.

(1) The first pixel in the subset was given the chance of moving in the whole image. The next pixel in the first column and first row was then

constrained by maximum one pixel difference in displacement from the first pixel. This was considered as strain of less than 100 percent and there should be no overlay of pixels. The other pixels inside were then constrained from the previous pixels in the same row by maximum one pixel difference for u_1 displacement, and from the previous pixels in the same column by maximum one pixel difference for u_2 displacement. The displacement field is shown in *Figure 6.6.*

(2) From the results shown in *Figure 6.6*, the displacement has big jumps in the unconstrained direction. So, more strict constraints should be applied. The second constraint type was to apply constraints to the pixels in both directions. The first pixel and pixels in the first row and column were constrained as in type 1. The inside pixel (i, j) was constrained in the range of maximum one pixel difference both from $(i-1, j)$ and $(i, j-1)$. The displacement field is shown in *Figure 6.7.*

(3) By applying constraint type 2, the displacement between adjacent pixels was constrained to within one pixel of difference. However, the values for the initial population members were obtained from the conventional DIC technique, Vic2D. Bicubic spline interpolation is used in Vic2D for reconstructing the sub-pixel intensities of the deformed images. So, using the Vic2D values for the initial population members and allowing the displacements to vary by no more than 1 pixel from this initial data. The displacement field obtained using this constraint condition is shown in *Figure 6.8.*

(4) Starting from the displacement data obtained by type 1, allow a maximum of one pixel variation for displacement difference for the adjacent pixels. The objective correlation value is less than that of Vic2D, which used cubic spline interpolation. The displacement result is shown in *Figure 6.9.*

(5) To avoid early likeness of population for obtaining the global minimum, twenty different runs were done separately to get twenty best members for twenty initial populations, using the same constraints and same parameters for GA as in type 1. But the correlation value and displacement field were almost same as in Type 1, which is obtained in one running. Therefore, the likeness of population did not occur to affect the result in our work. The displacement result is shown in *Figure 6.10.*

(6) From the result in constraint type 1 and type 4, the displacement field has large deviation from Vic2D value at the edge. In order to minimize this effect, averaging method was used for adjacent displacement. The same constraint was applied as in type 1. Averaging displacements of adjacent pixels for the corresponding pixel, displacement could be smoothed but the edge is still pulled off. The result is shown as in *Figure 6.11.*

A summary of the descriptions for the above six constraint types can be found in *Table 6.1.* The optimal objective correlation values for each of the constraint type, along with the Vic2D correlation value obtained using bicubic spline interpolation, are listed in *Table 6.2.* A CR of 0.25 and a F of 0.8 were used for each constraint type. From *Table 6.1*, it can be seen that the optimal GA value is for constraint type 4. This value is roughly 2 orders of magnitude better than that determined using Vic2D.

All constraint types except type 2 exhibited better correlation function values, with constraint type 3 being approximately twice the value of constraint type 4. This indicates that the pointwise DIC technique is capable of providing a substantially better fit of the original intensity values to the deformed image.

It is shown that discontinuous and independent displacements can be potentially predicted by the pointwise DIC technique with subpixel accuracy using a pointwise kinematic description of the displacement field instead of the traditional linear or higher-order approximation. Because of the orders of magnitude increase in optimization variables, the GA is used to determine the pointwise displacement fields. From the parametric study of GA, it is shown that the crossover probability (CR) and DE step size (F) significantly affect the convergence rates and optimal correlation function values. Larger CR and F values give faster initial convergence rates. With a fixed mutation rate and constraint condition, the best correlation value can be achieved when CR=0.25. Using the optimal CR value 0.25 and varying F, a F=0.8 gave the best correlation value. From the study of six different constraint types, it was clear that different constraint conditions could affect the displacement field directly. By choosing the proper GA parameters and constraints, the smallest correlation value can be obtained that is up to 2 orders of magnitude less than that from the conventional DIC technique. While the displacement fields were not physically meaningful for a case of constant rotation. This may be due to two possible reasons: (1) The displacement field values may be caused by the inherent experimental errors in the technique. This can be useful in refining the technique through improved speckle patterns and digital imaging hardware to minimize the inherent errors that are

not be revealed in the conventional technique. (2) The correlation function and constraints of displacement for pointwise DIC may need to be further investigated for the kinematic and pointwise description of the displacement field.

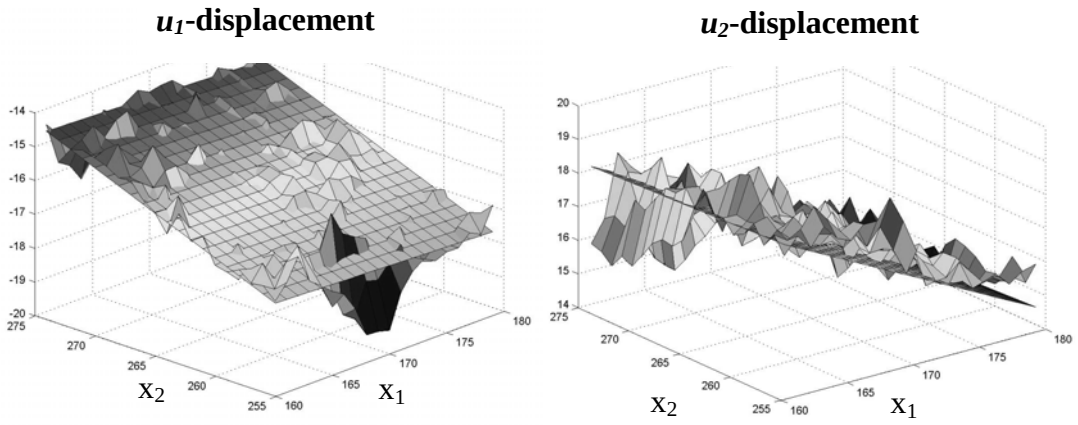

Figure 6.6: u_1 and u_2 displacement fields using constraint type 1. The results from Vic2D are the smooth surfaces.

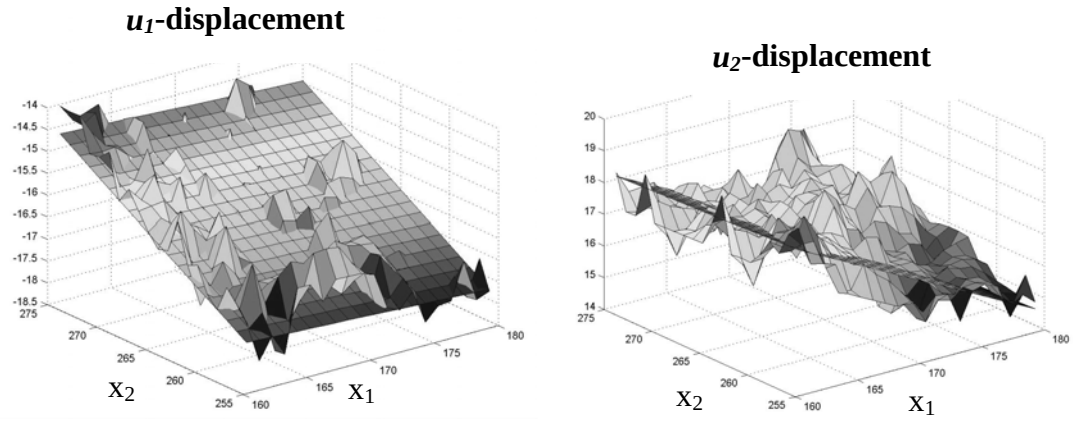

Figure 6.7: u_1 and u_2 displacement fields using constraint type 2.

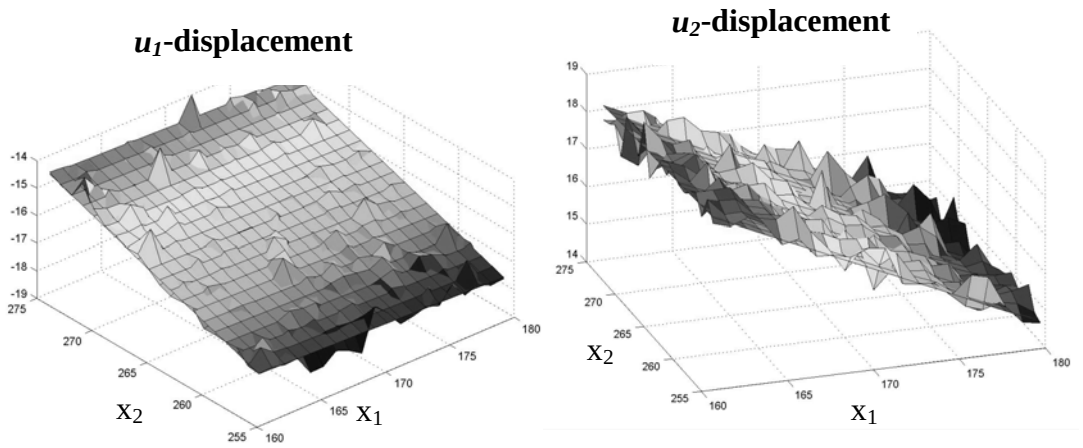

Figure 6.8: u_1 and u_2 displacement fields using constraint type 3

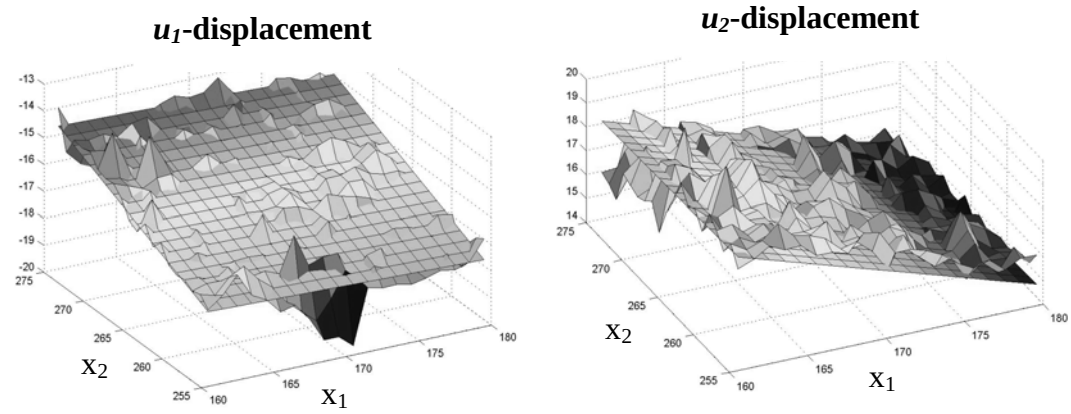

Figure 6.9: u_1 and u_2 displacement field using constraint type 4.

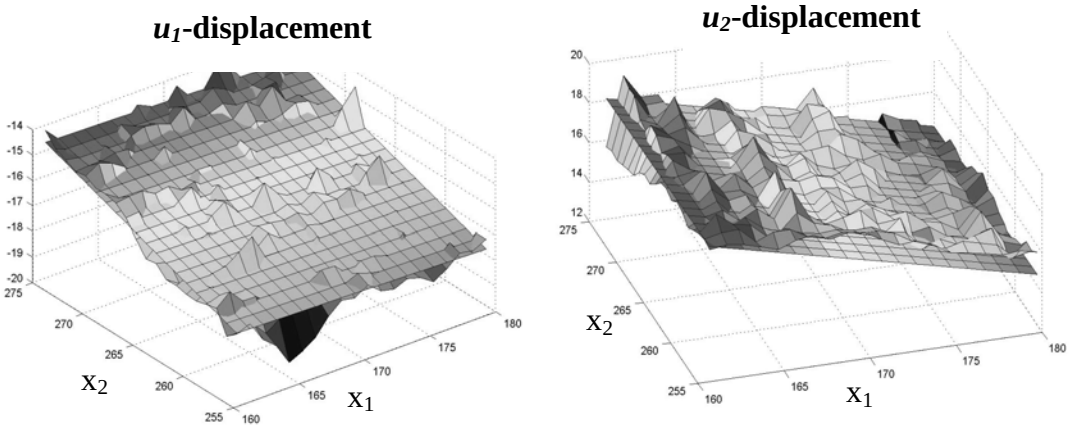

Figure 6.10: u_1 and u_2 displacement field using constraint type 5.

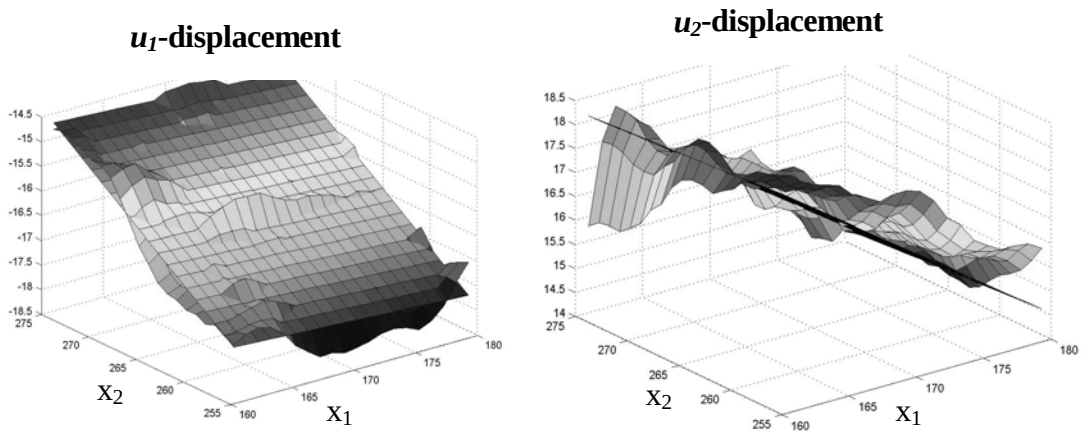

Figure 6.11: u_1 and u_2 displacement field using constraint type 6.

Table 6.1: Descriptionsfor different types of constraints

Costraint Type	Description
1	Constrain $u_1(i, j)$ displacement from pixel $(i, j-1)$ and $u_2(i, j)$ displacement from pixel $(i-1, j)$
2	Constrain both $u_1(i, j)$ and $u_2(i, j)$ displacement from pixel $(i-1, j-1)$
3	Start from the Vic2D displacements and allow one pixel variation in displacement
4	Start from the type 1 displacements and allow one pixel variation in displacement
5	Start from 20 individual best members for initial population and apply constraint type 1
6	Same as constraint type 1, use average of the displacement from the adjacent pixels

Table 6.2: Correlation function value using different type of constraints

Constraint Type	Correlation Value	% Difference with Vic2D
1	0.000538	-82.6%
2	0.00971	213.2%
3	0.0000484	-98.4%
4	0.0000219	-99.3%
5	0.000813	-73.7%
6	0.000713	-76.9%

6.3 Theoretical Development of Pointwise DIC

In section 6.2, pointwise DIC using a Genetic Algorithm (GA) optimization method was presented to experimentally demonstrate that the displacement of each pixel can be determined independently (i.e., *pointwise*) with subpixel accuracy. The effects of GA parameters, crossover probability CR and mutation rate MU on the convergence rate and correlation function values were studied. Also the displacement fields obtained using different constraint conditions were compared. Though the optimal objective correlation function value obtained from pointwise DIC can be two orders of magnitude less than that of conventional DIC, the displacement field obtained from pointwise DIC was not physically meaningful. Therefore, further study was needed to ascertain whether the deviation of displacement field was from the inherent experimental error due to imaging or from the imperfection of the development of the pointwise DIC technique.

In this section, computer-generated ideal sinusoidal images were used to theoretically develop the pointwise DIC technique. Thus, the inherent experimental errors from the real speckle patterns and imaging hardware could be removed from the analysis.

Rigid body translation, extensional strain, and rigid body rotation cases were used to study the accuracy of the displacement fields obtained using pointwise DIC. The objective correlation function was modified through the use of intensity gradients to enhance the accuracy of the pointwise DIC technique. The accuracy of bilinear and bicubic interpolation schemes were investigated for the reconstruction of values for intensity and intensity gradients in the deformed and undeformed images. The Eulerian description of intensity gradients in the deformed images was also transformed in order to correlate with the Lagrangian description of the undeformed images. To demonstrate the advantages of the pointwise DIC technique over conventional DIC, a theoretical displacement field associated with a twin boundary was analyzed using the ideal sinusoidal images. The results were compared with those from commercial available software Vic2D. Experiments were also conducted on a polycarbonate dogbone specimen that validated pointwise DIC on real images and determined the inherent accuracy in the digital image acquisition.

6.3.1 Ideal Sinusoidal Images for Theoretical Analysis

For theoretical analysis, ideal sinusoidal images generated by a computer program have been used to remove experimental errors associated with digital images and evaluate the inherent accuracy of the DIC technique. An ideal sinusoidal image has an intensity, $F(x_\alpha(i, j))$, at absolute coordinate, $x_\alpha(i, j)$, where *(i, j)* is the relative pixel location in the subset, which is defined as follows:

$$F(x_\alpha(i, j)) = (255/2)(1 + \sin(\pi i/\lambda)\sin(\pi j/\lambda)) \tag{6.7}$$

where λ is the period of the sinusoid. The intensity of each pixel will therefore range from 0 (e.g., black) to 255 (e.g., white), which corresponds to a digital image with 8-bit gray levels that would typically be used in the DIC technique. Translated images can be obtained by uniformly translating the original image one-half of a pixel along both the positive x_1-direction and positive x_2-direction. The ideal image for extensional strain can be obtained by stretching the original image 5% in the x_1 direction. A rotated image can be obtained by uniformly rotating the original image clockwise 10^o degree relative to the first pixel. Ideal sinusoidal undeformed and rotated images can be seen in *Figure 6.12.*

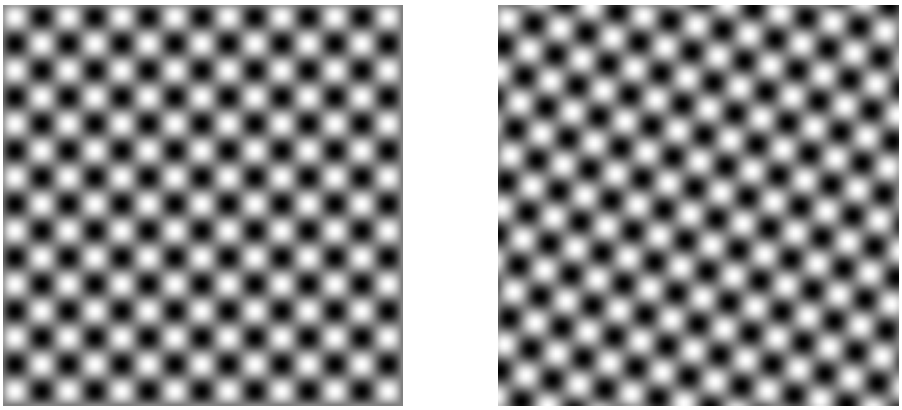

(a) (b)

Figure 6.12: Computer-generated ideal sinusoidal images for pointwise DIC, (a) Undeformed image and (b) Rotated image

6.3.2 Modified Correlation Function

To test the validity of the principles for pointwise DIC, an ideal sinusoidal image was correlated against itself, which should produce no displacement. Bicubic interpolation scheme was used to calculate the intensity values at subpixel locations. For this case, a correlation function value of 1.0e-6 was reached after 650 iterations using the GA method. However, the root-mean-square distance of the u_1-displacement between the calculated displacement field and the ideal displacement field was 0.3080, while the root-mean-square distance for the u_2-displacement was 0.2668. Further evaluation of the individual intensity values indicated that they are not always unique at integer and subpixel locations. For example, position (13, 13) has same intensity as position (13.6383, 12.5555), which is the pointwise DIC calculated subpixel position. Thus, the objective correlation function was modified to include the intensity gradients in order to more uniquely identify each pixel location as follow:

$$S(x_\alpha(i,j),u_\alpha(i,j))=\sum_{i=1}^{N}\sum_{j=1}^{N}\{[F(x_\alpha(i,j))-G(x_\alpha^*(i,j))]^2+[F_{x_1}(x_\alpha(i,j))-G_{x_1}(x_\alpha^*(i,j))]^2 +[F_{x_2}(x_\alpha(i,j))-G_{x_2}(x_\alpha^*(i,j))]^2+[F_{x_1x_2}(x_\alpha(i,j))-G_{x_1x_2}(x_\alpha^*(i,j))]^2\} \quad (6.8)$$

where $F_{x_1}(x_\alpha(i,j))$ and $G_{x_1}(x_\alpha^*(i,j))$ are intensity gradients in the x_1-direction, $F_{x_2}(x_\alpha(i,j))$ and $G_{x_2}(x_\alpha^*(i,j))$ are intensity gradients in the x_2-direction, and $F_{x_1x_2}(x_\alpha(i,j))$ and $G_{x_1x_2}(x_\alpha(i,j))$ are cross-derivatives of the intensity fields. Intensity gradients can be calculated directly from the intensity values of adjacent pixels when using bilinear interpolation scheme, which is formulated in *equation*

(6.5). However, directional derivative is applied on the bicubic interpolation of the intensity values to calculate the intensity gradient when using the bicubic interpolation scheme.

Using the modified correlation function and the bicubic interpolation scheme for the intensity and intensity gradients, the correlation function value reaches 1.0e-6 after 1047 iterations. The root-mean-square distance between the calculated displacement field and the ideal displacement field is 1.2491e-5 for u_1-displacement and 8.5468e-5 for u_2-displacement, which are nearly 4 orders of magnitude smaller than the deviation of the displacement field obtained in the previous case without using the intensity gradients. The pointwise DIC calculated displacement fields with and without intensity gradients are plotted together with the ideal ones in *Figure 6.13.* A summary of the results for correlating an image with itself using the original and modified correlation function is tabulated in *Table 6.3.*

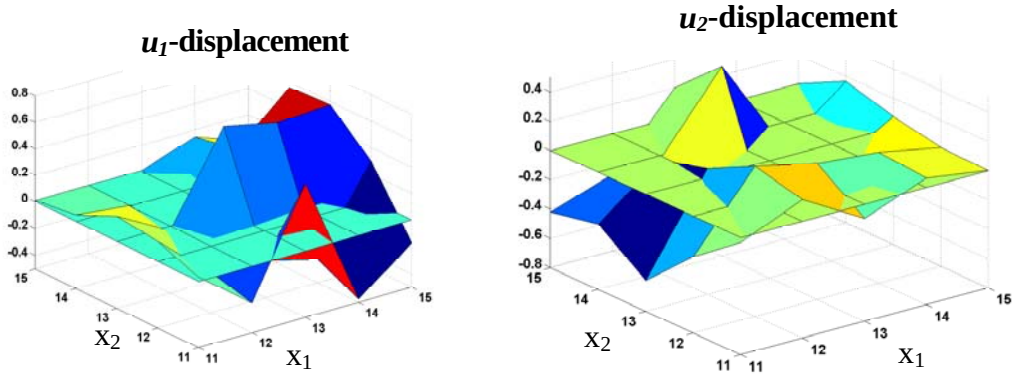

(a)

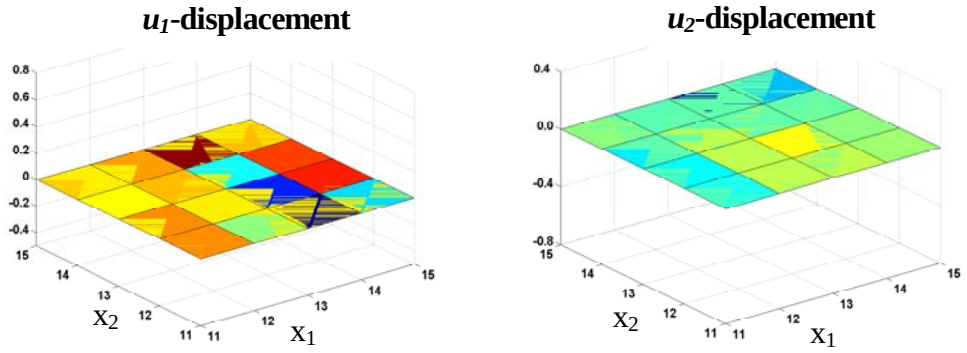

(b)

Figure 6.13: The pointwise DIC calculated displacement together with the ideal displacement, (a) without intensity gradients, (b) with intensity gradients

Table 6.3: The root-mean-square values of the obtained position from the ideal position using bilicubic interpolation and the correlation function without and with intensity gradients

Correlation Function	Iterations to reach correlation value of 1.0e-6	Root Mean Square of u_1-displacement	Root Mean Square of u_2-displacement
Without intensity gradient	650	0.3080	0.2668
With intensity gradient	1047	1.2491e-005	8.5468e-006

6.3.3 Theoretical Analysis of Pointwise DIC Using Ideal Sinusoidal Images

6.3.3.1 Rigid Body Translation

In order to quantify the accuracy of the pointwise DIC technique for the case of rigid body translation, the deformed image was translated from the undeformed image by 0.5 pixel in both the x_1-direction and x_2-direction at every point in the

image. The correlation algorithm is employed between the undeformed image and the translated image, allowing each pixel to displace independently. Using the bilinear interpolation scheme, the optimal correlation value was 43.7343. The root-mean-square distance between the calculated values and the ideal values was 0.0493 for the u_1-displacement and 0.0427 for the u_2-displacement. Some pixel locations had deviations of up to 0.8 pixel from the ideal displacements, which was very poor local accuracy.

Using the bicubic interpolation scheme, an optimal correlation value of 0.01494 was obtained, almost 3 orders of magnitude smaller than for the bilinear scheme. The root-mean-square distance between the calculated values and the ideal values is 8.9145e-4 for u_1- displacement and 8.9146e-4 for u_2-displacement, which was more than two orders of magnitude smaller than for the bilinear scheme. The displacement fields obtained using both the bilinear interpolation scheme and the bicubic interpolation scheme are shown in *Figure 6.14*. From this figure, it can be seen that the local variations in the bilinear interpolation scheme are not present in the bicubic case, resulting in a far more accurate displacement resolution than indicated by the difference in standard deviation.

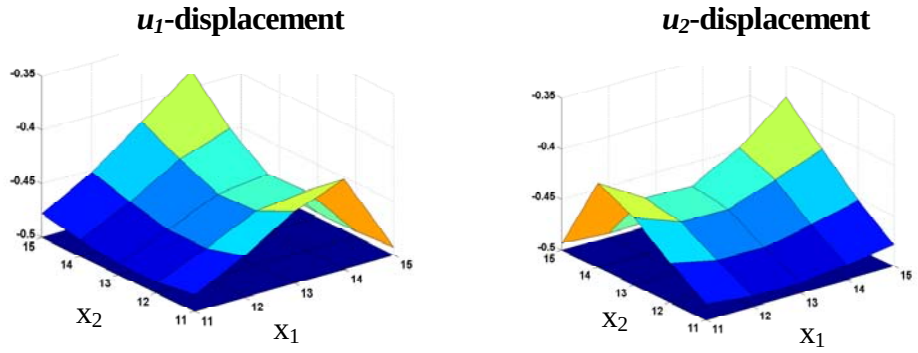

(a)

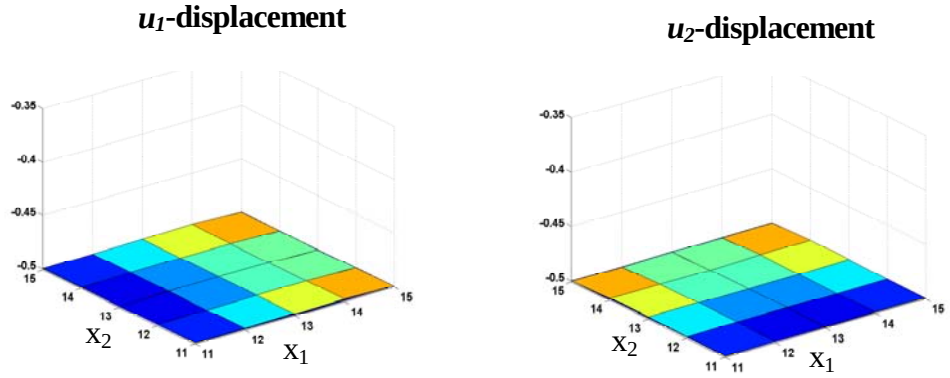

(b)

Figure 6.14: The pointwise DIC calculated displacement together with the ideal displacement for rigid body translation case, (a) Bilinear interpolation scheme, (b) Bicubic interpolation scheme

6.3.3.2 Extensional Strain

The case of rigid body translation provides a good indication of the general accuracy of the pointwise DIC technique. However, in actual applications the technique will be used to determine deformations on the surfaces of objects undergoing strain. Therefore, the accuracy of the technique for measuring strains was

analyzed by applying a 5% extensional strain to the undeformed image in the x_1-direction while keeping x_2-direction constant.

It is important to note that the intensity gradients in the deformed image are calculated relative to the pixel positions in the deformed image (i.e., Eulerian reference frame, x_α*). This will alter the values of the intensity gradients from their values in the undeformed image. Therefore, it is necessary to calculate the intensity gradients relative to the undeformed pixel locations (i.e., Lagrangian reference frame, x_α), by transforming from the Eulerian to the Lagrangian frame. This transformation can be expressed mathematically as follows:

$$\frac{\partial(.)}{\partial x_\alpha} = \frac{\partial(.)}{\partial x_\beta *}\frac{\partial x_\beta *}{\partial x_\alpha} = \frac{\partial(.)}{\partial x_\beta *}(\delta_{\beta\alpha} + u_{\beta,\alpha}) \qquad (6.9)$$

However, because the displacements at each pixel are not known, the displacement gradients are also not known. Therefore, they must either be additional optimization variables solved for using the GA method or directly calculated from the displacement field. In the case of extensional strain, rather than solving for all of the displacement gradients, only the $u_{1,1}$ displacement gradient was chosen as an additional optimization variable, and it was assumed constant over the entire field in order to maximize the convergence of the GA method.

Using the bilinear interpolation scheme, the correlation function reached an optimal value of 23.9046. The root-mean-square distance between the obtained values and the ideal values was 0.0353 for the u_1-displacement and 0.0439 for the u_2-displacement. The bicubic interpolation case reached an optimal correlation function

value of 0.001221. The root-mean-square distance between the correlated displacements and the theoretical displacements was 8.1058e-4 for the u_1-displacement and 2.8034e-5 for the u_2-displacement. The displacement fields obtained using bilinear interpolation scheme and bicubic interpolation scheme are shown in *Figure 6.15*.

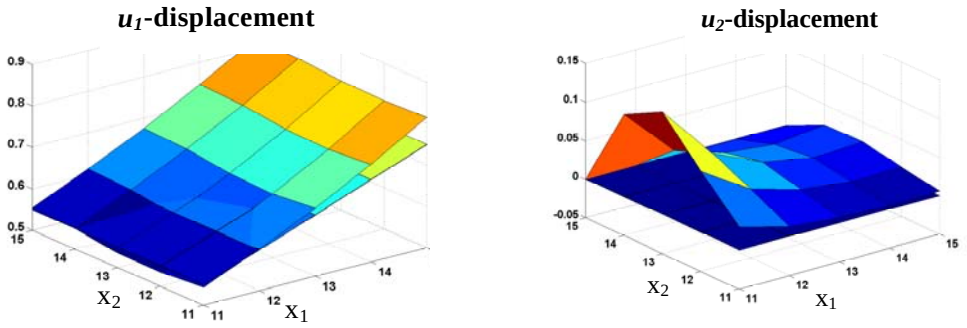

(a)

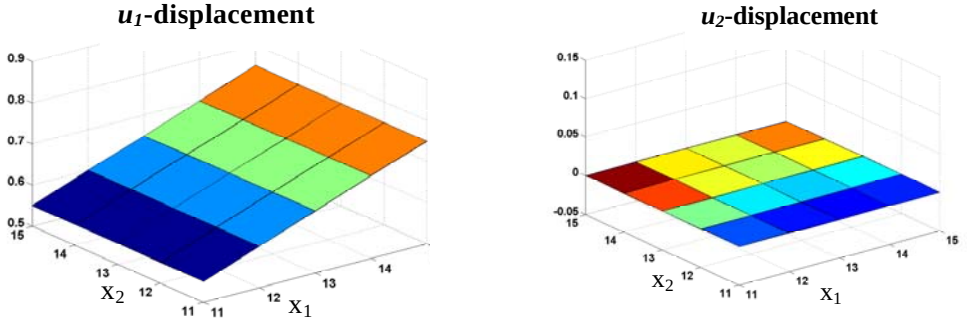

(b)

Figure 6.15: The pointwise DIC calculated displacement together with the ideal displacement for extensional strain case, (a) Bilinear interpolation scheme, (b) Bicubic interpolation scheme

6.3.3.3 Rigid Body Rotation

To completely test the effects of the displacement gradients on the gradient transformation in *equation (6.8),* the case of rigid body rotation can be analyzed. For the case of a rigid body rotation, a rotation angle, θ , is applied uniformly to every point in the image. The resulting displacement field is as follows:

$$\begin{aligned} u_1 &= x_1 \cos\theta + x_2 \sin\theta \\ u_2 &= x_1 \sin\theta + x_2 \cos\theta \end{aligned} \tag{6.10}$$

As can be seen from *equation (6.9),* all four of the displacement gradients in the correlation function *equation (6.8)* will be nonzero for the case of rigid body rotation. In this investigation, the deformed image was obtained by applying a 10^o rotation clockwise to the undeformed image. As with the case of extensional strain, the variables to be optimized in the DIC algorithm have been fundamentally changed from determining the two displacements u_i, to determining the 6 deformation parameters, u_i and $u_{i,j}$, at every point in a subset. For infinitesimal deformations, it is important to note that the displacement gradients will be related to the rotation angle, θ , as follows,

$$\theta = \frac{1}{2}\left(u_{1,2} - u_{2,1}\right) \tag{6.11}$$

As with the case of extensional strain, rather than using all of the displacement gradients as optimization variables, only the rotation angle itself was chosen as an

optimization variable that was assumed constant over the entire field in order to maximize the convergence rate for the GA method.

Using the bilinear interpolation scheme, an optimal correlation value of 26.1069 was reached. The root-mean-square distance between the obtained values and the ideal values was 0.1393 for the u_1-displacement and 0.1154 for the u_2-displacement. The bicubic interpolation scheme can be used to obtain an optimal correlation value of 0.007276. The root-mean-square distance between the obtained displacement and the ideal value was 0.0041 for the u_1-displacement and 0.0039 for the u_2-displacement. A summary of the results using the bilinear and bicubic interpolation scheme is listed in *Table 6.4*. It is shown that bicubic interpolation schemes can reach the correlation function value which is more than 3 orders of magnitude smaller than that for bilinear interpolation. The displacement field using bicubic interpolation matches with ideal ones about 2 orders of magnitude better than that for bilinear interpolation. The displacement fields obtained using bilinear interpolation scheme and bicubic interpolation scheme are shown in *Figure 6.16*.

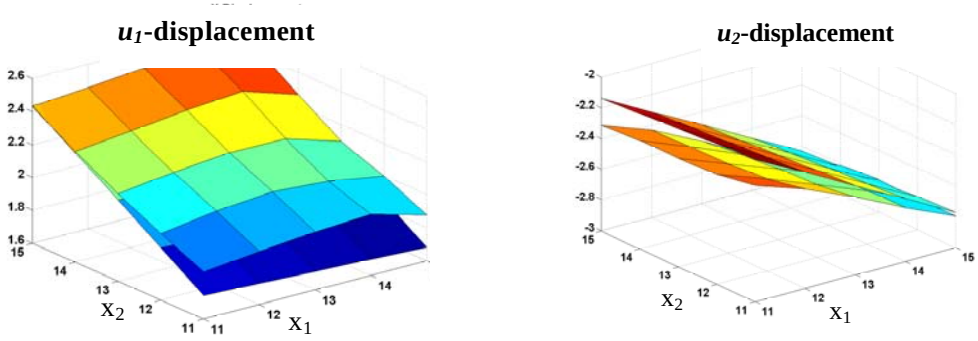

(a)

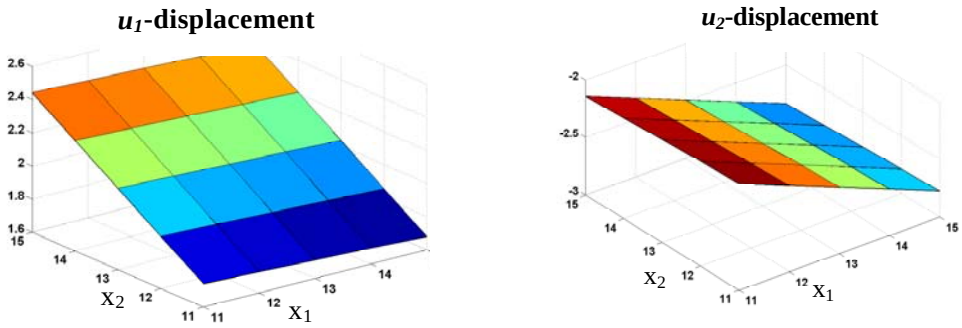

(b)

Figure 6.16: The pointwise DIC calculated displacement together with the ideal displacement for rigid body rotation case, (a) Bilinear interpolation scheme, (b) Bicubic interpolation scheme

Table 6.4: Ultimate correlation value and standard deviation comparison for bilinear and bicubic interpolation scheme

Correlation Case	Interpolation Scheme	Optimal Correlation Function Value	Root Mean Square of u_1-displacement	Root Mean Square of u_2-displacement
Rigid Body Translation	Bilinear	43.7343	0.0493	0.0427
	Bicubic	0.01494	8.9145e-4	8.9146e-4
Extensional Strain	Bilinear	23.9046	0.0353	0.0439
	Bicubic	0.001221	8.1058e-4	2.8034e-4
Rigid Body Rotation	Bilinear	26.1069	0.1393	0.01154
	Bicubic	0.007276	0.0041	0.0039

6.3.3.4 Comparison of Bilinear and Bicubic Interpolation Error

For the above three cases of rigid body translation, extension and rotation, the bicubic interpolation scheme gives better result for displacement field and correlation function value than bilinear interpolation scheme. As discussed in the previous section, the correlation function for pointwise DIC was modified to include both the intensity and intensity gradients. Therefore, the interpolation error of the intensity and

the intensity gradients using bicubic and bilinear interpolation schemes are compared, which will explain the large difference in the correlation function value. In this interpolation error study, ideal sinusoidal image defined by *equation (6.7)* was used. An area of 5x5 pixel with the first pixel located at (11,11) was chosen as the reference. This reference image was then translated in both x and y direction by an incremental step of 1/10 pixel. The intensity and intensity gradients were then calculated for these subpixel positions using bilinear and bicubic interpolation scheme. *Figure 6.17(a)* and *(b)* show the root-mean-square of the bilinear and bicubic interpolation scheme errors for the intensity, intensity gradients and intensity cross gradients. Bilinear interpolation scheme shows error as large as 1.4 for intensity gradient, while bicubic interpolation scheme has all the errors less than 1.0e-2. This shows that bicubic interpolation is at least 2 orders more accurate than bilinear interpolation scheme. This also explains the much smaller correlation function value of bicubic interpolation than bilinear interpolation scheme.

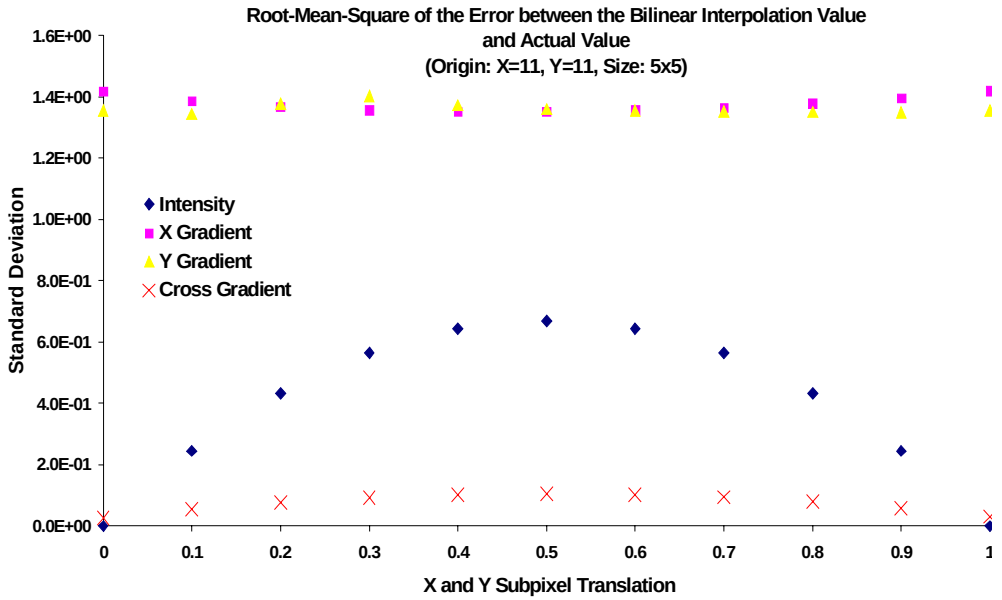

(a)

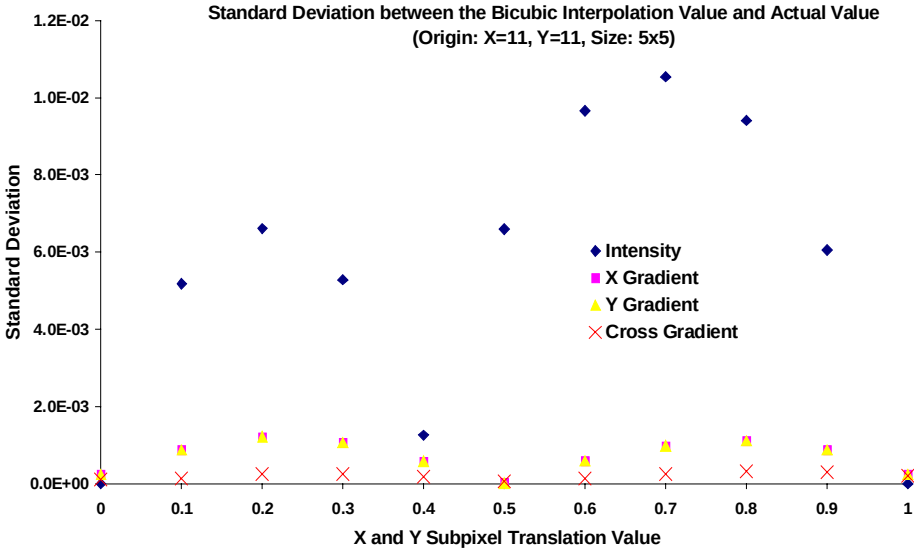

(b)

Figure 6.17: Root-Mean-Square of the interpolation error of the intensity and intensity gradient for different x-y subpixel translation value (a) bilinear interpolation scheme error (b) bicubic interpolation scheme error

6.3.3.5 Correlation Analysis for the Twinning Deformation

After pointwise DIC has been theoretically evaluated for rigid body translation, rotation and extension cases, it was applied on the twinning deformation case to compare the displacement fields with which were obtained from commercially available software Vic2D. Ideal sinusoidal images were generated to simulate the twinning deformation. The intensity of pixel location (i, j) is defined same as in *equation (6.7).* The bottom half plane displaces 1/6<111> relative to the top half plane. The twinned image is shown together with the undeformed image in *Figure 6.18.*

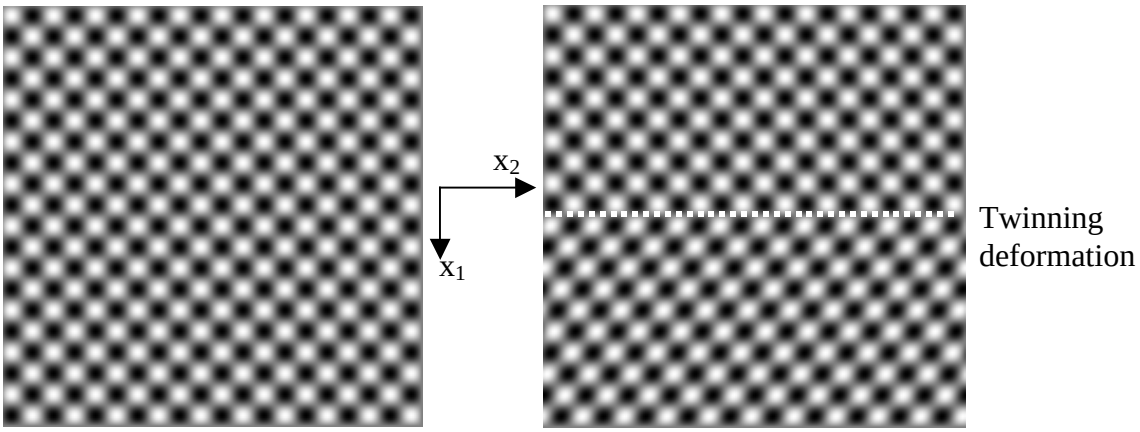

(a) Undeformed image (b) Twinned deformation image

Figure 6.18: Computer-generated ideal sinusoidal images for twinning deformation case (a) Undeformed image, and (b) Twinned image. The lower half below the twin interface undergoes a 1/6<111> twinning deformation (i.e., $\frac{\partial u_2}{\partial x_1} = -0.167$)

A 5-pixel by 5-pixel correlation area cross the twinning plane was chosen to correlate between the undeformed image and the twinned image, which would be a

good case to test the eligibility of pointwise DIC at the deformation interface. Bicubic interpolation scheme and the modified correlation function with intensity were used in the pointwise DIC. In this case, the optimal correlation value can reach 0.1458. The root-mean-square distance between the obtained displacement and the ideal value is 0.0026 for the u_1-displacement and 0.0228 for the u_2-displacement for the pointwise DIC results. Using the commercially software Vic2D, the displacement field shows larger deviation from the actual values. The root-mean-square distance between the obtained displacement and the ideal value is 0.0088 for the u_1-displacement and 0.2576 for the u_2-displacement for the Vic2D results. The displacement fields obtained using pointwise DIC and Vic2D software are shown in *Figure 6.19* together with the ideal values. The deviation of the pointwise DIC and the Vic2D calculated results from the ideal values are shown together in *Figure 6.20*. It shows that the deviation for the u_2-displacement of Vic2D is more than 10 times larger than that of pointwise DIC, and the deviation for u_1-displacement of Vic2D is 3 times of that of pointwise DIC.

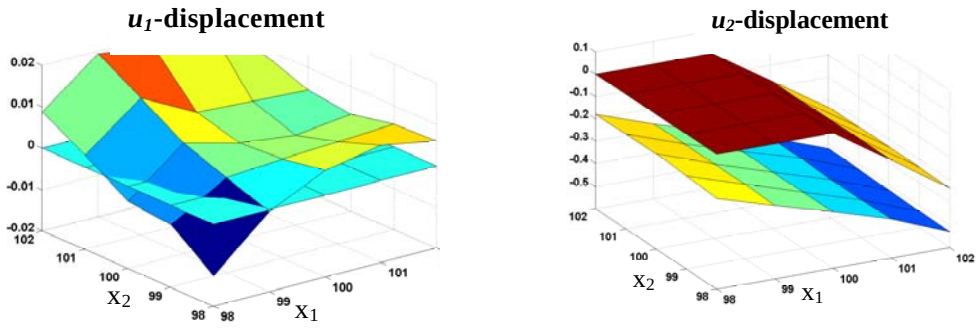

(a)

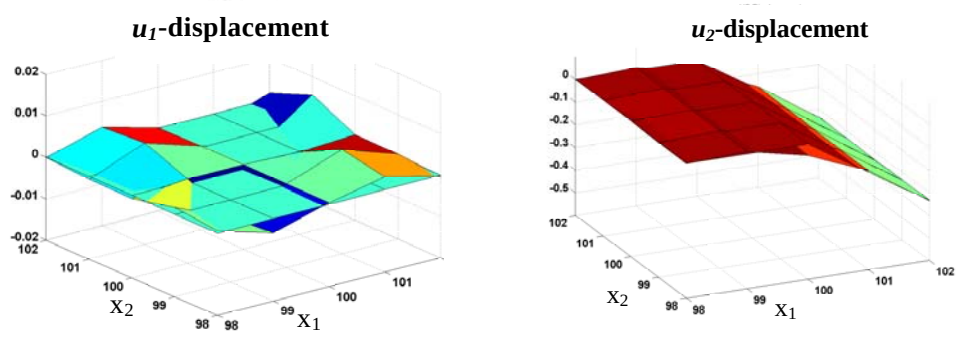

(b)

Figure 6.19: The calculated displacement together with the ideal displacement cross the twinning plane (a) Displacement field from Vic2D, (b) Displacement field from pointwise DIC

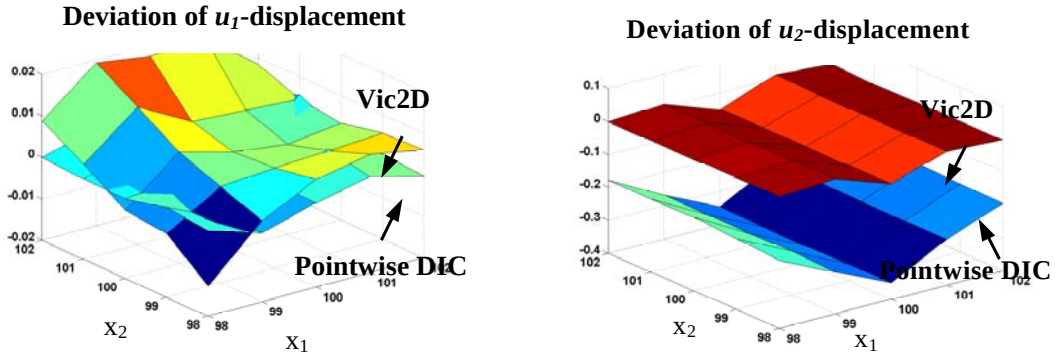

Figure 6.20: The deviation of displacement field of Vic2D and pointwise DIC from the ideal values

6.3.3.6 Pointwise DIC using Real Images Obtained from Experiments

To verify the validity of pointwise DIC on real images, a polycarbonate specimen with an ASTM D638 dogbone geometry was subjected to rigid body translation, extensional strain, and rigid body rotation. Digital images were obtained

using a Q-imaging Retiga 1300 digital camera with 8 bit gray level resolution and a 1280x1024 pixel spatial resolution. A 105 mm Nikon Micro-Nikkor lens was used to image at a magnification of 1mm/59 pixels. A fiber optic ring light was used to illuminate the specimen in order to obtain uniform light intensity. To reduce the level of noise in the deformed and undeformed images, 20 consecutive images were obtained of each and averaged.

The speckle pattern that was imaged can be seen in *Figure 6.21*. The specimen was translated 10 microns in the u_1-direction and 5 microns in the u_2-direction on an x-y translation stage with an accuracy of 1 micron for the rigid body translation test. For the extensional strain test, strain was measured using an extensometer until a 5% extensional strain was obtained. The absolute accuracy of the extensometer is difficult to determine due to alignment and slip issues, but from experience an accuracy of approximately 0.1% is considered reasonable. In the final rigid body rotation test, the specimen was rotated on a rotation stage with an accuracy of 0.1 degree.

Images were correlated using bicubic spline interpolation and 5x5 pixel areas of interest, as for the theoretical analyses conducted on ideal images. The u_1- and u_2-displacement results for each case can be seen in *Figure 6.22*, along with a least-squares fit of a bilinear plane to the results. Root-mean-square deviation of the displacement relative to the ideal value for each case can be seen in *Table 6.5* along with the values of translation, strain, and rotation that were obtained from the least-square fits. The expected values for the translation results were 0.590 pixels for the u_1-displacement and 0.295 pixels for the u_2-displacement, while the correlated values

were 0.634 and 0.256 pixels respectively. These are within the 0.059 pixel accuracy of the x-y translation stage. The root-mean-square deviations for both displacement fields were 0.029 pixels, and were approximately 3 times higher than for the ideal images. This increase in the root-mean-square deviation was also observed for the extensional strain case where the result of 0.0110 pixels were 14 times higher for the u_1-displacement field, and the result of 0.0111 pixels were nearly 50 times higher for the u_2-displacement field. However, all of the root-mean-square deviations were significantly less than the theoretical bilinear results for the ideal images. The extensional strain was determined to be 4.87%, which was within the range of expected accuracy for the extensometer measurement. For the rigid body rotation case, the root-mean-square deviations were approximately one-half that for the theoretical bilinear results obtained for the ideal images and 20 times the theoretical bicubic results, being 0.0733 and 0.0714 pixels for the u_1-displacment field and u_2-displacement field respectively. The rotation value was 0.1855 radians, which was within the 0.1 degree accuracy for the rotation stage.

Since the values of translation, strain, and rotation were within the range of accuracy for the expected values, the pointwise DIC technique was validated using real images. However, the root-mean-square deviations for all of these cases were much greater than for the ideal images. This is not unexpected, since these results are indicative of the experimental errors inherent to the acquisition of digital images. One source of error is attributed to the accuracy of the digital imaging system (i.e., noise), which uses a Q-imaging Retiga digital camera, considered one of the most accurate digital cameras on the market. Another source of error can be introduced from non-

uniform illumination of the speckle surface, which necessitated the use of a fiber optic ring light. While efforts were made to minimize these errors, there is still the possibility that they can contribute to the observed increases in the root-mean-square deviations. Finally, spherical aberrations from the lens can also contribute to errors, but were minimized by stopping down the lens to increase the depth of field.

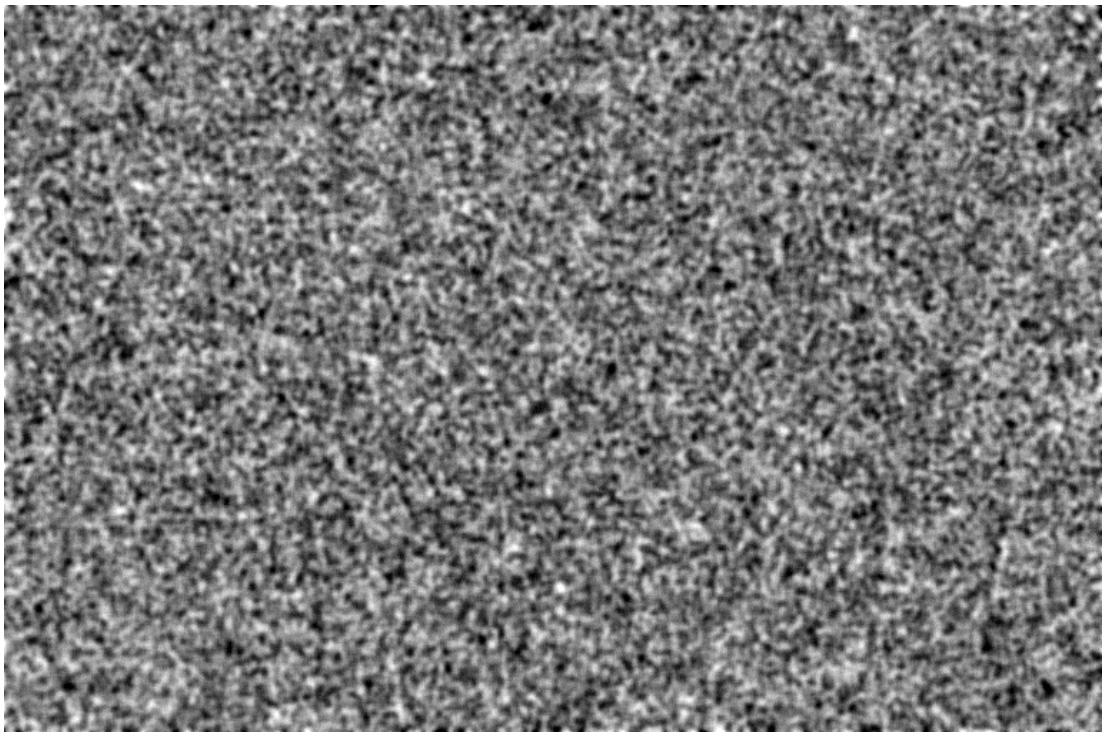

Figure 6.21: Real digital speckle image obtained from Q-imaging Retiga 1300 digital camera

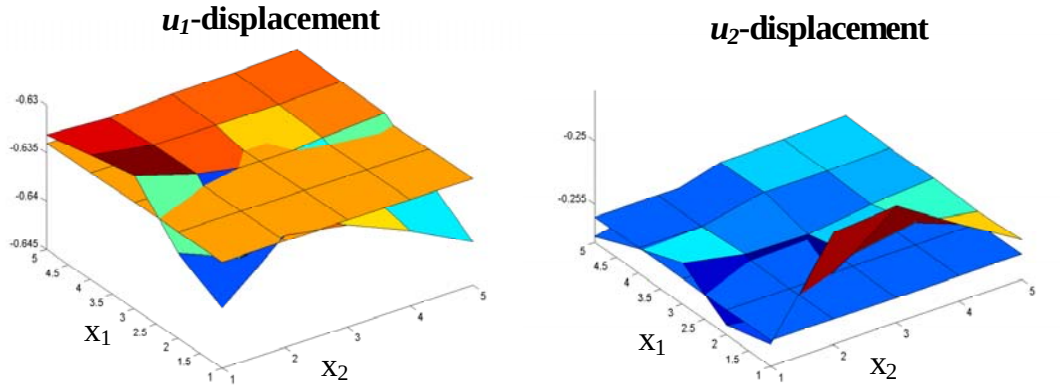

(a)

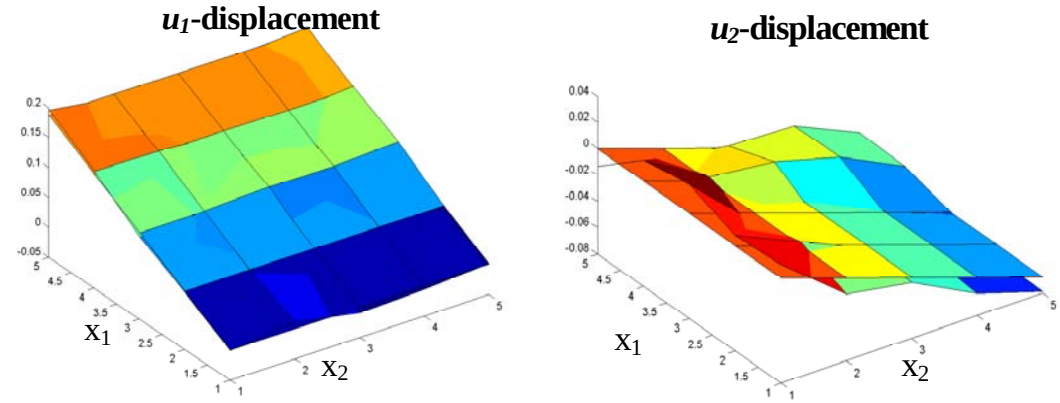

(b)

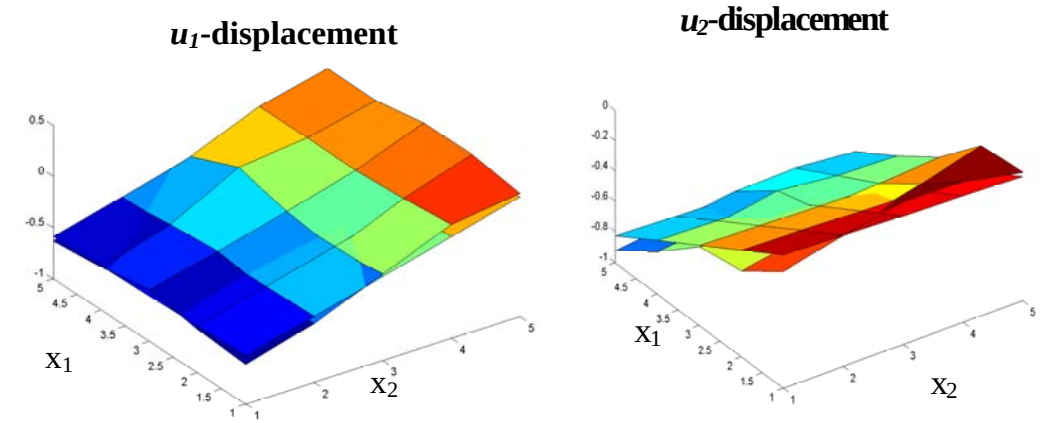

(c)

Figure 6.22: The displacement fields (in *pixels*) correlated from real images subjected to (a) rigid body translation, (b) 5% extensional strain in x_1-direction, and (c) 10^o rigid body rotation, along with the least squares fit of a bilinear plane to the results.

Table 6.5: Pointwise DIC results using real images for rigid body translation, extensional strain, and rigid body rotation cases

Correlation Case	Values from least squares fit	Root Mean Square of u_1-displacement	Root Mean Square of u_2-displacement
Rigid Body Translation	u_1-disp: 0.634 u_2-disp: 0.256	0.0029	0.0029
Extensional Strain	4.87%	0.0108	0.0111
Rigid Body Rotation	0.1855 radians	0.0733	0.0714

6.4 Summary

The conventional DIC employs subset-based correlation algorithm. It cannot accurately determine the displacement field when the displacements are varying rapidly or discontinuous, such as near a crack or interface. Thus, the pointwise DIC technique was developed to provide independent and discontinuous description of displacement fields. A GA optimization algorithm with a Differential Evolution method was employed to optimize the correlation function for the large number of variables associated with the pointwise DIC technique. The effects of the GA parameters on the correlation function value and the convergence rate were studied. A theoretical analysis of the pointwise DIC was undertaken using ideal sinusoidal images. This analysis has indicated that displacements can be measured independently at each pixel within a subset with sub-pixel accuracy. However, due to the lack of uniqueness of the sub-pixel intensity values, the correlation function must be modified to include the intensity gradients instead of just intensity values in order to improve the accuracy. When calculating the intensity gradients for a strained or rotated image, they must be transformed from an Eulerian reference frame to a

Lagrangian reference frame. Thus, the gradients for the deformed image need to be transformed using the displacement gradients at each pixel in a subset, which adds 4 additional variables for each pixel that need to be optimized in the pointwise DIC technique.

Bilinear interpolation schemes have been very popular for DIC because of their computational efficiency with reasonable accuracy for reconstructing images and determining deformations. However, for the pointwise DIC technique the bicubic interpolation scheme can achieve optimal correlation values that are three or four orders of magnitude smaller than that for the bilinear interpolation scheme. The resulting root-mean-square differences between the optimal displacements determined using bicubic interpolation and the actual displacements are two orders of magnitude less than that for the bilinear interpolation scheme. These results were consistently obtained for three different deformation cases: (1) *rigid body translation*, (2) *extensional strain*, and (3) *rigid body rotation*. Thus, it was demonstrated theoretically that pointwise DIC can accurately determine deformation fields using the bicubic interpolation scheme with the modified correlation function, and that deformation effects on the intensity gradients could be accurately accounted for in the modified correlation function.

To demonstrate the advantages of pointwise DIC over the conventional DIC technique, a classical twinning deformation was simulated using the ideal sinusoidal images. The results of pointwise DIC indicate that it can accurately correlate discontinuous deformations across the twin interface, however there is slightly greater error in resolving the discontinuity in displacement gradients across the interface. The

displacement field obtained using pointwise DIC had a deviation from the ideal values that was up to two orders of magnitude better than the conventional DIC technique everywhere but at the twin interface itself, where the deviation was only one order of magnitude better.

The pointwise DIC technique was also validated using real images from a specimen subjected to rigid body translation, extensional strain, and rigid body rotation. Correlation results were obtained using bicubic spline interpolation, and indicated that the values of translation, strain, and rotation were within expected accuracies. However, the standard deviation was up to 50 times greater than for the theoretical results obtained for bicubic spline interpolation, but significantly less than for the theoretical results for bilinear interpolation. These results can be used as an indication of the inherent accuracy in the digital image acquisition system.

7 Contributions and Future Work

7.1 Scientific and Technical Contributions

The main scientific and technical contributions of this work can be summarized as follows:

1. A control system and integrated imaging capability at the microscale and nanoscale have been developed for a new biaxial microtensile tester.

(a) Development of the control of biaxial loading state that provides an experimental method for determining the mechanical behavior under a 2-D stress state.

(b) An optical microscope and objective AFM have been integrated into the tensile testing system to obtain *in situ* digital images with up to one million pixels of resolution of microstructural features over the scanning area, which can range from hundreds of nanometers to tens of microns.

(c) Digital images of a deforming biaxial vinyl film test specimen with a hole at its center was correlated using the DIC technique to verify the biaxial loading state with microscale spatial resolution and sub-micron displacement resolution.

(d) Topographic images of a deforming sputtered nanoscrystalline copper film obtained with the objective AFM were converted into gray scale images with intensity of each pixel in the gray scale corresponding to the topographic data in the image.

(e) Microtensile test results at the microscale were consistent with FEA and theoretical results, although the effect of finite geometry manifested through the shear strain distribution was better predicted by FEA.

(f) The DIC technique was applied to the converted gray scale images to obtain heterogeneous displacement fields at the nanoscale with sub-nanometer displacement resolution.

2. The DIC technique has been used to characterize the spatial nonlinearity in AFM imaging without a specialized micromachined calibration grating.

(a) AFM topographic images with different probe offset values were obtained from sputtered nanocrystalline NiTi films.

(b) The DIC technique was applied to the converted gray scale images from these topographic images to calculate the displacement variation and apparent strain induced by the nonlinearity when measuring displacement fields at the nanoscale.

(c) The nonlinearity calibrated using the DIC technique was verified through comparison with calibration results from the conventional method using the standard calibration grating and SPIP software.

(d) The DIC technique provides nonlinearity calibration at various length scales without the restriction of using a specialized micromachined calibration grating.

3. Pointwise DIC technique has been developed to measure discontinuous displacement fields.

(a) The constraint of constant displacement gradient in the subset is removed from the displacement field, providing independent and discontinuous description of the displacement field.

(b) The GA optimization algorithm with a DE method has been applied to determine the minimum correlation function value for a potentially large number of displacement variables.

(c) The effects of GA parameters over the convergence rate and the optimal correlation function value have been investigated.

(d) The correlation function for pointwise DIC was modified to include the intensity gradients to uniquely determine pixel locations.

(e) Ideal sinusoidal images with rigid body translation, extensional strain, and rigid body rotation cases were used to study the accuracy of the displacement fields obtained using pointwise DIC.

(f) An ideal image associated with a twin boundary is analyzed to demonstrate the advantages of pointwise DIC over the conventional DIC technique for measuring discontinuous displacement fields.

(g) Pointwise DIC was validated using real speckle images obtained from a polycarbonate specimen subjected to rigid body translation, extensional strain, and rigid body rotation.

7.2 Proposed Future Work

The future work proposed for the biaxial microtensile testing system and pointwise DIC are as follows:

1. Develop a closed-loop control program for the picomotor by including the actual motion of the picomotor versus the specified motion of the motor as feedback into the control program.
2. Conduct biaxial microtensile testing on MEMS structures and thin films using the objective AFM for deformation measurements at the nanoscale.
3. Compare the deformation mechanisms of the nanostructured materials and MEMS structures determined from the biaxial microtensile tests with current theoretical and computational models.
4. Characterize the mechanical properties of free standing thin films using the microscopic hole method for biaxial stress states.
5. Develop a faster approach to optimizing the modified correlation function in pointwise DIC with a user-friendly GUI so that it can obtain displacement fields for a large number of displacement variables more quickly and easily.

8 Appendices

8.1 DME DualScope Scanning Probe Microscope Standard Operating Procedure

AFM probe and the focus of laser beam:

AFM probes are micromachined from silicon materials with high resolution. The typical cantilever probe drawing is shown in *Figure 8.1.* The laser beam is focusing on the center of the backside of cantilever as shown in *Figure 8.2.* The intensity of the laser beam reflected from the cantilever can be detected by sensor when the cantilever probe is tapping on the specimen surface.Generally, the AFM probe is mounted to a chip which is attached to the AFM scanner head. The schematic drawing for the setup of AFM probe is shown in *Figure 8.3(a).* In our dualscope AFM, the cantilever probe is mounted to the disk using super glue or silver paste. *Figure 8.3(b)* shows a real setup of the cantilever probe before the disk is attached to the AFM scanner head.

Figure 8.1: An AFM probe includes a cantilever with a sharp probe tip

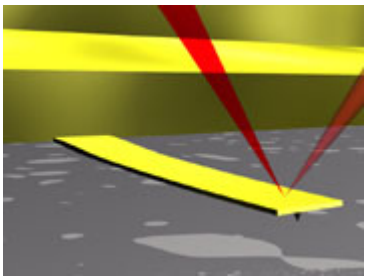

Figure 8.2: Laser beam focusing on cantilever

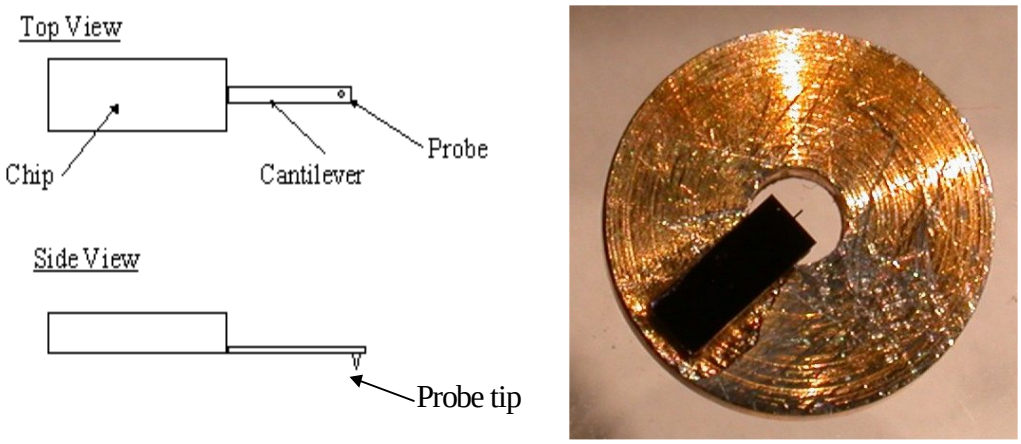

(a) (b)

Figure 8.3: The setup of an AFM cantilever probe, (a) The schematic view of the setup of AFM cantilever probe, (b) The actual mounting disk and cantilever probe in the dualscope AFM

Operating procedures:

I. Turning System On

1. Boot up microscope-dedicated computer.
2. Turn on power of DualScope controller (Red round button on front panel).
3. Start DualScope program on computer (desktop shortcut SPM.EXE or E:\DME\SPM\SPM.EXE). A window with text "Reset the controller?" will popped out. Click "No" for normal cases.

II. Positioning Sample

1. Select "Utilities" in the main menu.
2. Select "Change sample" in "Utilities" submenu. Screen will show "Move sensor to parked position", click "Next" button;
3. Screen will show "Move scan head away from the sample", click "Next".
4. Screen shows "Exchange sample", proceed to change sample with caution, Place sample on stage with side to be imaged facing with the AFM scanner head. Turn on microscope light and, with AFM objective in place, *very carefully* focus microscope so that sample comes into focus; Turn off microscope light, then click "Next".
5. Screen will show "Move scan head back to measuring position", click "Next". Finally, screen will show "The wizard is complete", click "Finish" button.

III. AFM adjustment: (Refer to Help for Utility Menu for more details)

1. While still in Utilities menu, select "AFM adjust." Screen will show "Move sensor away to standby distance," click "Next".
2. The "Frequency sweep" window shows up, where you can input some typical parameters: Selected Q-Factor: 700, Frequency offset: 0, Amplitude Setpoint: 1.5. Phase shift: 0. Check "Automatic sweep" and click "Sweep" button so the frequency will sweep over the whole range. A red and a blue curve should move around until the working amplitude is set to amplitude setpoint. Then "Next" will show up. (Note: If the laser is not focused on the cantilever, the amplitude could not be achieved. Need to readjust the cantilever position.)
3. "Enter Force" window will show up where you can input the following typical values: Force constant: 50.0 N/m (dependent on the probe which is using). Force: 0.12 nN. Loop-gain: 1.0; Loop filter: 3 Hz. Z gain: High. Click 'Next".
4. Will show "Adjust to selected working point", click "Next" when it shows up.
5. "Seeking force" will obtain the entered force. Click "Next", then shows "Move the sensor to standby position", then can increase or decrease the standby position if needed.
6. Screen will show "Checking the oscillation next to setpoint" and "Adjust to selected working point", Click "Next".
7. "The wizard is complete" window will show up. Click "Finish". Now AFM is ready to scan on the sample. (Note: Do not touch the scanner head or sample after the adjustment is complete.)

IV. Making a Measurement

1. Review the measurement parameters at the top right of the screen and change as desired. Lower loop gain and filter means less noise; larger X/Y-width or slower scanning speed increases scan time; larger X/Y-points increases resolution.
2. Select "F2 Start Measurement." Slowly, the large square will be filled with the scanned image. During the measurement, select "F3 Stop Measurement" so that the measurement will stop after finishing current scan. Select " F4 Break Measurement" to stop the on-going scanning.
3. Store images: Return to main menu. Select "File" in main menu. Select 'Save as" and type the name for the image. (Note this only save one image that is currently active.) Select "Open" to open the file that is saved in the previous "save as" command and drag the rest of images in the other panels to this file.
4. Export images: Select "Export" under "File" submenu, choose the desired file format and type in the file name.

VII. Turning System Off

1. Return to main menu and select “Exit”. Piezomotor will automatically park.
2. Turn off DualScope controller (red button on front panel).
3. Move microscope stage all the way up (away from AFM objective) and place black cover under AFM objective to protect it.

VIII. Avoiding Problems -- CAUTION

1. Do not move the sample unless either “Change sample” or “Park Piezo Motor” has been selected. If the piezomotor is not retracted, the AFM probe can be easily broken.
2. Do not accidentally select “F5 Change Cantilever”; This moves the piezomotor to its highest position and will crash the AFM probe.

8.2 Operation Procedures for Biaxial MicroTensile Testing System

I. Turning System On

1. Turn on the power for PXI, computer, picomotor drivers and load cell modules.
2. Turn on PXI.
3. Turn on the PC computer.
4. Open the valve of the air for linear air bearing stage.

II. Setup the Specimen

1. Move the picomotor positions to the ideal position for the test before setting up the specimen.
   (1) Open the LabView program *TWOMOTORS_Setup.llb* to individually control each picomotor.
      a. Input the values for ADDRESS and COM for the desired motor;
      b. Input the speed for the motor;
      c. Input the desired position value in the POSITION option;
   (2) Move up the AFM scanner head away from the grip of the loading stage.
2. Carefully mount the specimen to the grip end using super glue or ultraviolet light glue.
3. Wait till the glue is cured.

III. Conduct the testing

1. Locate AFM over the area of interest on the specimen.
2. Turn on the power for AFM controller.
3. Turn on the insulated box that contains power supply and module for the load cell.
4. Select the channels for the data acquisition of load.
5. Open the LabView Program *Cont AcqSimultaneous2.vi* for collecting data of the load.
   (1) Input the channel numbers for data aquistion;
   (2) Input the scan rate;

(3) Input the directory to save data;

6. Open the LabView program TWOMOTORS_Control.llb for control of two motors in one axis to load the specimen simultaneously.
   (a) Input the values for ADDRESS and COM for the desired motor;
   (b) Input the speed for the motor;
   (c) Input the desired position value in the POSITION option;
7. Load the specimen and record AFM images:
   (a) Load the specimen to the desired position and record the force during the loading process;
   (b) Hold the motors stationary;
   (c) Acquire AFM images for the current load position following the procedures described in "DME DualScope Scanning Probe Microscope Standard Operation Procedures";
   (d) Save the AFM images and export the topographic image to data file;
   (e) Repeat steps (a) through (d) till the specimen fails;
8. Turn off the System:
   (a) Turn off AFM controller;
   (b) Turn off the air flow for linear air bearing;
   (c) Turn off the data acquisition system;
   (d) Turn off the picomotor driver;
   (e) Turn off the PXI;
9. Data reduction of load and displacement.

8.3 Operation Manual of the Sputtering Machine

1. Clean the substrate wafer as following steps:

   a) Clean and dry tweezers with DI water and dry N2.
   b) Take the substrate and use dry N2 to remove all particles on the substrate surfaces.
   c) Sequentially spray both sides of the substrate with Acetone, Methanol, and then Isoproponal (Note: do not let the substrate dry between sequential chemical sprays).
   d) Rinse the substrate with DI water and then dry with N2.
   e) Place in the container and carry to the sputtering machine.

2. Fully open the needle valve in the Argon gas line. Tightly close the Nitrogen and Argon valves at the upper right corner of the chamber. Tightly close the valve on the Argon supply line on the Argon tank.

3. Place your specimen on the sample holder attached to the stainless bar. Put the assembly into the chamber. Make sure your specimen is located at the center of the windows in the shielding plates. Close the chamber door. Lock it tight.
   (a) Clean the chamber using ISOPROPONAL.
   (b) Clean the sample holder and all sputtering shields using ISOPROPONAL.
   (c) Always wear gloves when touching the inside of the chamber.
   (d) Put the substrate into the vacuum chamber right after cleaning and etching.
   (e) Make sure that there is no dust on the door to ensure better sealing.
   (f) Make sure the resistance between the target and target holder is on the order of 700-800 kohms or 0.7-0.8 Mohms.
   (g) Make sure the thermocouple works by turning on the substrate heater and making sure both the thermocouples register a temperature increase. Then turn off the substrate heater.
   (h) Make sure the sputtering shield is closed prior to closing the reaction chamber door.
   (i) Connect up both ends of the thermocouple (two leads in the power supply and two leads into the sample holder).
   (j) Place all mirror and glass shields over the wires and power supply to avoid material buildup and resultant short circuits.

4. Turn on the 307 vacuum gauge controller (Press "ON").

5. Turn on the mechanical pump. Open the chamber valve, which is connected to turbo pump.

6. Wait for about 2 hours. When the pressure gauge "A" reads in the range of 3E-2 Torr, turn on the turbo pump. Do not turn on the ION gauge at this moment; otherwise you will burn the filament.
   (a) Note the sound of turbo pump running.
   (b) Watch the increase of the turbo pump speed.
   (c) When the turbo pump reaches full speed, which is at 75 KRPM, the pressure is already at the 5E-5 range, and then the ION Gauge can be used to read the pressure.

7. Turn on the heater band around the chamber to bake system. Normally bake overnight. It is optional to keep the ION Gauge on or off. Press the DEGAS button to outgas the ION Gauge for 1-2 minutes after turning the ION gauge on.

8. The vacuum will be at range of 2.0E-6 Torr when the chamber is around 70C. Turn off the heater band. Use fan to cool the chamber down for about 1 hour. The vacuum will be at around 5.0E-7 Torr. Close the needle valve tightly. Turn on the ION Gauge and degas for one to two minutes. Then turn the ION gauge off.

9. Turn on the chiller. Set the maximum temperature that the target will be allowed to reach.

10. Turn on the black valve on the ARGON tube about half circle turn. Turn on the black valve on the chamber, which connects to the Argon tube about 1/4 turn. Open the needle valve very gradually while watching the increase in the pressure.
    (a) Gauge B is more accurate when the pressure is at the 1E-2 and 1E-3 order.
    (b) Fill the chamber with Argon until Gauge B reads around 2.0E-3 Torr.

11. Turn on MDX 500 for sputtering. Set the desired power for the sputtering controller. A typical power setting is 300W. Use the constant power mode for sputtering.

12. Ten minutes after the chiller was started, push the "START " bottom at the sputtering gun controller (MDX 500 panel). One should see purple color plasma formed between the sputtering gun and the specimen. The needle valve may need adjustment from time to time to keep the Argon pressure at 2.5E-3 Torr. The turbo pump will shut itself off when the pump temperature reaches 60C.
    a) Face the fan toward the turbo pump to increase cooling.
    b) Use DISPLAY button the MDX 500 panel to read the actual power, current, and voltage as well as the setpoint values of power, current, and voltage.
    c) Presputter for a couple of minutes before opening the sputter guard. The flame color changes from purple to blue during the first couple of minutes, and this marks the time it is acceptable to open the sputter guard to sputter on the substrate.

13. Allow the system to sputter as long is wanted, then put the sputter guard down to denote the time sputtering was stopped.

14. Stop sputtering by pushing the "STOP" bottom. Turn off the power to the MDX 500 sputtering.

15. Close all the valves for the Argon to bring the system down to vacuum again. Keep the cooling water running for around 10 minutes after sputtering.

16. *Turn on the power for heater controller. Turn on the heater.(Option for heating sample)*
    a) Set the controller temperature to 500C.
    b) SPRR for the heating rate is 180C/hr. The substrate temperature is about 200C after sputtering. It will take about 2 hours to reach 500C. Then hold the temperature at 500C for 30 minutes.

17. *Turn off the heater. Cool the substrate down below 100C in vacuum (Approximately two hours).*

18. Turn off the turbo pump. Fully close the valve next to turbo pump. Vent the chamber with Argon.

(a) Fully open the Argon valve at the upper right corner of the chamber and the valve on the Argon supply line on the Argon tank. Also, fully open the Argon needle valve.
(b) Gauge B will read about 25 Torr when the Argon is actually at atmospheric pressure.

19. Open the chamber door. Turn the off the Argon valve at the upper right corner of the chamber and the valve on the Argon supply line on the Argon tank. Also, fully close the Argon needle valve. Take the specimen out of the reaction chamber. Now the system is ready for the next run.

20. Put the sample into the sample container, and mark well.

8.4 An Example Matlab Program of the Application of Pointwise DIC to the Twinning Deformation

Descriptions of the programs:

1. ***SPECKLETWIN.M:*** Generate the original image and the deformed image simulating the case of twinning deformation;
2. ***MAINTWIN.M:*** Load the images and calculate the intensity gradients of the images. Define the parameters for the Genetic Algorithms. Call the sub-program CORRELATIONTWIN and DEVECTWIN;
3. ***CORRELATIONTWIN.M:*** Calculate the correlation function for each set of variable values obtained from DEVECTWIN and pass the correlation function value to DEVECTWIN.
4. ***DEVECTWIN*.M:** Implementation of Genetic Algorithm.

SPECKLETWIN.M:

```
clear all;
num=200;
pe=10;
pipe=pi/pe;
displace=1/6.;


%Create original speckle before twinning
for i=1:num
   for j=1:num
```

```
      iiold=i;
      jjold=j;
    sinx=sin(pipe*(iiold));
    siny=sin(pipe*(jjold));
    cosx=cos(pipe*(iiold));
    cosy=cos(pipe*(jjold));
    Gxy(i,j)=(255/2)*(1+sinx.*siny);
 end
end

grayRot=Gxy/255;
imwrite(grayRot,'twinorig.tif','TIF');

%Create images with twinning deformation
for i=1:num/2
   for j=1:num
      jjold=j;
    sinx=sin(pipe*(iiold));
    siny=sin(pipe*(jjold));
    cosx=cos(pipe*(iiold));
    cosy=cos(pipe*(jjold));
    Gxytwin(i,j)=(255/2)*(1+sinx.*siny);
 end
end

for i=num/2:num
   for j=1:num
      iiold=i;
      jjold=j+displace*(iiold-num/2.);

    sinx=sin(pipe*(iiold));
    siny=sin(pipe*(jjold));
    cosx=cos(pipe*(iiold));
    cosy=cos(pipe*(jjold));
    Gxytwin(i,j)=(255/2)*(1+sinx.*siny);
 end
end

graytwin=Gxytwin/255;
imwrite(graytwin,'twinned.tif','TIF');
```

MAINTWIN:

```
clear all;
Xdim=5;
Ydim=Xdim;

num=50;
pe=10;
pipe=pi/pe;
displace=1/6;

Xorigin=21;
Yorigin=21;

aa=[1., 0; 1/6, 1.];
bb=inv(aa);

%Load Original Image

load('twinorig');
Fxysin=twinorig;


% Find the intensity gradient for the original image

x0=1:num;
y0=1:num;
[yy0, xx0]=meshgrid(y0, x0);
FxyDir=Fxysin;

value=csapi({y0,x0},FxyDir);
dir=zeros;
dir(1,1)=1;
dir(2,1)=0;
junk1=fndir(value,dir);
DfxDir=fnval(junk1,{y0,x0});
junk1a=fndir(junk1,dir);
DfxxDir=fnval(junk1a,{y0,x0});
dir=zeros;
dir(1,1)=0;
dir(2,1)=1;
junk2=fndir(value,dir);
DfyDir=fnval(junk2,{y0,x0});
junk2a=fndir(junk2,dir);
DfyyDir=fnval(junk2a,{y0,x0});
dir=zeros;
dir(1,1)=1;
dir(2,1)=0;
```

```
junk3=fndir(junk2,dir);
DfxyDir=fnval(junk3,{y0,x0});



%Load the Twinned Image

load('twinned');
Gxysin=twinned;

% Find the intensity gradients for the twinned image

GxyDir=Gxysin;
x2=1:num;
y2=1:num;
[yy2, xx2]=meshgrid(y2, x2);

valueG=csapi({y2,x2},GxyDir);
dir=zeros;
dir(1,1)=1;
dir(2,1)=0;
junk1=fndir(valueG,dir);
DgxDir=fnval(junk1,{y2,x2});
junk1a=fndir(junk1,dir);
DgxxDir=fnval(junk1a,{y2,x2});
dir=zeros;
dir(1,1)=0;
dir(2,1)=1;
junk2=fndir(valueG,dir);
DgyDir=fnval(junk2,{y2,x2});
junk2a=fndir(junk2,dir);
DgyyDir=fnval(junk2a,{y2,x2});
dir=zeros;
dir(1,1)=0;
dir(2,1)=1;
junk3=fndir(junk1,dir);
DgxyDir=fnval(junk3,{y2,x2});

%Transfer of the intensity gradients

Dgxnew=bb(1,1).*DgxDir+bb(2,1).*DgyDir;
Dgynew=bb(1,2).*DgxDir+bb(2,2).*DgyDir;
Dgxynew=DgxyDir+bb(2,1).*DgyyDir;


%*****************  Start of RUN program ************************
```

```
Axy=FxyDir;
DAx=DfxDir;
DAy=DfyDir;
DAxy=DfxyDir;

xi=Xorigin:Xorigin+Xdim-1;
yi=Yorigin:Yorigin+Ydim-1;
[yyi, xxi]=meshgrid(yi, xi);

% Select the correlation area from the original image

Fxy=Axy(xi,yi);
Dfx=DAx(xi,yi);
Dfy=DAy(xi,yi);
Dfxy=DAxy(xi,yi);

Xorigin0=Xorigin;
Yorigin0=Yorigin-Xorigin*displace;

Bxyi=GxyDir;
DBxi=Dgxnew;
DByi=Dgynew;
DBxyi=Dgxynew;

xx=xx2;
yy=yy2;

t=cputime;

% VTR                   "Value To Reach" (stop when ofunc < VTR)
                VTR = 1e-6;

% XVmin,XVmax   vector of lower and bounds of initial population
%               the algorithm seems to work well only if [XVmin,XVmax]
%               covers the region where the global minimum is expected


% D             number of parameters of the objective function

      D=Xdim*Ydim;

      XVmin =1*[ones(1,1)*(-1),ones(1,Xdim*Ydim-1)*(-1)];
                XVmax =1*[ones(1,1)*1,ones(1,Xdim*Ydim-1)*1];

% y             problem data vector (remains fixed during optimization)
```

```
                y=[];

% NP          number of population members
                NP =20;

% itermax     maximum number of iterations (generations)
                itermax = 15000;

% F           DE-stepsize F ex [0, 2]
                F = 0.8;

% CR          crossover probabililty constant ex [0, 1]
                CR = 0.25;

% strategy      1 --> DE/best/1/exp          6 --> DE/best/1/bin
%             2 --> DE/rand/1/exp          7 --> DE/rand/1/bin
%             3 --> DE/rand-to-best/1/exp  8 --> DE/rand-to-best/1/bin
%             4 --> DE/best/2/exp          9 --> DE/best/2/bin
%             5 --> DE/rand/2/exp          else  DE/rand/2/bin

                strategy = 8

% refresh     intermediate output will be produced after "refresh"
%            iterations. No intermediate output will be produced
%            if refresh is < 1
                refresh = 100;
% Print out the resultes every iteration

[xy,f,nf] =
devecTwin('correlationTwin',VTR,D,XVmin,XVmax,y,NP,itermax,F,CR,CRfinal,
strategy,refresh,Xdim,pipe,Xorigin0,Yorigin0, Fxy, Dfx, Dfy, Dfxy, Bxyi, DBxi,
DByi,DBxyi, xx, yy);
e=cputime-t
```

CORRELATIONTWIN:

```
function[result]=correlationTwin(x,y,iter,Xdim,pipe,Xorigin0,Yorigin0,Fxy,Dfx,Dfy,
Dfxy,Bxyi,DBxi,DByi,DBxyi,DByyi, xx, yy, num);
% Objective function for Differential Evolution
%
% Input Arguments:
% ----------------
% x             : parameter vector to be optimized
```

```
% y               : data vector (remains fixed during optimization)
%
% Output Arguments:
% ----------------
% result            : objective function value
%

Ydim=Xdim;
num=num;
for j=1:Ydim
   for i=1:Xdim

      Xstar(i,j)=i+Xorigin0-1+x(Xdim*(j-1)+i);
      Ystar(i,j)=j+Yorigin0-1+x(Xdim*Ydim+Xdim*(j-1)+i);
   end
end

xi=Xstar;
yi=Ystar;

Gxyinterp=interp2(yy,xx,Bxyi, yi, xi, 'cubic');
Dgxinterp=interp2(yy,xx,DBxi, yi, xi, 'cubic');
Dgyinterp=interp2(yy,xx,DByi, yi, xi, 'cubic');
Dgxyinterp=interp2(yy,xx,DBxyi, yi, xi, 'cubic');
Dgyyinterp=interp2(yy,xx,DByyi, yi, xi, 'cubic');


for j=1:Ydim
   for i=1:Xdim

      if Xstar(i,j)>num/2
         Dgxnew(i,j)=Dgxinterp(i,j)-(1/6)*Dgyinterp(i,j);
         Dgxynew(i,j)=Dgxyinterp(i,j)-(1/6)*Dgyyinterp(i,j);
      else
         Dgxnew(i,j)=Dgxinterp(i,j);
         Dgxynew(i,j)=Dgxyinterp(i,j);
      end

   end
end

Gxynew=Gxyinterp;
Dgynew=Dgyinterp;

FG=(Fxy-Gxynew).*(Fxy-Gxynew)+(Dfx-Dgxnew).*(Dfx-Dgxnew)+(Dfy-
Dgynew).*(Dfy-Dgynew)...
```

```
   +(Dfxy-Dgxynew).*(Dfxy-Dgxynew);

result=sum(sum(FG));
```

DEVECTWIN:

```
function[result]=correlationTwin(x,y,iter,Xdim,pipe,Xorigin0,Yorigin0,Fxy,Dfx,Dfy,
Dfxy,Bxyi,DBxi,DByi,DBxyi,DByyi, xx, yy, num);
% Objective function for Differential Evolution
%
% Input Arguments:
% ---------------
% x               : parameter vector to be optimized
% y               : data vector (remains fixed during optimization)
%
% Output Arguments:
% ----------------
% result            : objective function value
%

Ydim=Xdim;
num=num;
for j=1:Ydim
   for i=1:Xdim

      Xstar(i,j)=i+Xorigin0-1+x(Xdim*(j-1)+i);
      Ystar(i,j)=j+Yorigin0-1+x(Xdim*Ydim+Xdim*(j-1)+i);
   end
end

xi=Xstar;
yi=Ystar;

Gxyinterp=interp2(yy,xx,Bxyi, yi, xi, 'cubic');
Dgxinterp=interp2(yy,xx,DBxi, yi, xi, 'cubic');
Dgyinterp=interp2(yy,xx,DByi, yi, xi, 'cubic');
Dgxyinterp=interp2(yy,xx,DBxyi, yi, xi, 'cubic');
Dgyyinterp=interp2(yy,xx,DByyi, yi, xi, 'cubic');


for j=1:Ydim
   for i=1:Xdim
```

```
        if Xstar(i,j)>num/2
           Dgxnew(i,j)=Dgxinterp(i,j)-(1/6)*Dgyinterp(i,j);
           Dgxynew(i,j)=Dgxyinterp(i,j)-(1/6)*Dgyyinterp(i,j);
        else
           Dgxnew(i,j)=Dgxinterp(i,j);
           Dgxynew(i,j)=Dgxyinterp(i,j);
        end

    end
end

Gxynew=Gxyinterp;
Dgynew=Dgyinterp;

FG=(Fxy-Gxynew).*(Fxy-Gxynew)+(Dfx-Dgxnew).*(Dfx-Dgxnew)+(Dfy-
Dgynew).*(Dfy-Dgynew)...
    +(Dfxy-Dgxynew).*(Dfxy-Dgxynew);

result=sum(sum(FG));
```

9 References

1. Binnig, G., Quate, C.F., Gerber, C., "Atomic Force Microscope", PHYSICAL REVIEW LETTERS, 56 (9), 930-933, 1986

2. Bobji, M.S., Bhushan, B., "Atomic Force Microscopic Study of the Microcracking of Magnetic Thin Films under Tension", SCRIPTA MATERILLIA, 44 (1), 37-42, 2001

3. Bobji, M.S., Bhushan, B., "In-Situ Microscopic Surface Characterization Studies of Polymeric Thin Films during Tensile Deformation using Atomic Force Microscopy", JOURNAL OF MATERIALS RESEARCH, 16(3), 844-855, 2001

4. Bobji, M.S., Bhushan, B., "A Technique to Measure Poisson's Ratio of Ultrathin Polymeric Films Using Atomic Force Microscopy", REVIEW OF SCIENTIFIC INSTRUMENTS, 74 (2), 1043-1047, 2003

5. Brooks, R.R., Iyengar, S.S., Chen J., "Automatic Correlation and Calibration of noisy sensor readings using elite genetic algorithms", ARTIFICIAL INTELLIGENCE, 84, 339-354, 1996

6. Bruck H.A., McNeil S.R., Sutton M.A. and Peters W.H., "Digital Image Correlation Using Newton-Raphson Method of Partial Differential Correction," EXPERIMENTAL MECHANICS, 29, 261-267, 1989

7. Bruck, H.A., Moore, C.L., Valentine, T.L., "Repeatable Bending Actuation in Polyurethane using Opposing Embedded One-way Shape Memory Alloy wires Exhibiting Large Deformation Recovery", SMART MATERIALS & STRUCTURES, 11 (4), 509-518, 2002

8. Bruck, H.A., Moore, C.L., Valentine, T.L., "Bending Actuation in Polyurethanes with a Symmetrically Graded Distribution of One-way Shape Memory Alloy Wires", EXPERIMENTAL MECHANICS, 44 (1), 62-70, 2004

9. Cardenas-Garcia, J.F., Ekwaro-Osire, S., "Elements of Design of a Biaxial Tester for Micro-electromechanical Systems (MEMS) Materials", JOURNAL OF ENGINEERING DESIGN, 2004, (in review)

10. Cardenas-Garcia, J.F., Ekwaro-Osire, S., "Development of a Bi-axial Micro-Tensile Tester of MEMS Materials for Research and Student Training", NSF PROPOSAL, 2000

11. Chandrasekaran, D., Nygards, M., "A Study of the Surface Deformation Behavior at Grain Boundaries in an Ultra-low-carbon Steel", ACTA MATERILLIA, 51 (18), 5375-5384, 2003

12. Chandrasekaran, D., Nygards, M., “Comparison of Surface Displacement Measurements in a Ferritic Steel using AFM and Non-local Plasiticity”, MATERIALS SCIENCE AND ENGINEERING A-STRUCT URE, 365 (1-2), 191-195, 2004

13. Chasiotis, I., Fillmore, H.L., Gillies, G.T., “Atomic Force Microscopy Measurement of Cytostructural Elements Involved in the Nanodynamics of Tumor Cell Invasion”, NANOTECHNOLOGY, 14, 557-561, 2003

14. Chasiotis L., Knauss W.G., “A New Microtensile Tester for the Study of MEMS Materials with Aid of Atomic Force Microscopy”, EXPERIMENTAL MECHANICS, 42 (1), 51-57, 2002

15. Chen, H., Liu, D., Lee, A., “Moiré in Atomic Force Microscope”, EXPERIMENTAL TECHNIQUES, 24 (1): 31-32, 2000

16. Cho, S., Cardenas-Garcia, J.H., “Measurement of Nano-Displacements and Mechanical Properties of MEMS via the Microscopic Hole Method”, SENSORS AND ACTUATORS A: PHYSICS, 2004, (*accepted)*

17. Chokshi, A.H., Rosen, A., Karch, J., Gleiter, H., “On the Validity of the Hall-Petch Relationship in Nanocrystalline Materials”, SCRIPTA METALLURGICA, 23 (10): 1679-1683, 1989

18. Chona, R., Khanna, S.K., Kmiec, K.J., “Application of High-resolution Geometric Moire Method to Fracture Problems”, EXPERIMENTAL TECHNIQUES, 19 (6): 10-13, 1995

19. Cretegny, L., Saxena, A., “AFM Characterization of the Evolution of Surface Deformation during Fatigue in Polyscrystalline Copper”, ACTA MATERILLIA, 49 (18), 3755-3765, 2001

20. Chu, T.C., Peters, W.H., Ranson, W.F. and Sutton, M.A., “Application of Digital Correlation Methods to Rigid Body Mechanics,” Proc. 1982 Fall Meeting of SESA, 73-77, 1982

21. Dai, F.L., Wang, Z.Y., “Geometric Micron-moire”, OPTICS AND LASERS INENGINEERING, 31 (3): 191-198, 1999

22. Gallego-Juárez, J.A., “Piezoelectric Ceramics and Ultrasonic Transducers”, JOURNAL OF PHYSICS, E: SCIENTIFIC INSTRUMENTS, 22, 804-816, 1989

23. Dally, J.W. and Read, D.T., “Electron-beam Moiré,” EXPERIMENTAL MECHANICS, 33, 270–277, 1993

24. Dally, J.W. and Read, D.T., “Micromechanics Study of the Effects of Damage on Interface Strains,” NOVEL EXP. TECH. FRACT. MECH., 17 (6), 1–11, 1993

25. Dasari, A., Rohrmann, J., Misra, R.D.K, “Atomic Force Microscopy Assessment of Mechanically Induced Scratch Damage in Polypropylenes and Ethylene-Propylene di-block Copolymers”, MATERIALS SCIENCE AND ENGINEERING A-STRUCTURE, 354 (1-2), 67-81, 2003

26. Dasari, A., Rohrmann, J., Misra, R.D.K, “On the Scratch Deformation of Micrometric Wollastonite Reinforced Polypropylene Composites”, MATERIALS SCIENCE AND ENGINEERING A-STRUCTURE, 364 (1-2), 357-369, 2004

27. Derlet, P.M., Hasnaoui, A., Van Swygenhoven, H., “Atomistic Simulations as Guidance to Experiments”, SCRIPTA MATERIALIA, 49 (7), 629-635, 2003

28. Drexler, E.S., “Reliability of A Flip-chip Package Thermally Loaded between 55 DegreesCand 125 Degrees C,” JOURNAL OF ELECTRONIC MATERIALS, 28, 1150–1157, 1999

29. Drexler, E.S. and Berger, J.R., “Mechanical Deformation in Conductive Adhesives as Measured with Electron-beam Moiré,” JOURNAL OF ELECTRONIC PACKAGING, 121 (2), 69–74, 1999

30. Gleiter, H., “Nanocrystalline materials”, PROGRESS IN MATERIALS SCIENCE, 33, 223-315, 1989

31. Gleiter, H., “Nanostructured Materials: State of the Art and Perspectives”, NANOSTRUCTURED MATERIALS, 6 (1-4): 3-14, 1995

32. Gleiter, H., “Nanostructured Materials: Basic Concepts and Microstructure”, ACTA MATERIALLIA, 48, 1-29, 2000

33. Grediac, M., “The Use of Full-field Measurement Methods in Composite Material Characterization: Interest and Limitations”, COMPOSITES PART A-APPLIED SCIENCE AND MANUFACTURING, 35 (7-8), 751-761, 2004

34. Hall, E.Q., “The Deformation and Ageing of Mild Steel .3. Discussion of Results”, PROCEEDINGS OF THE PHYSICAL SOCIETY OF LONDON SECTION B, 64 (381): 747-753, 1951

35. Han, B. and Post, D., “Immersion Interferometer for Microscopic Moiré Interferometry,” EXPERIMENTALMECHANICS, 32, 38–41, 1992

36. Han, B., “Micromechanical Deformation Analysis of Beta Alloy Titanium in Elastic and Elastic/Plastic Tension”, 36(2), 120-126, 1996

37. Haque, M.A., Saif, T.A., “Microscale Materials Testing Using MEMS Structures”, JOURNAL OF MICROELECTROMECHANICAL SYSTEMS, 10(1), 2001

38. Harvey, S.E., Marsh, P.G., Gerberich, W.W., “Atomic Force Microscopy and Modeling of Fatigue-Crack Initiation in Metals”, ACTA METALL MATERILLIA, 42 (10), 3493-3502, 1994

39. Horita, Z., Smith, D.J, Furukawa, M., “High-resolution Electron Microscopy Observations of Grain Boundary Structures in Submicrometer-grained Al-Mg Alloys”, MATERIALS SCIENCE FORUM, 204, 437-442, Part 1-2, 1996

40. Husson, C., Bahlouli, N., Mguil, S., Ahzi, S., “Mechanical Characterization of Thin Metal Sheets by a Digital Image Correlation Method”, JOURNAL DE PHYSIQUE IV, 12 (PR11), 393-400, 2002

41. Kai Dirsche, “Online Correction of Scanning Probe Microscopes with Pixel Accuracy”, Ph.D Thesis, 2000

42. Kishimoto, S., Egashira, M., Shinya, N., “Micro creep Deformation Measurement by a Moire Method using Electron-Beam Lithography and Electron-Beam Scan”, OPTICAL ENGINEERING, 32(3), 522-526, 1993

43. Koskinen J., Steinwall J. E., Soave R., Johnson H. H., “Microtensile Testing of Free-standing Polysilicon Fibers of Various Grain Sizes”, JOURNAL OF MICROMECHANICS AND MICROENGINEERING, 3, 13-17, 1993

44. Koza, J.R., Bennett, F.H., Andre, D., Keane, M.A., “Genetic Programming III, Darwinian Invention and Problem Solving”, Morgan Kaufmann Publishers, San Francisco, CA, 1999

45. Kraft, O., Volkert, C.A., “Mechanical Testing of Thin Films and Small Structures”, ADVANCED ENGINEERING MATERIALS, 3 (3), 99-110, 2001

46. Kumar, K.S., Swygenhoven, H. V., Suresh, S., “Mechanical Behavior of Nanocrystalline Metals and Alloys”, ACTA MATERIALLIA, 51, 5743-5774, 2003

47. Li, S.X., Chen, M., Zhang, T.I., Sun, L.Z., Wang, Z.G., “The Crack-growth toward the Grain-Boundary of a Fatigued Aluminum Bicrystal”, SCRIPTA METALLURGICA ET MATERIALIA, 31 (7), 897-902, 1994

48. Lian, J., Baudelet, B., Nazarov, A.A., “Model for the Prediction of the Mechanical Behavior of Nanocrystalline Materials”, MATERIALS SCIENCE AND ENGINEERING A-STRUCTURAL MATERIALS PROPERTIES MICROSTRUCTURE AND PROCESSING, 172 (1-2), 23-29, 1993

49. Liu, C.M., Chen, L.W., “Digital Atomic Force Microscope Moire Method”, ULTAMICROSCOPY, 101 (2-4): 173-181, 2004

50. Lu, H. and Cary, P.D., “Deformation Measurement by Digital Image Correlation: Implementation of a Second-order Displacement Gradient”, EXPERIMENTAL MECHANICS, 40(4), 393-401, 2000

51. Lu, Y.G., Zhong, Z.W., Yu, J., Xie, H.M., Chai, G.B., Asundi, A., “Thermal Deformation Measurement of Electronic Packages using the Atomic Force Microscope Scanning Moire Technique”, REVIEW OF SCIENTIFIC INSTRUMENTS, 72 (4): 2180-2185, 2001

52. Luo,P.F., Chao, Y.J., Sutton, M.A. and Peters, W.H., “Accurate Measurements of Three-dimensional Deformations in Deformable and Rigid Bodies Using Computer Vision,” EXPERIMENTAL MECHANICS, 33, 123-132, 1993

53. Mearini, G.T., Hoffman, R.W., “Tensile Properties of Aluminum Multilayered Thin Films”, JOURNAL OF ELECTRONIC MATERIALS, 22 (6), 623-629, 1993

54. Moore, C.L., Bruck, H.A., “A Fundamental Investigation into Large Strain Recovery of One-way Shape Memory Alloy Wires Embedded in Flexible Polyurethane”, SMART MATERIALS & STRUCTURES, 11 (1), 130-139, 2002

55. Morimoto, Y., Hayashi, T., and Wada, K., “High-sensitivity Measurement of Strain by Moiré Interferometry,” JSME INTERNATIONAL JOURNAL SERIES I-SOLID MECHANICS, 32122–127, 1989

56. Nieh, T.G., Wadsworth, J., “Hall-Petch Relation in Nanocrystalline Solids”, SCRIPTA METALLURGICA ET MATERIALIA, 25 (4), 955-958, 1991

57. Nieman, G.W., Weertman, J. R., Siegel, R.W., “Tensile-strength and Creep Properties of Nanocrystalline Palladium”, SCRIPTA METALLURGICA ET MATERIALLIA, 24(1), 145-150, 1990

58. Nix, W.D., “Mechanical Properties of Thin Films”, METALLURGICAL TRANSACTIONS A-PHYSICAL METALLURGY AND MATERIALS SCIENCE, 20 (11), 2217-2245, 1989

59. Paredes, J.I., Martinez-Alonso, A., Tascon, J.M.D., “Application of Scannning Tunneling and Atomic Force Microscopies to the Characterization of Microporous and Mesoporous Materials”, MICROPOROUS AND MESOPOROOUS MATERIALS, 65, 93-126, 2003

60. Petch, N.J., “The Cleavage Strength of Polycrystals”, JOURNAL OF THE IRON AND STEEL INSTITUTE, 174 (1): 25-28, 1953

61. Peters, W.H. and Ranson, W.F., “Digital Imaging Techniques in Experimental Stress Analysis,” OPTICAL ENGINEERING, 21, 437-432, 1982

62. Post, D., Han, B., and Ifju, P., High Sensitivity Moiré—Experimental Analysis for Mechanics and Materials, Springer-Verlag, Berlin, 1994

63. Post, D., “Moiré Interferometry—Advances and Applications,” EXPERIMENTAL MECHANICS, 31, 276–280, 1991

64. Read, D.T. and Dally, J.W., “Local Strain Measurement by Electron Beam Moiré,” ADVANCES IN ELECTRONIC CIRCUIT PACKAGING, 4, 163–169, 1993

65. Read, D.T. and Dally, J.W., “Electron-beam Moiré Study of Fracture of a Glass-fiber-reinforced Plastic Composite,” JOURNAL OF APPLIED MECHANICS, 61, 402–409, 1994

66. Read, D.T. and Dally, J.W., “Fatigue of Microlithographicallypatterned Freestanding Aluminum Thin-film Under Axial Stresses,” JOURNAL OF ELECTRONIC PACKAGING, 117 (1), 1–6, 1995

67. Read, D.T. and Dally, J.W., “Theory of Electron Beam Moiré,” JOURNAL OF RESEARCH OF THE NATIONAL INSTITUTE OF STANDARDS AND TECHNOLOGY, 101 (1), 47–61, 1996

68. Read, D.T., “Piezo-actuated Microtensile Test Apparatus”, JOURNAL OF TESTING EVALUATION, 26(3), 255-259, 1998

69. Rugar, D., Mamin, H.J., Erlandsson, R., Stern, J.E., Terros, B.D., “Force Microscope Using a Fiber-Optic Displacement Sensor”, REVIEW OF SCIENTIFIC INSTRUMENTS, 59 (11), 2337-2340, 1988

70. Rugar, D., Hansma, P., “Atomic Force Microscopy”, PHYSICS TODAY, 43 (10): 23-30, 1990

71. Ruud, J.A., Josell, D. and Spaepen, F., “ A New Method for Tensile Testing of Thin Films”, JOURNAL OF MATERIALS RESEARCH, 8(1), 112-117, 1993

72. Sharpe W.N. Jr., Yuan Bin, Edwards R.L., “A New Technique for Measuring the Mechanical Properties of Thin Films”, JOURNAL OF MICROELECTROMECHANICAL SYSTEMS, 6(3), 1997

73. Sharpe W. N. Jr., Turner K. T., Edwards R. L., “Tensile Testing of Polysilicon”, EXPERIMENTAL MECHANICS, 39(3), 162-170, 1999

74. Schiotz, J., Vegge, T., Di Tolla, F.D., Jacobsen, K.W., “Atomic-scale Simulations of the Mechanical Deformation of Nanocrystalline Metals”, PHYSICAL REVIEW B, 60 (17), 11971-11983, 1999

75. Schiotz J, Di Tolla FD, Jacobsen KW, “Softening of Nanocrystalline Metals at Very Small Grain Sizes”, NATURE, 391 (6667): 561-563, 1998

76. Srikar, V. T., Spearing, S.M., “A Critical Review of Microscale Mechanical Testing Methods Used in the Design of Microelectromechanical Systems”, EXPERIMENTAL MECHANICS, 43(3), 2003

77. Storn, R. and Price, K., “Differential Evolution - a Simple and Efficient Heuristic for Global Optimization over Continuous Spaces,” JOURNAL OF GLOBAL OPTIMIZATION, 11, 341 – 35, 1997

78. Sutton, M.A., Wolters, W.J., Peters, W.H., Ranson, W.F., and MeNeil, S.R., “Determination of Displacements Using an Improved Digital Image Correlation Method,” IMAGE VISION COMPUTING, 1(3), 133-139, 1983

79. Sutton, M.A., Cheng, M., Peters, W.H., Chao, Y.J., and NcNeil, S.R., “Application of an Optimized Digital Image Correlation Method to Planar Deformation Analysis,” IMAGE VISION COMPUTING, 4(3), 143-150, 1986

80. Tong, W., Hector, L.G., Weiland, H., “In-situ Surface Characterization of a Binary Aluminum Alloy during Tensile Deformation”, SCRIPTA MATERILLIA, 36 (11), 1339-1344, 1997

81. Tsuchiya, T., Tabata, T., Sakata, S. and Tagi, Y., “ Specimen Size Effect on Tensile Strength of Surface Micromachined Polysilicalline Silicon Thin Films”, PROCEEDINGS OF THE TENTH IEEE INTERNATIONAL WORKSHOP ON MICROELECTROMECHANICAL SYSTEMS, Nagoya, Japan, 529-534, 1997

82. Valiev, R.Z., Chmelik, F., Bordeaux, F., “The Hall-Petch in Submicro-Grained Al 1.5%MG alloy”, SCRIPTA METALLURGICA ET MATERIALIA, 27 (7), 855-860, 1992

83. Van Swygenhoven H, Derlet PM, Hasnaoui A “Atomic Mechanism for Dislocation Emission from Nanosized Grain Boundaries”, PHYSICAL REVIEW B, 66 (2), 2002

84. Vendroux, G. and Knauss, W.G., “Submicron Deformation Fields Measurements: Par1: Developing a Digital Scanning Tunneling Microscope,” EXPERIMENTAL MECHANICS, 38(2), 86-92, 1998

85. Vendroux, G. and Knauss, W.G., “Submicron Deformation Fields Measurements: Par2: Improved Digital Image Correlation,” EXPERIMENTAL MECHANICS, 38(3), 18-23, 1998

86. Vendroux, G. and Knauss, W.G., “Submicron Deformation Fields Measurements: Par3: Demonstration of Deformation Determinations” EXPERIMENTAL MECHANICS, 38(3), 154-160, 1998

87. Vossen, J.L., Kern, W., THIN FILM PROCESSES II, Academic Processes, San Diego, CA, 1991

88. Wang, Y., Cuitino, A.M., “Full-field Measurements of Heterogeneous Deformation Patterns on Polymeric Foams using Digital Image Correlation”, INTERNATIONAL JOURNAL OF SOLIDS AND STRUCTURES, 39 (13-14), 3777-3796, 2002

89. Wang, Z.Y., Dai, F.L., Jiang, X.L., “High Resolution, High Sensitivity Moire Method”, ACTA MECHANICA SINICA, 15 (2): 176-181, May 1999

90. Wattrisse, B., Chrysochoos, A., Muracciole, J.M., Nemoz-Gaillard, M., “Analysis of Strain Localization during Tensile Tests by Digital Image Correlation”, EXPERIMENTAL MECHANICS, 41 (1), 29-39, 2001

91. Xie, H.M., Kishimoto, S., Asundi, A., Boay, C.G., “In-plane Deformation Measurement using the Atomic Force Microscope Moiré Method”, NANOTECHNOLOGY, 11, 24-29, 2000

92. Xie, H.M., Asundi, A., Boay, C.G., Lu, Y.G., Yu, J., Zhong, Z.W., Ngoi, B.K.A., “High Resolution AFM Scanning Moiré Method and its Application to the Micro-deformation in the BGA electronic package”, MICROELECTRONICS RELIAGILITY, 42 (8): 1219-1227, 2002

93. Zhang, D.S., Eggleton, C.D., Arola, D.D., “Evaluating the Mechanical Behavior of Arterial Tissue using Digital Image Correlation”, EXPERIMENTAL MECHANICS, 42 (4), 409-416, 2002

94. Zhang, D.S., Arola, D.D., “Applications Tissues of Digital Image Correlation to Biological”, JOURNAL OF BIOMEDICAL OPTICS, 9 (4), 691-699, 2004

95. Zhong, Z.W., “Thermal Strain Analysis of IC Packages using Various Moire Methods”, MICROELECTRONICS INTERNATIONAL, 21 (3): 25-28, 2004

96. Zhong, Z.W., Lu, Y.G., “An AFM Scanning Moire Technique for the Inspection of Surface Deformations”, INTERNATIONAL JOURNAL OF ADVANCED MANUFACTURING TECHNOLOGY, 23 (5-6): 462-466, 2004